Title

Quantification and Deep Learning Applications: Metabolite-Specific Hyperpolarized 13C-Pyruvate MRI and Multiphase CT in Renal Cell Carcinomas

Author

Sahin, Sule

Publication Date

2024

Peer reviewed|Thesis/dissertation

Quantification and Deep Learning Applications: Metabolite-Specific Hyperpolarized 13C-Pyruvate MRI and Multiphase CT in Renal Cell Carcinomas

by

Sule Irem Sahin

DISSERTATION

Submitted in partial satisfaction of the requirements for degree of

DOCTOR OF PHILOSOPHY

in

Bioengineering

in the

GRADUATE DIVISION

of the

UNIVERSITY OF CALIFORNIA, SAN FRANCISCO
AND
UNIVERSITY OF CALIFORNIA, BERKELEY

Approved:

DocuSigned by:
Peder Larson
1644A2CD853841E...

Peder Larson

Chair

Signed by:
Steven Conolly
DocuSigned by:

Steven Conolly

Daniel Vigneron
DA5485F9C42341E...

Daniel Vigneron

Committee Members

ACKNOWLEDGMENTS

First, I would like to give my utmost thanks to my research adviser, Dr. Peder Larson. I've learned an endless amount about MRI, medical imaging, research skills, project management, scientific writing, pharmacokinetic modeling, and more, from you which I'm incredibly grateful for. Many times, during my PhD, I attended our meetings stressed about a project, but through your guidance and encouragement, left the meeting motivated and much less distressed. I am incredibly appreciative of the time you spent mentoring me.

I would like to thank the rest of my dissertation committee: Dr. Dan Vigneron, Dr. Steve Conolly and Dr. Zhen Jane Wang. Dan has been a great mentor to me during my PhD and it was in part due to a phone call we had in 2019 in which I made the decision to move across the country to join this Bioengineering PhD program. I also want to thank him for being a supportive and exceptional qualifying exam committee chair. I'd like to extend my appreciation to Dr. Steve Conolly in challenging me to answer the questions pertaining to the broader impact about my research and serving as a friendly graduate adviser when I first started the program. I'd like to thank Dr. Zhen Jane Wang for being a fantastic resource for anything about renal cell carcinoma and radiology. I've learned a lot from our conversations and emails.

I'd like to thank Dr. Janine Lupo for serving as my graduate adviser, a member of my qualifying exam committee and mentoring me as a rotation student. A huge thank you to Dr. Renuka Sriram for teaching me all about Hyperpolarized C13 imaging on the preclinical system and advising me when I was writing my first first-author paper. I'd like to thank Xiao Ji for also teaching me loads about the Bruker system and helping set up the spectral-spatial EPI sequence. Thank you to

Dr. Jeremy Gordon for being a great resource on Hyperpolarized C13 MRI and for great feedback on projects. A huge thanks to Marie Frederikke Garnæs from the Technical University of Denmark for her collaboration on the bSSFP pharmacokinetic modelling.

I would like to thank present and past Larson Lab members for years of great scientific discussion, collaboration and at times fun and laughs. Thank you to Anna Bennett, Avantika Sinha, Ernesto Diaz, Nikhil Deveshwar, Dr. Xiaoxi Liu, Dr. Xin Shen, Erin Argentieri, Dr. Charlie Wang, Dr. Nick Dwork, Dr. Manushka Vaidya, Dr. Abhejit Rajagopal, Dr. Andrew Leynes and Dr. Fei Tan. I've learned a great deal from all of you and am so grateful to have had you as lab mates. Additionally, a thank you to Dr. Shuyu Tang, who allowed me to use his data for the pharmacokinetic modelling project and gave me tons of great feedback over the years.
I would like to thank members of the Hyperpolarized MRI Technology and Resource Center (HMTRC). Dr. Yaewon Kim, Dr. Hsin-Yu Chen, Dr. Changhua Mu, and Lynn Delos Santos for teaching me reusable fluid path preparation, how to use and troubleshoot the SpinLab and helping me when I was struggling in the electronics lab. I'd like to thank Kim Semien for helping schedule many animal studies for me. I'd also like to thank Mary Frost, Heather Daniel and all the other MRI technologists in the Surbeck lab.

A huge thank you to Cresini Trabanza-David for helping with scheduling and reimbursements in the lab. Thank you to Victoria Starett and Rocío Sanchez for supporting my progress and ensuring I met the requirements of the Bioengineering program.

Last but not least I would like to thank my family for their continuous support over the past years. A huge thank you to my parents, Adnan and Imge Sahin, for supporting my educational achievements and inspiring me to challenge myself. Thank you to my sister, Asli Sahin, for being a great friend and support system. An enormous thank you to my husband Tim Mastovich. You make me a better person every day and I couldn't have done this without your enduring support and encouragement.

CONTRIBUTIONS

1. “Metabolite-Specific Echo Planar Imaging for Preclinical Studies with Hyperpolarized 13C-Pyruvate MRI”. Sule I Sahin, Xiao Ji, Shubhangi Agarwal, Avantika Sinha, Ivina Mali, Jeremy W Gordon, Mark Mattingly, Sukumar Subramaniam, John Kurhanewicz, Peder EZ Larson*, Renuka Sriram*. *Tomography*, 2023. (*=authors contributed equally)
2. “A pharmacokinetic model for hyperpolarized ^{13}C-pyruvate MRI when using metabolite-specific bSSFP sequences”. Sule Sahin, Marie Frederikke Garnæs, Anna Bennett, Nicholas Dwork, Shuyu Tang, Xiaoxi Liu, Manushka Vaidya, Zhen Jane Wang, Peder EZ Larson. *Magnetic Resonance in Medicine*, 2024.

QUANTIFICATION AND DEEP LEARNING APPLICATIONS: METABOLITE-SPECIFIC HYPERPOLARIZED 13C-PYRUVATE MRI AND MULTIPHASE CT IN RENAL CELL CARCINOMAS

SULE IREM SAHIN

ABSTRACT

Incidental discoveries of renal cell carcinomas, the most common type of kidney cancer, have increased in recent years due to improved imaging technologies. It is crucial to be able to characterize the pathology and tumor grade of discovered renal masses to optimize treatment planning. This problem will be approached in this dissertation using advanced metabolic MRI methods and CT data collection.

Hyperpolarized [1-^{13}C]pyruvate (HP C13) MRI has emerged as a method of imaging metabolic pathways in cancer, including kidney cancer. Yet further acquisition and quantification improvements are needed to optimize clinical relevance.

To improve HP C13 MRI acquisition in preclinical systems, a spectral-spatial echo planar imaging (EPI) sequence is proposed and compared to using a chemical shift imaging (CSI) acquisition. The EPI sequence is found to reduce partial volume effects and expedite acquisition. To improve upon quantification of HP C13 MRI, a novel pharmacokinetic model for balanced steady state free precession (bSSFP) acquisitions is proposed to fit apparent rate constants, k_{PL} and k_{PB}. The fit rate constant maps are compared to results from previous pharmacokinetic models in paired preclinical and clinical datasets.

Additionally, a U-Net is trained to estimate k_{PL} maps from HP C13 MRI data to take advantage of spatial relationships in the data. A novel anatomic HP C13 MRI brain phantom is introduced as training data for the U-Net. The U-Net is further finetuned with in vivo datasets. The U-Net predicted rate constant maps are compared to using a pharmacokinetic model to fit maps. Finally, a 500+ 3D multiphase renal tumor CT dataset is described to increase available data examples of renal tumors for better performance of data-driven approaches in renal tumor characterization.

TABLE OF CONTENTS

LIST OF FIGURES

LIST OF TABLES

CHAPTER 1: INTRODUCTION

Magnetic resonance imaging, ubiquitously known as MRI, is an incredibly powerful medical imaging tool for anatomical and functional imaging and has had a widespread impact in the field of medicine since its inception in the 1970s[1]. Recently, the invention of dynamic nuclear polarization (DNP) techniques has made in vivo MRI of ^{13}C possible[2]. Particularly the imaging of [1-^{13}C]pyruvate, termed hyperpolarized [1-^{13}C]pyruvate MRI has been a growing field of interest as pyruvate is the precursor to multiple metabolic pathways. The power of hyperpolarized [1-^{13}C]pyruvate MRI is in its' ability to probe each of these pathways, and gather in vivo data not just of pyruvate but its' metabolites: lactate, bicarbonate and alanine, as well.

Since the first in-human hyperpolarized [1-^{13}C]pyruvate MRI in prostate cancer patients[3], there has been an interest in using this technology for oncology applications. Dysregulated metabolism is a hallmark of cancer[4] and hyperpolarized [1-^{13}C]pyruvate MRI can clue us into the metabolism of tumors in a minimally invasive manner. Renal cell carcinoma, the most common type of kidney cancer, is specifically a cancer that has shown to exhibit dysregulated metabolism[5], which has made it an excellent candidate for hyperpolarized [1-^{13}C]pyruvate MRI studies[6,7]. The characterization of renal cell carcinomas is challenging with standard imaging protocols[8–10], which makes treatment planning challenging. This challenge either requires data-driven approaches, like deep learning, or new contrasts, like hyperpolarized [1-^{13}C]pyruvate.

1.1 Outline

Chapter 2 will introduce the foundational basics of MR imaging. It will next describe hyperpolarized [1-^{13}C]pyruvate MRI including challenges and recent advances. Finally, renal cell

carcinomas will be introduced. Specifically, computed tomography (CT) imaging of renal cell carcinomas and the metabolism of renal cell carcinomas will be reviewed.

Chapters 3-5 present advancements in acquisition and quantification of hyperpolarized [1-^{13}C]pyruvate MRI. Chapter 3 describes the implementation of a metabolite-specific echo planar imaging (EPI) sequence for hyperpolarized [1-^{13}C]pyruvate MRI on a Bruker 3T preclinical MR system. Here, the EPI sequence will be compared with a chemical shift imaging (CSI) sequence, through simulations of the point spread function and in vivo experiments. For the EPI sequence, simulations are also used to determine optimal pyruvate and lactate flip angles. Finally, pharmacokinetic modeling is performed to compute and compare the k_{PL} maps for CSI and EPI acquisitions.

Chapter 4 introduces a novel pharmacokinetic model to be used in hyperpolarized [1-^{13}C]pyruvate MRI experiments where one or more metabolites are acquired with a balanced steady state free precession (bSSFP) sequence. This model is validated on preclinical and clinical datasets that have paired acquisitions with spoiled gradient echo (GRE)-only acquisitions. The model performs well and fits k_{PL} and k_{PB} values similar to those used with a previous PK model on the GRE-only acquisitions.

Chapter 5 describes a method to train a U-Net to estimate k_{PL} maps from hyperpolarized [1-^{13}C]pyruvate MR dynamics. An anatomically accurate brain phantom pipeline is also described and used to generate a diverse training dataset to train the U-Net. The model is further finetuned

using in vivo brain datasets. The U-Net predicted k_{PL} maps are compared to maps derived using a pharmacokinetic model for simulated and in vivo test cases.

Chapter 6 presents a 3D multi-phase renal tumor CT dataset. This chapter describes the data curation process including, data formatting, registration of the phases to one another and the creation of tumor masks. Additionally, an analysis of the number of phases, pathologies, and pathology grades within the dataset is performed and presented.

1.2 References

1. Lauterbur PC. Image Formation by Induced Local Interactions: Examples Employing Nuclear Magnetic Resonance. *Nature*. 1973;242(5394):190-191. doi:10.1038/242190a0

2. Ardenkjær-Larsen JH, Fridlund B, Gram A, Hansson G, Hansson L, Lerche MH, et al. Increase in signal-to-noise ratio of > 10,000 times in liquid-state NMR. *Proc Natl Acad Sci*. 2003;100(18):10158-10163. doi:10.1073/pnas.1733835100

3. Nelson S, Kurhanewicz J, Vigneron D, Larson P, Harzstark A, Ferrone M, et al. Metabolic Imaging of Patients with Prostate Cancer Using Hyperpolarized [1-13C]Pyruvate. *Sci Transl Med*. 2013;5(198):198ra108. doi:10.1126/scitranslmed.3006070

4. Hanahan D, Weinberg RA. Hallmarks of Cancer: The Next Generation. *Cell*. 2011;144(5):646-674. doi:10.1016/j.cell.2011.02.013

5. Rathmell WK, Rathmell JC, Linehan WM. Metabolic pathways in kidney cancer: current therapies and future directions. *J Clin Oncol Off J Am Soc Clin Oncol*. October 2018:JCO2018792309. doi:10.1200/JCO.2018.79.2309

6. Tang S, Meng MV, Slater JB, Gordon JW, Vigneron DB, Stohr BA, et al. Metabolic imaging with hyperpolarized 13C pyruvate magnetic resonance imaging in patients with renal tumors—Initial experience. *Cancer*. 2021;127(15):2693-2704. doi:https://doi.org/10.1002/cncr.33554

7. Ursprung S, Woitek R, McLean MA, Priest AN, Crispin-Ortuzar M, Brodie CR, et al. Hyperpolarized 13C-Pyruvate Metabolism as a Surrogate for Tumor Grade and Poor

Outcome in Renal Cell Carcinoma—A Proof of Principle Study. *Cancers*. 2022;14(2):335. doi:10.3390/cancers14020335

8. Wang ZJ, Westphalen AC, Zagoria RJ. CT and MRI of small renal masses. *Br J Radiol*. 2018;91(1087):20180131. doi:10.1259/bjr.20180131

9. van Oostenbrugge TJ, Fütterer JJ, Mulders PFA. Diagnostic Imaging for Solid Renal Tumors: A Pictorial Review. *Kidney Cancer*. 2(2):79-93. doi:10.3233/KCA-180028

10. Kang SK, Huang WC, Pandharipande PV, Chandarana H. Solid renal masses: what the numbers tell us. *AJR Am J Roentgenol*. 2014;202(6):1196-1206. doi:10.2214/AJR.14.12502

CHAPTER 2: BACKGROUND

2.1 MRI

MRI and Nuclear Magnetic Resonance (NMR), which forms the foundation of MRI, involves atomic nuclei and nuclear spin physics. In MRI, any NMR active nuclei (nuclei with an odd number of protons) can be imaged, but in most MRI applications, hydrogens (protons) are imaged.

Table 2.1: Select NMR active nuclei with nuclear spin number, gyromagnetic ratio and natural abundance.

Nucleus	Spin	Gyromagnetic Ratio, γ [MHz/T]	Natural Abundance [%]
^{1}H	1/2	42.58	99.99
^{3}He	1/2	32.43	0.0001
^{13}C	1/2	10.71	1.108
^{19}F	1/2	40.06	100.0
^{23}Na	3/2	11.26	100.0
^{31}P	1/2	17.24	100.0
^{129}Xe	1/2	11.78	26.44

Under a magnetic field (B_0), nuclear spins either align in the direction of the magnetic field (Z-direction) or the opposite direction. A slight majority align in the direction of the magnetic field creating a net magnetization, M = [Mx, My, Mz], aligned in the direction of the magnetic field. Within this magnetic field, the nuclear spins precess, and the frequency at which they precess is given by the Larmor equation:

$$\omega = \gamma B_0 \tag{2.1}$$

Where ω is the angular precession frequency, γ is the gyromagnetic ratio, a property of the nuclei, and B_0 is the strength of the magnetic field. The B_0 magnetic field, also called the main magnetic field, sets the stage to make MRI possible.

At equilibrium, the net magnetization points along the direction of the magnetic field, the longitudinal (Z) direction by convention. Radiofrequency (RF) excitation pulses tuned to the same precession frequency as the spins (also known as "on resonance") are used to perturb the spins under B_0 towards the transverse (X, Y) plane. Relaxation times (T_1, T_2) govern how the spins react to the RF pulses. The T_1 or spin-lattice relaxation time describes the recovery of longitudinal (Z) magnetization. The T_2 or spin-spin relaxation time describes the dephasing that occurs between individual spins resulting in a loss of net transverse magnetization over time. The relationship between the relaxation times and magnetization over time is described as follows:

$$M_z(t) = M_0(1 - e^{-\frac{t}{T_1}}) \quad 2.2$$

$$M_{xy}(t) = M_0 e^{-\frac{t}{T_2}} \quad 2.3$$

Where M_0 is the initial magnetization, t is time, M_{xy} is the transverse magnetization and M_z is the longitudinal magnetization. The T_1 and T_2 change based on the main magnetic field strength and the tissue properties.

The RF excitations or B_1^+ pulses are transmitted via transmit RF coils. The received signal, also called the free induction decay (FID) is received via receive RF coils that are placed very close to the body. The FID is a decaying oscillating signal, the current generated from the oscillating magnetic field from the oscillating spins.

Gradient coils which sit in between the main magnetic field and the RF coils, encode spatial data. In each spatial dimension (G_x, G_y, G_z), they add a small gradient to the B_0 field in that direction. For frequency encoding (usually denoted to be in X), the gradient is applied during readout such that spatial position corresponds with slightly different precession frequencies. For phase

encoding (usually in Y and sometimes, in Z for 3D imaging), the gradient is turned on and off before readout such that spatial position corresponds with varying accumulated phase. For slice or slab selection, the G_z gradient is turned on during RF excitation such that only spins with a specific frequency (and therefore within the slice) are excited. The gradient fields over time dictate the spatial readout, which can be optimized for fast readouts like echo planar imaging (EPI).

These timings of the gradients along with the RF pulses make up the pulse sequence which can be shown in the form of a pulse sequence diagram:

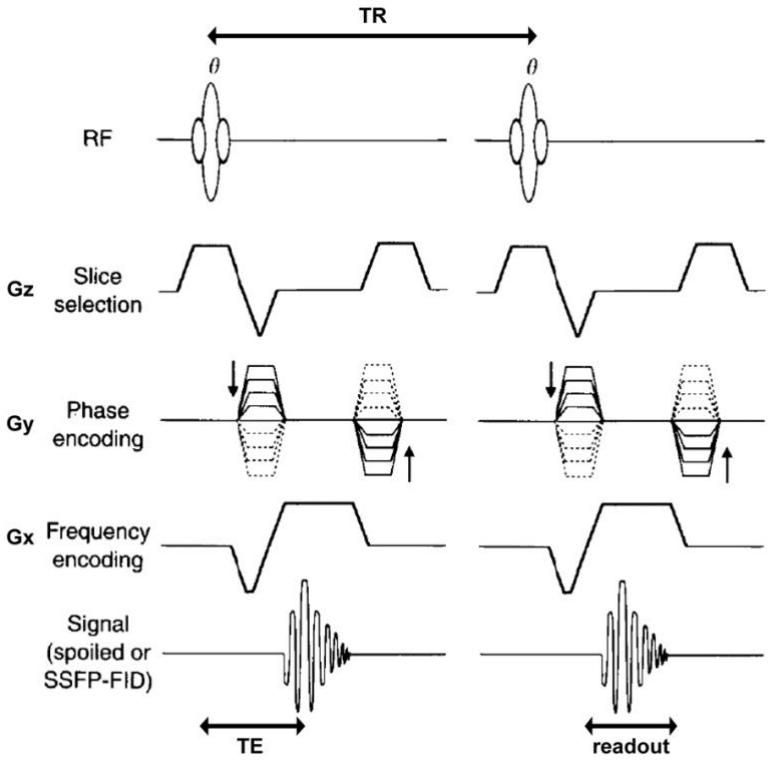

Figure 2.1: Example gradient echo pulse (GRE) pulse sequence diagram with a cartesian readout[1]. First row shows the RF excitation with flip angle Θ, where TR describes the time between subsequent excitations. The slice selection, phase encoding and frequency encoding gradients are shown in the second through fourth lines. For phase encoding, the multiple lines show the change of the amplitude of the gradients for a cartesian readout. The final row shows the FID signal.

The TR or repetition time is the time between subsequent RF excitations and TE, the echo time, is the time between the RF pulse and the FID (signal readout).

The data received from the MRI is filled in a matrix, called k-space, where each location corresponds to a different spatial frequency in the reconstructed image. To reconstruct the image, the 2D or 3D Fourier transform of k-space is used.

2.2 Hyperpolarized [1-^{13}C]Pyruvate MRI

As an alternative to conventional proton MRI, with carbon imaging, the imaging of organic compounds with carbon backbones becomes possible, which is particularly relevant in medicine. As carbon-12 has spin zero and is therefore NMR inactive, its' isotope carbon-13 must instead be imaged (**Table 2.1**). MRI of endogenous carbon-13 is a challenge due to very low SNR compared with protons. Carbon-13 has much lower natural abundance (only ~1% of all carbon), lower concentration in tissue than proton, and a ¼ of the gyromagnetic ratio of protons (**Table 2.1**). These challenges make endogenous carbon-13 MRI infeasible and would necessitate impractically long acquisition times to get SNR like that of proton MRI.

To achieve SNR on the order of proton MRI, two steps must be taken. First, the agent of interest can be enriched with carbon-13 and the enriched carbon-13 compound can be administered to the subject. Second, the Carbon-13 enriched agent must be hyperpolarized. Currently, the most popular method of hyperpolarization for hyperpolarized carbon-13 MRI is via dissolution dynamic nuclear polarization (dDNP). Briefly, with dDNP, microwaves are used to transfer polarization from electron radicals to carbon-13 at very low temperatures and under high

magnetic field. In solution, this results in a 10,000x increase in polarization[2]. A disadvantage of dDNP is outside of the magnetic field, the carbon-13 quickly loses polarization governed by the T_1 time decay constant specific to carbon-13 and the compound. Unlike proton MRI, there is no T_1 recovery of magnetization. In practice, this necessitates quick injection after removal from the magnetic field. To speed up the process, dissolution with heated water is used to quickly bring the hyperpolarized solution to body temperature for injection. Preclinical and clinical hyperpolarizers are available that can boost polarization up to 30-40%. With carbon-13 enrichment and dDNP hyperpolarization, in vivo carbon-13 MRI is feasible.

2.2.1 Pyruvate Metabolism

The utility of carbon-13 MRI is governed by the choice of the carbon-13 enriched agent used. Currently, the most popular molecule used is pyruvate and hyperpolarized [1-^{13}C]pyruvate MRI is the focus of this work. However, other compounds such as urea[3,4], bicarbonate[5–7], fumarate[8,9] and more have also been studied with success.

Pyruvate is useful to image due to its location in the metabolic pathway. Through glycolysis, glucose is converted to pyruvate as a precursor to several metabolic pathways. Pyruvate is converted to lactate via lactate dehydrogenase (LDH) through anaerobic fermentation. Pyruvate is shuttled into the mitochondria as input into the TCA cycle (and creates bicarbonate as a byproduct). Pyruvate is also converted to alanine via alanine aminotransferase (ALT) during transamination.

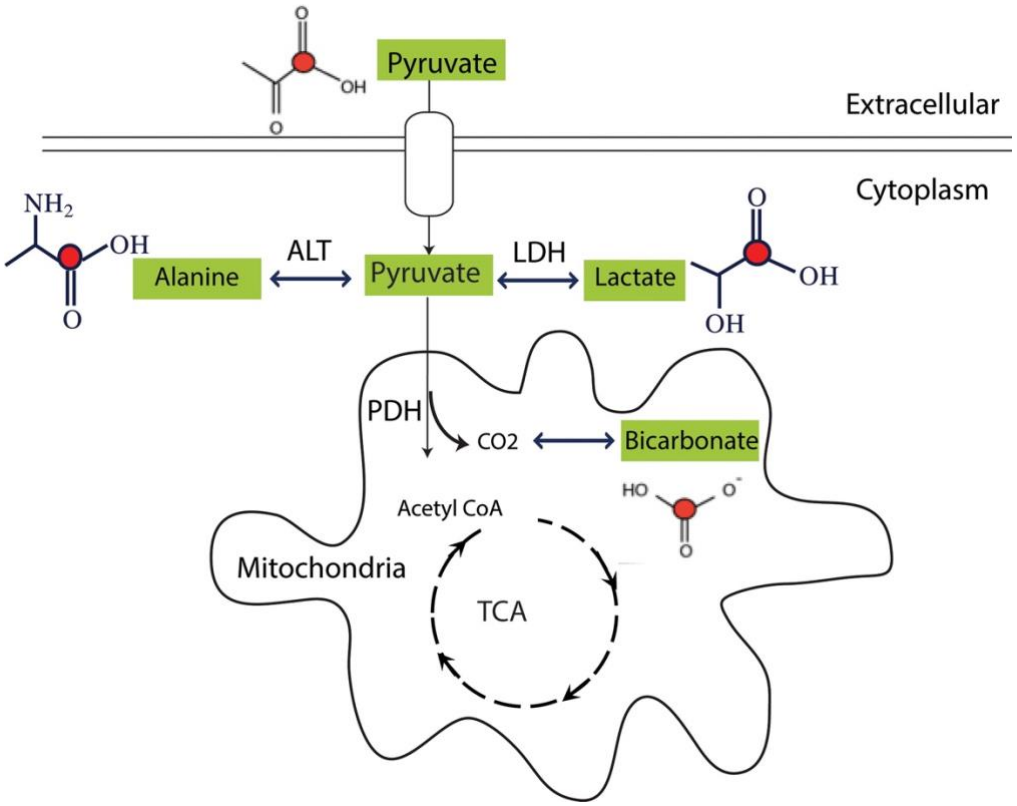

Figure 2.2: Pyruvate metabolic pathways and metabolites of interest. Red circle denotes the ^{13}C -labelled carbon[10]. Pyruvate is transported into the cell where it is converted to lactate, alanine or bicarbonate via the enzymes lactate dehydrogenase (LDH), alanine aminotransferase (ALT) or pyruvate dehydrogenase (PDH).

During hyperpolarized [1-^{13}C]pyruvate MR preparation, the 1st Carbon in pyruvate is labelled with the hyperpolarized carbon-13 and as pyruvate takes each of these metabolic pathways converts to ^{13}C labelled lactate, bicarbonate and alanine. Using MRI, we can take advantage of the unique chemical shifts of [1-^{13}C]pyruvate and its metabolites to image metabolic maps of each metabolite, directly probing the various metabolic pathways.

The first in-human MRI study using hyperpolarized [1-^{13}C]pyruvate was completed in 2013 at UCSF in prostate patients[11] initiating new research into technical advances and clinical applications.

2.2.2 RF Excitations, Readouts & Pulse Sequences

As multiple metabolites are being imaged, one acquisition strategy is spectroscopic imaging (MRSI), where for each spatial location the continuous chemical shift spectrum is acquired. The spectrum can then be analyzed to derive metabolite maps using the chemical shifts of each metabolite. One MRSI technique of interest is phase-encoded chemical shift imaging (CSI). With CSI, the spectrum of each voxel is acquired during one TR and phase encodes are used to move to a new voxel, requiring Nx x Ny RF excitations (where Nx and Ny are the number of voxels in X and Y). One large disadvantage of CSI is that it is slow, which makes it difficult to acquire high resolution data or across larger FOVs[12,13]. Faster methods for MRSI have been developed such as echo planer spectroscopic imaging (EPSI) strategies, which acquire both one row of imaging data and spectra for each voxel in one TR[14].

As an alternative to MRSI, metabolite-specific imaging is a more flexible and faster method. With metabolite-specific imaging, spectral-spatial (spsp) RF excitations are used not only for slice or slab selection but also to excite only certain chemical shift frequencies[15]. Using a spectral-spatial RF excitation centered around the frequency of the metabolite of interest, fast readout methods, like those used in proton MRI can be leveraged to directly image maps of the metabolite. During metabolite-specific imaging, an image of pyruvate is acquired using a spsp RF excitation centered around the frequency of pyruvate, then the center frequency of the spsp RF pulse is shifted to the frequency of a metabolite, for example lactate, to acquire a lactate map. The center frequency can then be shifted back to pyruvate and so on to acquire interleaved images of pyruvate and lactate dynamically. Common fast readouts for metabolite-specific imaging are echo planar imaging (EPI) or spiral[16–19].

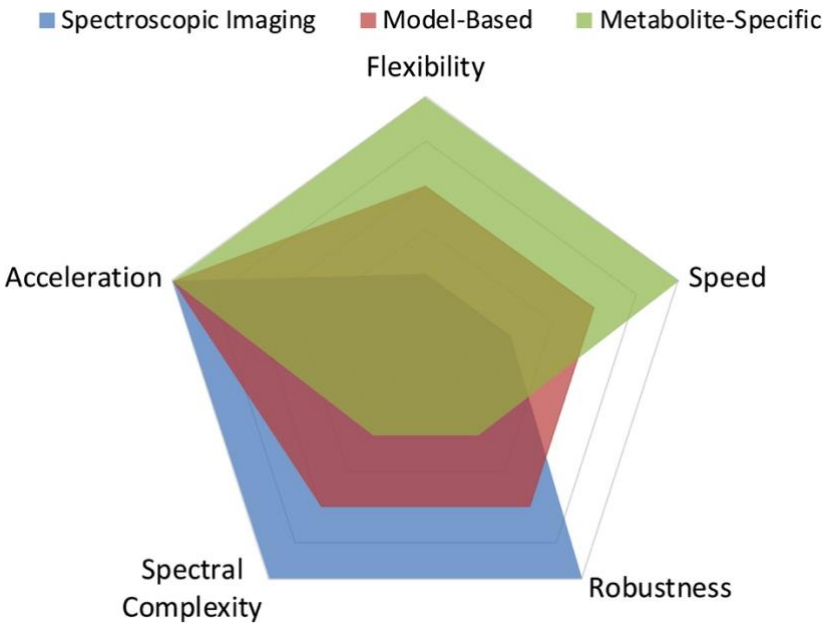

Figure 2.3: The advantages and disadvantages of imaging methods for Hyperpolarized ^{13}C MRI[20]. Spectroscopic imaging works best with complex spectra but is slow. In contrast, metabolite-specific imaging requires sparse spectra but is more flexible and faster.

Recently, metabolite-specific balanced steady state free precession (bSSFP) pulse sequences have been applied to hyperpolarized [1-^{13}C]Pyruvate MRI. The advantage of bSSFP sequences is that they refocus the transverse magnetization at every TR instead of a typical spoiled gradient echo (GRE) sequence[21]. This is particularly important for hyperpolarized experiments where there is no magnetization recovery. Using a metabolite-specific bSSFP sequence for hyperpolarized C13 metabolites has shown to improve the SNR of lactate[19], bicarbonate[22] and urea[23] by 2-3x.

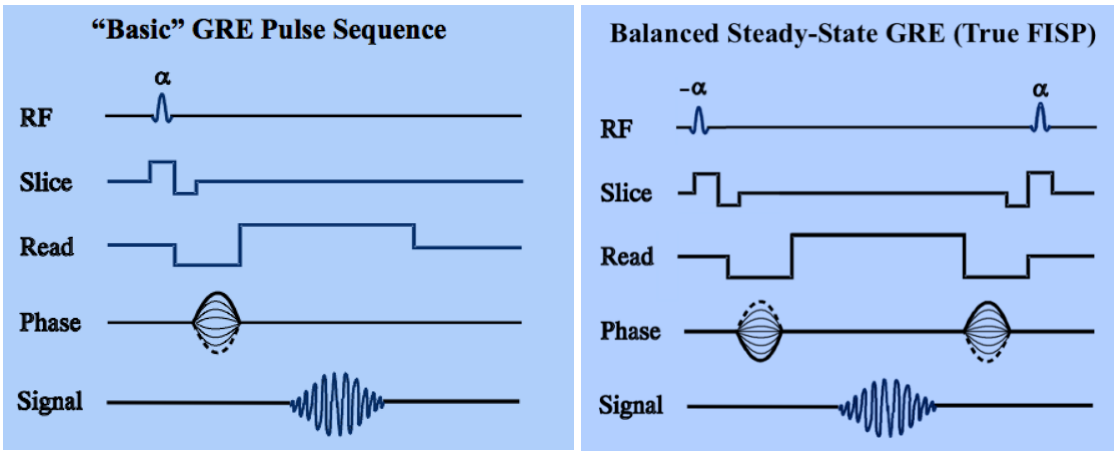

Figure 2.4: Spoiled GRE pulse sequence diagram (left) versus a bSSFP pulse sequence diagram (right). In bSSFP sequences, the gradients are balanced each TR (i.e. sum to 0) and the RF excitations alternate. (Images courtesy of Allen D. Elster, MRIquestions.com [24,25].)

2.2.3 Quantification & Pharmacokinetic Modeling

Area under the curve (AUC) ratios, computed by summing the metabolite data over time, have previously been used to normalize the downstream metabolite signal by pyruvate. Although uncomplicated and quick to compute, it is challenging to compare AUC ratios across patients or studies. AUC ratios are affected by flip angles used, bolus timings and bolus characteristics.

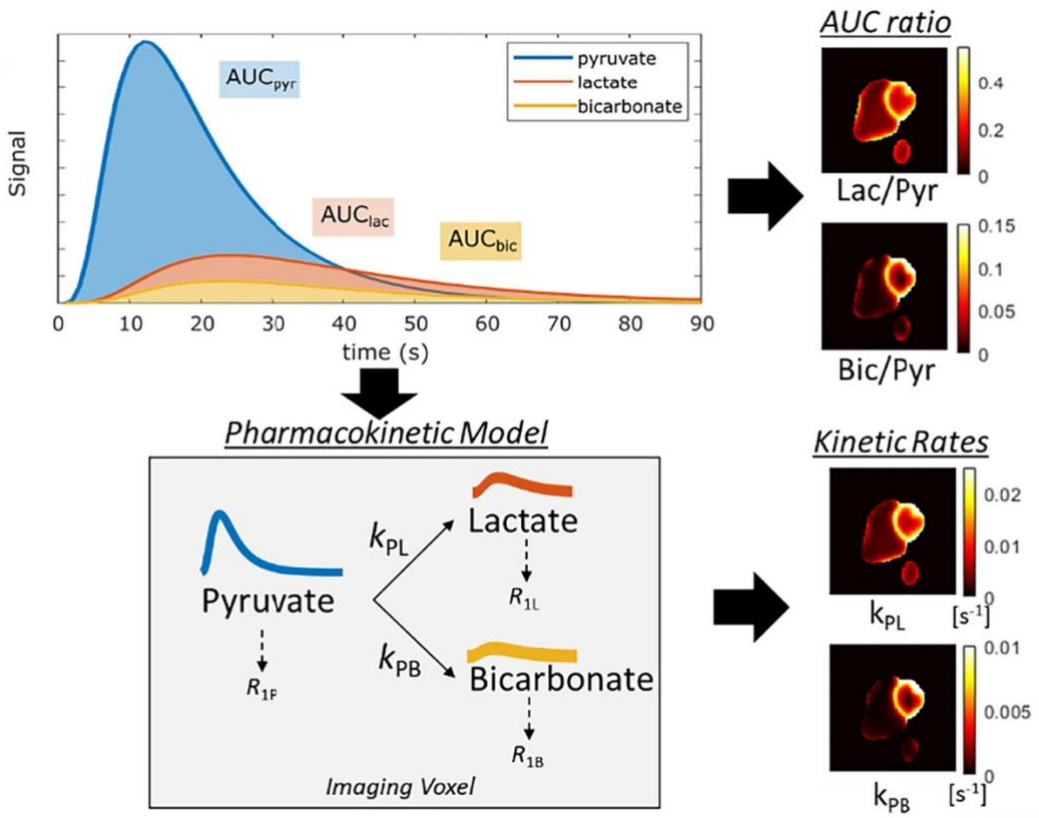

Figure 2.5: Overview of quantification methods for Hyperpolarized [1-^{13}C]Pyruvate[26]. AUC ratio maps are derived from taking the sum of the dynamics and dividing the AUCs of the downstream metabolites (lactate, bicarbonate) by the pyruvate AUC. For the pharmacokinetic model the dynamics are fit to the model per voxel to get rate constant (k_{PL} and k_{PB}) maps. Pyr = pyruvate, Lac = lactate, Bic = bicarbonate, AUC = area under the curve

In an alternative approach, the pharmacokinetics of pyruvate and lactate can be modeled as a set of differential equations[27–30]. The pharmacokinetic (PK) model used can increase in complexity based on the number of physical compartments (**Figure 2.6**). Although more physical compartments (such as vasculature, intracellular, extracellular) may more accurately model the biochemistry, there are more unknown parameters that cannot be acquired with imaging which must also be estimated or fit[27]. In the one physical compartment case, the whole body is considered as a single homogeneous compartment. The one physical compartment model for pyruvate and lactate can be described with the following equations[30]:

$$\frac{dP_z(t)}{dt} = -R_{1P}P_z(t) - k_{PL}P_z(t) + u(t) \quad 2.4$$

$$\frac{dP_z(t)}{dt} = -R_{1P}P_z(t) - k_{PL}P_z(t) + u(t) \quad 2.5$$

Where P_z and L_z are the longitudinal components of pyruvate and lactate respectively, k_{PL} is the apparent pyruvate-to-lactate rate constant, R_{1P} and R_{1L} are the reciprocal of pyruvate and lactate T_1, and u(t) is the input function. Note that this is a uni-directional model, meaning that it is assumed that the lactate-to-pyruvate conversion, k_{LP}, is zero.

The apparent rate constant, k_{PL}, is a quantitative marker representing anaerobic fermentation. The model can be extended to the other metabolites to fit k_{PB} and k_{PA}, the rate constants representing pyruvate to bicarbonate and alanine conversion, respectively.

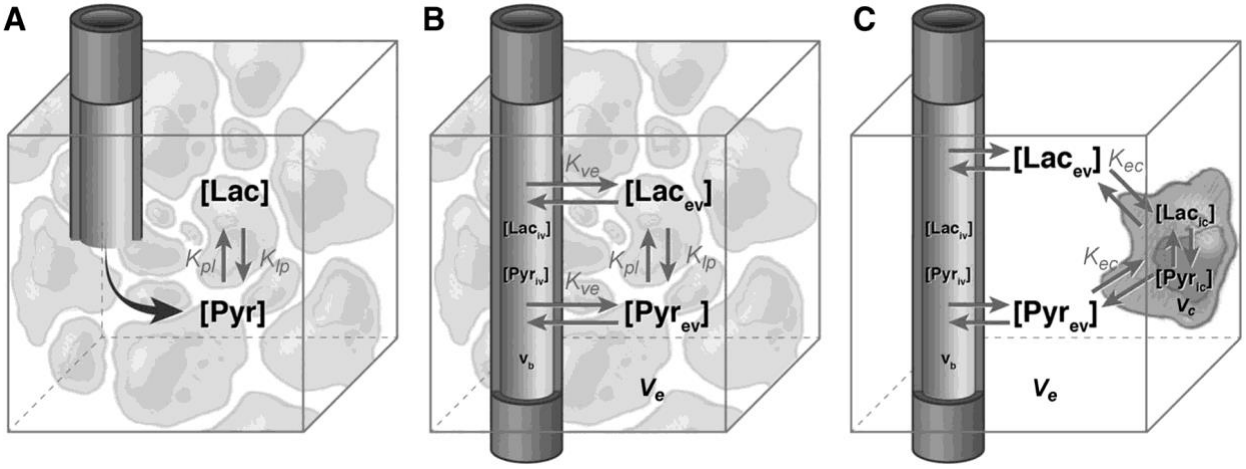

Figure 2.6: Visual representations of a one physical compartment (A), two physical compartment (B) and three physical compartment (C) pharmacokinetic (PK) model[27]. For the one compartment model, the full pool of pyruvate can convert to lactate, In the two compartment model, the intervascular (iv) compartment is separate and pyruvate can only convert to lactate in the extravascular (ev) compartment. For the three compartment model, there is a further intracellular compartment (ic), where pyruvate can only convert to lactate in the intracellular compartment.

By solving the differential equations, a function can be derived between the metabolite dynamics and the rate constants. Then using least-squares fitting or similar techniques, the metabolite maps

can be used to fit rate constants per voxel to create rate constant maps. As flip angles, and bolus characteristics are inputs into the model, the apparent rate constants can be compared across patients and institutions.

2.3 Renal Cell Carcinoma

According to the American Cancer Society, there will be an estimated 81,610 new cases of kidney and renal pelvis cancers in 2024[31]. Improvement in imaging technologies has increased the rate of incidental discoveries of small renal masses[32]. For these new discoveries, it is more important than ever to be able to characterize these masses for proper treatment planning.

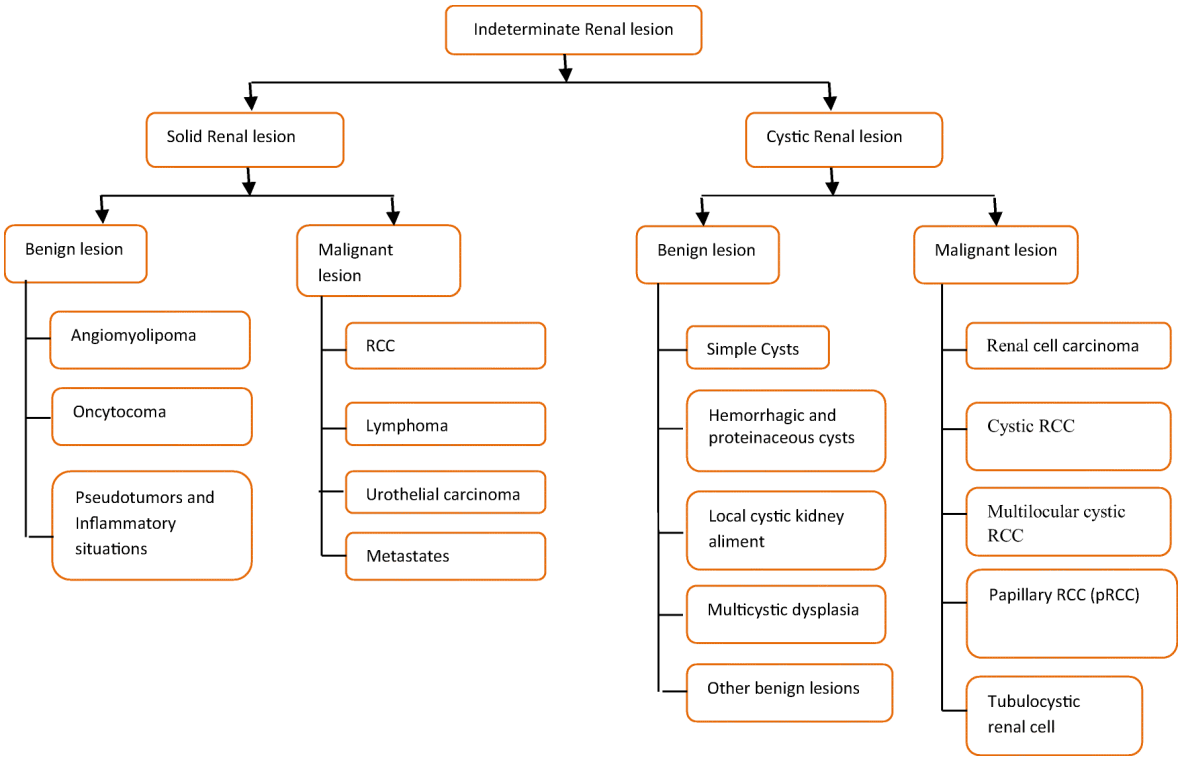

Figure 2.7: Diagram of groupings and pathologies of renal lesions, including malignant renal cell carcinoma (RCC), benign angiomyolipoma and benign oncocytoma[33].

Renal cell carcinomas (RCCs) are the most common renal malignancy. Renal cell carcinomas are divided into three main pathological subgroups: clear cell RCC (ccRCC) which is up to 80% of

RCCs, papillary RCC (pRCC) which is about 10%, and chromophobe RCC (chRCC) about 5%[34,35]. The most common benign renal tumors include angiomyolipoma (AML) and oncocytomas.

Standard of care for RCC, includes initial diagnosis and TNM staging using ultrasound or pre- and post-contrast CT. Typically, this leads to surgical resection of the tumor in form of a partial or radical nephrectomy. If the pathology is unclear, percutaneous needle core biopsy is used. Fuhrman grading based on histology is additionally used to assign a grade to the tumor based on appearance of cell nuclei[36]. The International Society of Urological Pathology (ISUP) has more recently updated tumor grading guidelines and stated chRCC should not be graded[37]. Of localized (stage T1) renal tumors, around 80% were found to be low-grade[38] and would not require resection, and instead would benefit from active surveillance[39].

2.3.1 CT of RCC

The most common imaging method used for renal mass diagnosis and staging is Computed Tomography (CT). An optimal CT protocol for RCC diagnosis typically includes an unenhanced CT along with post-contrast phases: corticomedullary (25-40 seconds after contrast administration) and nephrogenic (90-120 seconds after contrast administration)[35,40]. AML with macroscopic fat can be distinguished from RCC using CT alone. However, it is challenging to distinguish lipid-poor AML and oncocytomas from RCC with CT[35,40–42].

2.3.2 RCC Metabolism

The reprogramming of metabolism is a hallmark of cancer[43]. Called the Warburg effect, tumor cells, unlike healthy cells, even in the presence of oxygen, rely more heavily on lactate fermentation than respiration for metabolism[44] (**Figure 2.8**). RCC exhibits the Warburg effect[45], and previous studies have shown increased LDHA in RCC tumor cells compared with healthy through immunohistochemistry[46], gene expression[47] and proteomics/metabolomics analysis[48]. Girgis et al.[47] reports an increase in LDHA expression for increasing RCC tumor grade. Sriram et al.[49] found a significant increase in mean LDHA expression in ccRCC compared with both healthy tissues and benign tumors (AML and oncocytoma).

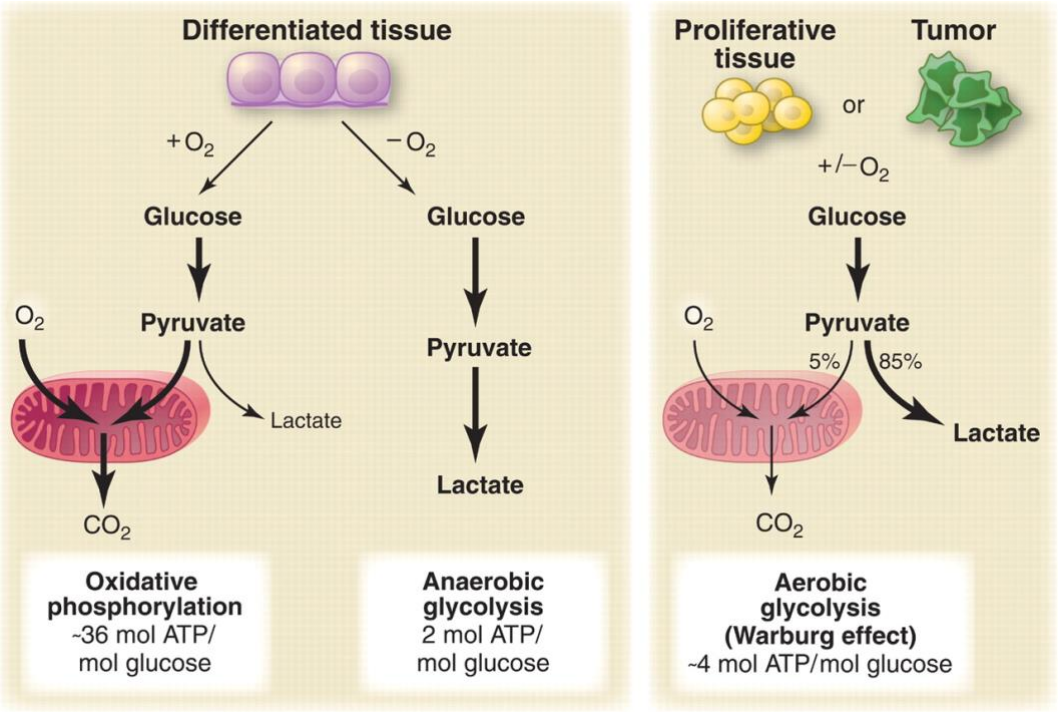

Figure 2.8: Graphical representation of the Warburg effect[50]. Tumor cells, regardless of the availability of oxygen, favor fermentation (pyruvate to lactate conversion) over the TCA cycle and oxidative phosphorylation.

Hyperpolarized [1-^{13}C]Pyruvate MRI can also be used to capture the Warburg-like metabolism in RCC. In xenograft rat models, Sriram et al.[51] investigated three different RCC cell lines and

found the cell line with the highest LDHA expression, also had the highest pyruvate-to-lactate conversion as assessed with Hyperpolarized [1-^{13}C]Pyruvate MRI. In human Hyperpolarized [1-^{13}C]Pyruvate MRI studies, increasing WHO/ISUP tumor grade has shown to correlate with median k_{PL} in ccRCC[52]. Another study showed that an increase in hyperpolarized ^{13}C-Lactate over ^{13}C-Pyruvate ratio correlated with increasing ccRCC tumor grade[53].

2.4 References

1. Bernstein MA, King KF, Zhou XJ. *Handbook of MRI Pulse Sequences*.; 2004.

2. Ardenkjær-Larsen JH, Fridlund B, Gram A, Hansson G, Hansson L, Lerche MH, et al. Increase in signal-to-noise ratio of > 10,000 times in liquid-state NMR. *Proc Natl Acad Sci*. 2003;100(18):10158-10163. doi:10.1073/pnas.1733835100

3. Reed GD, von Morze C, Bok R, Koelsch BL, Van Criekinge M, Smith KJ, et al. High Resolution 13C MRI With Hyperpolarized Urea: In Vivo T2 Mapping and 15N Labeling Effects. *IEEE Trans Med Imaging*. 2014;33(2):362-371. doi:10.1109/TMI.2013.2285120

4. Reed GD, von Morze C, Verkman AS, Koelsch BL, Chaumeil MM, Lustig M, et al. Imaging Renal Urea Handling in Rats at Millimeter Resolution Using Hyperpolarized Magnetic Resonance Relaxometry. *Tomography*. 2016;2(2):125-137. doi:10.18383/j.tom.2016.00127

5. Gallagher FA, Kettunen MI, Day SE, Hu DE, Ardenkjær-Larsen JH, Zandt R in 't, et al. Magnetic resonance imaging of pH in vivo using hyperpolarized 13C-labelled bicarbonate. *Nature*. 2008;453(7197):940-943. doi:10.1038/nature07017

6. Mu C, Liu X, Kim Y, Riselli A, Korenchan DE, Bok RA, et al. Clinically Translatable Hyperpolarized ^{13}C Bicarbonate pH Imaging Method for Use in Prostate Cancer. *ACS Sens*. 2023;8(11):4042-4054. doi:10.1021/acssensors.3c00851

7. Scholz DJ, Otto AM, Hintermair J, Schilling F, Frank A, Köllisch U, et al. Parameterization of hyperpolarized (13)C-bicarbonate-dissolution dynamic nuclear polarization. *Magma N Y N*. 2015;28(6):591-598. doi:10.1007/s10334-015-0500-9

8. Gallagher FA, Kettunen MI, Hu DE, Jensen PR, Zandt RI 't, Karlsson M, et al. Production of hyperpolarized [1,4-13C2]malate from [1,4-13C2]fumarate is a marker of cell necrosis and treatment response in tumors. *Proc Natl Acad Sci U S A*. 2009;106(47):19801-19806. doi:10.1073/pnas.0911447106

9. Clatworthy MR, Kettunen MI, Hu DE, Mathews RJ, Witney TH, Kennedy BWC, et al. Magnetic resonance imaging with hyperpolarized [1,4-13C2]fumarate allows detection of early renal acute tubular necrosis. *Proc Natl Acad Sci*. 2012;109(33):13374-13379. doi:10.1073/pnas.1205539109

10. Wang ZJ, Ohliger MA, Larson PEZ, Gordon JW, Bok RA, Slater J, et al. Hyperpolarized 13C MRI: State of the Art and Future Directions. *Radiology*. 2019;291(2):273-284. doi:10.1148/radiol.2019182391

11. Nelson S, Kurhanewicz J, Vigneron D, Larson P, Harzstark A, Ferrone M, et al. Metabolic Imaging of Patients with Prostate Cancer Using Hyperpolarized [1-13C]Pyruvate. *Sci Transl Med*. 2013;5(198):198ra108. doi:10.1126/scitranslmed.3006070

12. Golman K, in 't Zandt R, Thaning M. Real-time metabolic imaging. *Proc Natl Acad Sci*. 2006;103(30):11270-11275. doi:10.1073/pnas.0601319103

13. Kohler S j., Yen Y, Wolber J, Chen A p., Albers M j., Bok R, et al. In vivo 13carbon metabolic imaging at 3T with hyperpolarized 13C-1-pyruvate. *Magn Reson Med*. 2007;58(1):65-69. doi:10.1002/mrm.21253

14. Yen YF, Kohler S j., Chen A p., Tropp J, Bok R, Wolber J, et al. Imaging considerations for in vivo 13C metabolic mapping using hyperpolarized 13C-pyruvate. *Magn Reson Med*. 2009;62(1):1-10. doi:10.1002/mrm.21987

15. Meyer CH, Pauly JM, Macovskiand A, Nishimura DG. Simultaneous spatial and spectral selective excitation. *Magn Reson Med*. 1990;15(2):287-304. doi:10.1002/mrm.1910150211

16. Cunningham CH, Chen AP, Lustig M, Hargreaves BA, Lupo J, Xu D, et al. Pulse sequence for dynamic volumetric imaging of hyperpolarized metabolic products. *J Magn Reson*. 2008;193(1):139-146. doi:10.1016/j.jmr.2008.03.012

17. Gordon JW, Vigneron DB, Larson PEZ. Development of a symmetric echo planar imaging framework for clinical translation of rapid dynamic hyperpolarized 13C imaging. *Magn Reson Med*. 2017;77(2):826-832. doi:10.1002/mrm.26123

18. Cunningham CH, Lau JYC, Chen AP, Geraghty BJ, Perks WJ, Roifman I, et al. Hyperpolarized 13C Metabolic MRI of the Human Heart: Initial Experience. *Circ Res*. 2016;119(11):1177-1182. doi:10.1161/CIRCRESAHA.116.309769

19. Tang S, Bok R, Qin H, Reed G, VanCriekinge M, Delos Santos R, et al. A metabolite-specific 3D stack-of-spiral bSSFP sequence for improved lactate imaging in hyperpolarized [1- 13 C]pyruvate studies on a 3T clinical scanner. *Magn Reson Med*. 2020;84(3):1113-1125. doi:10.1002/mrm.28204

20. Gordon JW, Chen HY, Dwork N, Tang S, Larson PEZ. Fast Imaging for Hyperpolarized MR Metabolic Imaging. *J Magn Reson Imaging*. 2021;53(3):686-702. doi:https://doi.org/10.1002/jmri.27070

21. Bieri O, Scheffler K. Fundamentals of balanced steady state free precession MRI. *J Magn Reson Imaging*. 2013;38(1):2-11. doi:10.1002/jmri.24163

22. Liu X, Tang S, Cui D, Bok RA, Chen HY, Gordon JW, et al. A metabolite specific 3D stack-of-spirals bSSFP sequence for improved bicarbonate imaging in hyperpolarized [1-13C]Pyruvate MRI. *J Magn Reson*. 2023;353:107518. doi:10.1016/j.jmr.2023.107518

23. Liu X, Tang S, Mu C, Qin H, Cui D, Lai YC, et al. Development of specialized magnetic resonance acquisition techniques for human hyperpolarized [13C,15N2]urea + [1-13C]pyruvate simultaneous perfusion and metabolic imaging. *Magn Reson Med*. 2022;88(3):1039-1054. doi:10.1002/mrm.29266

24. Elster AD. GRASS/FISP. Questions and Answers in MRI. http://mriquestions.com/grassfisp-how.html. Accessed August 1, 2024.

25. Elster AD. True FISP/FIESTA. Questions and Answers in MRI. http://mriquestions.com/true-fispfiesta.html. Accessed August 1, 2024.

26. Larson PEZ, Tang S, Liu X, Sinha A, Dwork N, Sivalokanathan S, et al. Regional quantification of cardiac metabolism with hyperpolarized [1-13C]-pyruvate CMR evaluated in an oral glucose challenge. *J Cardiovasc Magn Reson*. 2023;25(1):77. doi:10.1186/s12968-023-00972-7

27. Bankson JA, Walker CM, Ramirez MS, Stefan W, Fuentes D, Merritt ME, et al. Kinetic modeling and constrained reconstruction of hyperpolarized [1-13C]-pyruvate offers improved metabolic imaging of tumors. *Cancer Res*. 2015;75(22):4708-4717. doi:10.1158/0008-5472.CAN-15-0171

28. Khegai O, Schulte RF, Janich MA, Menzel MI, Farrell E, Otto AM, et al. Apparent rate constant mapping using hyperpolarized [1–13C]pyruvate. *NMR Biomed*. 2014;27(10):1256-1265. doi:10.1002/nbm.3174

29. Hill DK, Orton MR, Mariotti E, Boult JKR, Panek R, Jafar M, et al. Model Free Approach to Kinetic Analysis of Real-Time Hyperpolarized 13C Magnetic Resonance Spectroscopy Data. *PLOS ONE*. 2013;8(9):e71996. doi:10.1371/journal.pone.0071996

30. Larson PEZ, Chen HY, Gordon JW, Korn N, Maidens J, Arcak M, et al. Investigation of analysis methods for hyperpolarized 13C-pyruvate metabolic MRI in prostate cancer patients. *NMR Biomed*. 2018;31(11):1-17. doi:10.1002/nbm.3997

31. Siegel RL, Giaquinto AN, Jemal A. Cancer statistics, 2024. *CA Cancer J Clin*. 2024;74(1):12-49. doi:10.3322/caac.21820

32. Patard JJ. Incidental renal tumours. *Curr Opin Urol*. 2009;19(5):454-458. doi:10.1097/MOU.0b013e32832f0ccd

33. Kaur R, Juneja M, Mandal AK. An overview of non-invasive imaging modalities for diagnosis of solid and cystic renal lesions. *Med Biol Eng Comput*. 2020;58(1):1-24. doi:10.1007/s11517-019-02049-z

34. Reuter VE. The Pathology of Renal Epithelial Neoplasms. *Semin Oncol*. 2006;33(5):534-543. doi:10.1053/j.seminoncol.2006.06.009

35. Wang ZJ, Westphalen AC, Zagoria RJ. CT and MRI of small renal masses. *Br J Radiol*. 2018;91(1087):20180131. doi:10.1259/bjr.20180131

36. Fuhrman SA, Lasky LC, Limas C. Prognostic significance of morphologic parameters in renal cell carcinoma. *Am J Surg Pathol*. 1982;6(7):655-663. doi:10.1097/00000478-198210000-00007

37. Samaratunga H, Gianduzzo T, Delahunt B. The ISUP system of staging, grading and classification of renal cell neoplasia. *J Kidney Cancer VHL*. 2014;1(3):26-39. doi:10.15586/jkcvhl.2014.11

38. Rothman J, Egleston B, Wong YN, Iffrig K, Lebovitch S, Uzzo RG. Histopathological characteristics of localized renal cell carcinoma correlate with tumor size: a SEER analysis. *J Urol*. 2009;181(1):29-33; discussion 33-34. doi:10.1016/j.juro.2008.09.009

39. Gordetsky J, Eich ML, Garapati M, Del Carmen Rodriguez Pena M, Rais-Bahrami S. Active Surveillance of Small Renal Masses. *Urology*. 2019;123:157-166. doi:10.1016/j.urology.2018.09.017

40. van Oostenbrugge TJ, Fütterer JJ, Mulders PFA. Diagnostic Imaging for Solid Renal Tumors: A Pictorial Review. *Kidney Cancer*. 2(2):79-93. doi:10.3233/KCA-180028

41. Krishna S, Murray CA, McInnes MD, Chatelain R, Siddaiah M, Al-Dandan O, et al. CT imaging of solid renal masses: pitfalls and solutions. *Clin Radiol*. 2017;72(9):708-721. doi:10.1016/j.crad.2017.05.003

42. Kang SK, Huang WC, Pandharipande PV, Chandarana H. Solid renal masses: what the numbers tell us. *AJR Am J Roentgenol*. 2014;202(6):1196-1206. doi:10.2214/AJR.14.12502

43. Hanahan D, Weinberg RA. Hallmarks of Cancer: The Next Generation. *Cell*. 2011;144(5):646-674. doi:10.1016/j.cell.2011.02.013

44. Warburg O. On the origin of cancer cells. *Science*. 1956;123(3191):309-314. doi:10.1126/science.123.3191.309

45. Rathmell WK, Rathmell JC, Linehan WM. Metabolic pathways in kidney cancer: current therapies and future directions. *J Clin Oncol Off J Am Soc Clin Oncol*. October 2018:JCO2018792309. doi:10.1200/JCO.2018.79.2309

46. Singer K, Kastenberger M, Gottfried E, Hammerschmied CG, Büttner M, Aigner M, et al. Warburg phenotype in renal cell carcinoma: High expression of glucose-transporter 1 (GLUT-1) correlates with low CD8+ T-cell infiltration in the tumor. *Int J Cancer*. 2011;128(9):2085-2095. doi:https://doi.org/10.1002/ijc.25543

47. Girgis H, Masui O, White NM, Scorilas A, Rotondo F, Seivwright A, et al. Lactate Dehydrogenase A is a potential prognostic marker in clear cell renal cell carcinoma. *Mol Cancer*. 2014;13:101. doi:10.1186/1476-4598-13-101

48. Wettersten HI, Hakimi AA, Morin D, Bianchi C, Johnstone ME, Donohoe DR, et al. Grade-dependent metabolic reprogramming in kidney cancer revealed by combined proteomics and metabolomics analysis. *Cancer Res*. 2015;75(12):2541-2552. doi:10.1158/0008-5472.CAN-14-1703

49. Sriram R, Criekinge MV, Santos JD, Keshari KR, Wilson DM, Peehl D, et al. Non-Invasive Differentiation of Benign Renal Tumors from Clear Cell Renal Cell Carcinomas Using

Clinically Translatable Hyperpolarized 13C Pyruvate Magnetic Resonance. *Tomography*. 2016;2(1):35-42. doi:10.18383/j.tom.2016.00106

50. Vander Heiden MG, Cantley LC, Thompson CB. Understanding the Warburg Effect: The Metabolic Requirements of Cell Proliferation. *Science*. 2009;324(5930):1029-1033. doi:10.1126/science.1160809

51. Sriram R, Gordon J, Baligand C, Ahamed F, Delos Santos J, Qin H, et al. Non-Invasive Assessment of Lactate Production and Compartmentalization in Renal Cell Carcinomas Using Hyperpolarized 13C Pyruvate MRI. *Cancers*. 2018;10(9):313. doi:10.3390/cancers10090313

52. Ursprung S, Woitek R, McLean MA, Priest AN, Crispin-Ortuzar M, Brodie CR, et al. Hyperpolarized 13C-Pyruvate Metabolism as a Surrogate for Tumor Grade and Poor Outcome in Renal Cell Carcinoma—A Proof of Principle Study. *Cancers*. 2022;14(2):335. doi:10.3390/cancers14020335

53. Tang S, Meng MV, Slater JB, Gordon JW, Vigneron DB, Stohr BA, et al. Metabolic imaging with hyperpolarized 13C pyruvate magnetic resonance imaging in patients with renal tumors—Initial experience. *Cancer*. 2021;127(15):2693-2704. doi:https://doi.org/10.1002/cncr.33554

CHAPTER 3: METABOLITE-SPECIFIC ECHO PLANAR IMAGING FOR PRECLINICAL STUDIES WITH HYPERPOLARIZED 13C-PYRUVATE MRI

3.1 Abstract

Metabolite-specific echo-planar imaging (EPI) sequences with spectral–spatial (spsp) excitation are commonly used in clinical hyperpolarized [1-^{13}C]pyruvate studies because of their speed, efficiency, and flexibility. In contrast, preclinical systems typically rely on slower spectroscopic methods, such as chemical shift imaging (CSI). In this study, a 2D spspEPI sequence was developed for use on a preclinical 3T Bruker system and tested on in vivo mice experiments with patient-derived xenograft renal cell carcinoma (RCC) or prostate cancer tissues implanted in the kidney or liver. Compared to spspEPI sequences, CSI were found to have a broader point spread function via simulations and exhibited signal bleeding between vasculature and tumors in vivo. Parameters for the spspEPI sequence were optimized using simulations and verified with in vivo data. The expected lactate SNR and pharmacokinetic modeling accuracy increased with lower pyruvate flip angles (less than 15°), intermediate lactate flip angles (25° to 40°), and temporal resolution of 3 s. Overall SNR was also higher with coarser spatial resolution (4 mm isotropic vs. 2 mm isotropic). Pharmacokinetic modelling used to fit k_{PL} maps showed results consistent with the previous literature and across different sequences and tumor xenografts. This work describes and justifies the pulse design and parameter choices for preclinical spspEPI hyperpolarized ^{13}C-pyruvate studies and shows superior image quality to CSI.

3.2 Introduction

Magnetic resonance imaging (MRI) with hyperpolarized [1-^{13}C]pyruvate, using the dissolution dynamic nuclear-polarization technique, can interrogate key crossroads of metabolism by

measuring whether pyruvate is converted to lactate, alanine, or enters the TCA cycle. Elevated pyruvate to lactate conversion is a hallmark of many cancers, known as the Warburg effect, motivating the use of this modality for cancer imaging. Hyperpolarized ^{13}C-pyruvate MRI is now in clinical trials at 13 institutions worldwide with applications including prostate cancer [1], brain tumors [2], breast cancer [3], kidney cancer [4], kidney disease, liver disease, ischemic heart disease, and cardiomyopathies [5,6].

Metabolite-specific imaging is a popular tool in clinical hyperpolarized [1-^{13}C]pyruvate MRI as it provides excellent performance in terms of speed, coverage, and acquisition flexibility compared to spectroscopic imaging and chemical shift-encoding methods [7–9]. Specifically, this technique uses a spectrally and spatially selective (spsp) excitation pulse followed by a fast imaging readout, such as echo planar imaging (EPI). With a typical spspEPI sequence, one metabolite is excited at a time, and for each metabolite, all of k-space is acquired within one TR. Other metabolite-specific sequences have also been used previously, such as balanced steady-state free precession (bSSFP), which allowed for improved SNR by refocusing transverse magnetization [10,11]. Metabolite-specific imaging has become the optimal choice for hyperpolarized [1-^{13}C]pyruvate studies of tumor metabolism due to the sparsity of spectral information of interest.

Recent optimizations at our institute for clinical spspEPI include mitigation of B_0 inhomogeneities by improved shimming using proton signals [12], avoidance of flip angle variation over time due to its sensitivity to transmit B_1 inhomogeneities, and calibration errors [13], and

incorporation of real-time calibrations of hyperpolarized agent bolus arrival time, B_0, and B_1 to improve the reproducibility and SNR for better quantification [14].

In contrast, the standard for hyperpolarized [1-^{13}C]pyruvate MRI experiments on preclinical imaging systems is a chemical shift imaging (CSI) or non-localized spectroscopic sequences. While this sequence is very robust and requires no knowledge of the chemical shifts, it is also much slower than spspEPI. Fast spectroscopic imaging approaches, such as EPSI, have been developed as an alternative to CSI [15]. However, EPSI sequences still fall short of metabolite-specific sequences, such as spspEPI, in terms of speed and flexibility [8].

There has been limited development of spspEPI ^{13}C sequences on preclinical imaging systems and scarcely any implementation in preclinical in vivo research studies [16,17]. Thus, the objective of this work is to reverse engineer a 2D metabolite-specific clinical EPI protocol to a preclinical imaging system. In this, we include comparisons to CSI sequences, and additionally analyze different acquisition parameters as well as perform rate constant fitting for metabolite-specific EPI in murine studies.

3.3 Materials and Methods

3.3.1 Simulations

Simulations of the hyperpolarized signals were performed to evaluate the expected spatial resolution, SNR, and pharmacokinetic model accuracy for the EPI and CSI sequences. Magnetization decay across the k-space was simulated for both EPI and CSI acquisitions, taking into account RF effects, T_1 decay, and metabolic conversion. The metabolism was simulated

using a pharmacokinetic model with one physical compartment and two chemical pools—pyruvate and lactate [18]. The decay across one TR, from TR = $n - 1$ to n, can be modeled as:

$$M_n = \mathrm{rot}(\alpha) \cdot \mathrm{spoil} \cdot \mathrm{expm}(R \cdot \mathrm{TR}) \cdot M_{n-1} \qquad 3.1$$

where M stores the transverse and longitudinal magnetizations of pyruvate and lactate, i.e., $M = [\mathrm{M_{P,x}}, \mathrm{M_{P,y}}, \mathrm{M_{P,z}}, \mathrm{M_{L,x}}, \mathrm{M_{L,y}}, \mathrm{M_{L,z}}]'$, and expm is a matrix exponential. The matrix R includes relaxation and metabolic conversion and can be defined as:

$$\mathrm{R} = \begin{Bmatrix} 1 & 0 & 0 & 0 & 0 & 0 \\ 0 & 1 & 0 & 0 & 0 & 0 \\ 0 & 0 & -k''_{PL} - R_{1P} & 0 & 0 & 0 \\ 0 & 0 & 0 & 1 & 0 & 0 \\ 0 & 0 & 0 & 0 & 1 & 0 \\ 0 & 0 & k''_{PL} & 0 & 0 & -R_{1L} \end{Bmatrix} \qquad 3.2$$

where k_{PL}" is the effective apparent rate constant and R_{1P} and R_{1L} are the reciprocals of pyruvate and lactate T_1. The matrix rot is a 3D rotation matrix to simulate RF excitation and spoil is a matrix that eliminates transverse magnetization (M_x and M_y) after each TR.

The model used parameters of k_{PL} = 0.05 1/s, $T_{1,\mathrm{pyruvate}}$ = 20 s, and $T_{1,\mathrm{lactate}}$ = 30 s with values chosen based on prior in vivo fitting results. A realistic input function was modelled as a gamma distribution with FWHM of 8 s determined from the previous in vivo datasets. The input function was used to simulate bolus effects and inflow of injected pyruvate.

The point spread function (PSF) was simulated by taking the IFFT of the magnetization decay across k-space. The full width at half maximum (FWHM) was calculated for a y = 0 slice of the PSF, including zero-filling k-space before the IFFT. T_2* blurring effects were not considered due to short EPI readout time (100 ms) and expected relatively long T_2 of metabolites[19].

The pharmacokinetic model was also used to simulate average pyruvate and lactate dynamic curves for EPI. Equation (3.1) can be modified and expanded to multiple time points for an EPI sequence. For time point t, first, pyruvate is acquired:

$$M_{t,P} = \mathrm{rot}_P(\alpha_P) \cdot \mathrm{spoil}_P \cdot (M_{t-1} + U_t)$$
$$P_t = M_{t,P}^{(1)} + iM_{t,P}^{(2)} \qquad 3.3$$

Here, U_t stores the input function for time point t and is added to longitudinal pyruvate magnetization. The matrix $\mathrm{rot_P}$ is a rotation matrix that only rotates pyruvate magnetizations (simulating the spsp RF pulse) and P_t is the complex pyruvate signal for timepoint *t*. Next, lactate is acquired:

$$M_{t,L} = \mathrm{rot}_L(\alpha_L) \cdot \mathrm{spoil}_L \cdot \mathrm{expm}(R \cdot \mathrm{TR}_P) \cdot M_{t,P}$$
$$L_t = M_{t,L}^{(4)} + iM_{t,L}^{(5)} \qquad 3.4$$

Similarly, L_t is the complex lactate signal for timepoint *t*. Finally, relaxation and metabolic conversion at the delay at the end of each timepoint is modeled to arrive at the final magnetization vector, M_t, at the end of timepoint *t*:

$$M_t = \mathrm{expm}\big(R \cdot (\mathrm{TempRes} - \mathrm{TR}_P)\big) \cdot M_{t,L} \qquad 3.5$$

This model was repeated for all timepoints to simulate complex pyruvate and lactate signal over time. The relative SNR was approximated as the sum of the modelled magnitude signal over time. A Monte Carlo simulation was performed using simulated dynamic curves with random noise to fit k_{PL} values [18]. The standard deviation of the fit k_{PL} values across Monte Carlo iterations was calculated as a measure of k_{PL} fitting precision.

3.3.2 Pulse Sequences

A ramp-sampled, symmetric EPI readout with spsp excitation was developed for use on the ParaVision 6.0 Bruker software (Bruker, Billerica, MA, USA). The original EPI sequence on the Bruker scanner (Bruker, Billerica, MA, USA) was modified for ^{13}C applications and for use with spsp pulses, by enabling multiple image acquisitions pertaining to different chemical shifts, with variable flip angle implementation. Dynamic images were acquired over a minute with 18 metabolite images for each chemical shift in the following sequence, urea, pyruvate, and lactate, every 3 or 4 s. A reference scan was used to correct for the EPI phase errors that lead to Nyquist ghosts. This also enabled the online reconstruction of ^{13}C metabolite maps. The spsp RF pulse used in all of the EPI acquisitions was designed to individually excite [1-^{13}C]pyruvate, [1-^{13}C]lactate, or ^{13}C Urea at 3T, with a passband FWHM of 120 Hz and a stopband of 600 Hz (**Figure 3.1**). The spectral spatial pulse was 25.17 ms long and designed with a default slice thickness of 15 mm and is the same pulse used in the clinical studies [7]. The RF pulse was designed in MATLAB (MathWorks, Natick, MA, USA) using the spsp RF pulse design toolbox [20]. Further information and access by request to the pulse sequence can be found through https://github.com/UCSF-HMTRC/ accessed on 20 March 2023.

3.3.3 Experiments

All experiments were performed on a preclinical 3T cryogen-free Bruker Biospin (Billerica, MA, USA) with a maximum gradient strength of 960 mT/m and a maximum slew rate of 3550 T/m/s. A dual-tuned 40 mm $^{1}H/^{13}C$ volume coil was used for both the thermal phantom and hyperpolarized ^{13}C experiments. A total of 24 mg of [1-^{13}C]pyruvate was polarized on Hypersense (Oxford Instruments, Oxford, England). Thermal phantoms consisted of a ~2 cm

diameter sphere filled with 4M ^{13}C-Urea doped with 25mM Magnevist. A 5 mm diameter and 4 cm long cylindrical tube filled with 4M ^{13}C urea was used with mice during in vivo testing for calibration.

Eight mice implanted with patient-derived xenograft tissues of either renal cell carcinoma (RCC), or prostate cancer (LTL610, LuCap93) in the kidney or liver were used for testing the sequences (RCC kidney: 3, LTL liver: 2, LTL kidney: 2, LuCap93 kidney: 1) [21–24]. Animal experiments were performed under protocols approved by the Institutional Animal Care and Use Committee. Mice were anesthetized during the MRI experiments and their tail veins were cannulated for infusion of hyperpolarized solutions. Then, 350 μL of hyperpolarized neutralized 80 mM [1-^{13}C]pyruvate was infused in 12–15 s. Imaging was started 10 s after the start of the infusion. The average time between hyperpolarized imaging experiments was 41 min. For the 8 studies where both spspEPI and CSI imaging were acquired, CSI was acquired before spspEPI for 6 of them.

Different flip-angle combinations were tested for the metabolite-specific EPI sequence: 10° for urea, 10°, 15°, or 20° for pyruvate and 20°, 30°, or 50° for lactate. The field-of-view acquired was either 3.2 cm × 3.2 cm or 6.4 cm × 6.4 cm and corresponding spatial resolutions of 2 mm × 2 mm or 4 mm × 4 mm. Temporal resolutions tested were 3 or 4 s, adjusted by adding delay time after acquisition of metabolites (**Figure 3.1D**). Corresponding CSI scans were acquired with flip angle 10°, resolution 4 mm × 4 mm with FOV of 3.2 cm × 3.2 cm, centric phase encode ordering, and temporal resolution of 4.25 s. CSI flip angle was chosen due to previous success

using flip angle. Multi-slice ^{1}H T_2 RARE images were acquired with a 3.2 cm × 3.2 cm FOV and 0.167 mm × 0.167 mm resolution for anatomical reference.

3.3.4 Analysis

CSI metabolite maps were generated using SIVIC [25]. Tumor regions-of-interest (ROIs) were drawn on T_2 RARE images and down-sampled to the EPI and CSI resolutions. Hyperpolarized signal time courses were normalized by the mean noise over time within a region outside of the animal. An inputless one-physical-compartment pharmacokinetic model accounting for RF pulse flip angles was used to fit k_{PL} to the average signal from all tumor voxels resulting in a single k_{PL} value and per voxel within the tumor resulting in a k_{PL} map [18,26]. Hyperpolarized images and k_{PL} maps were overlaid on T_2 RARE after resampling to the T_2 RARE resolution and applying a Fermi filter. Simulations, models, and analysis were performed using MATLAB (Mathworks, MA, USA).

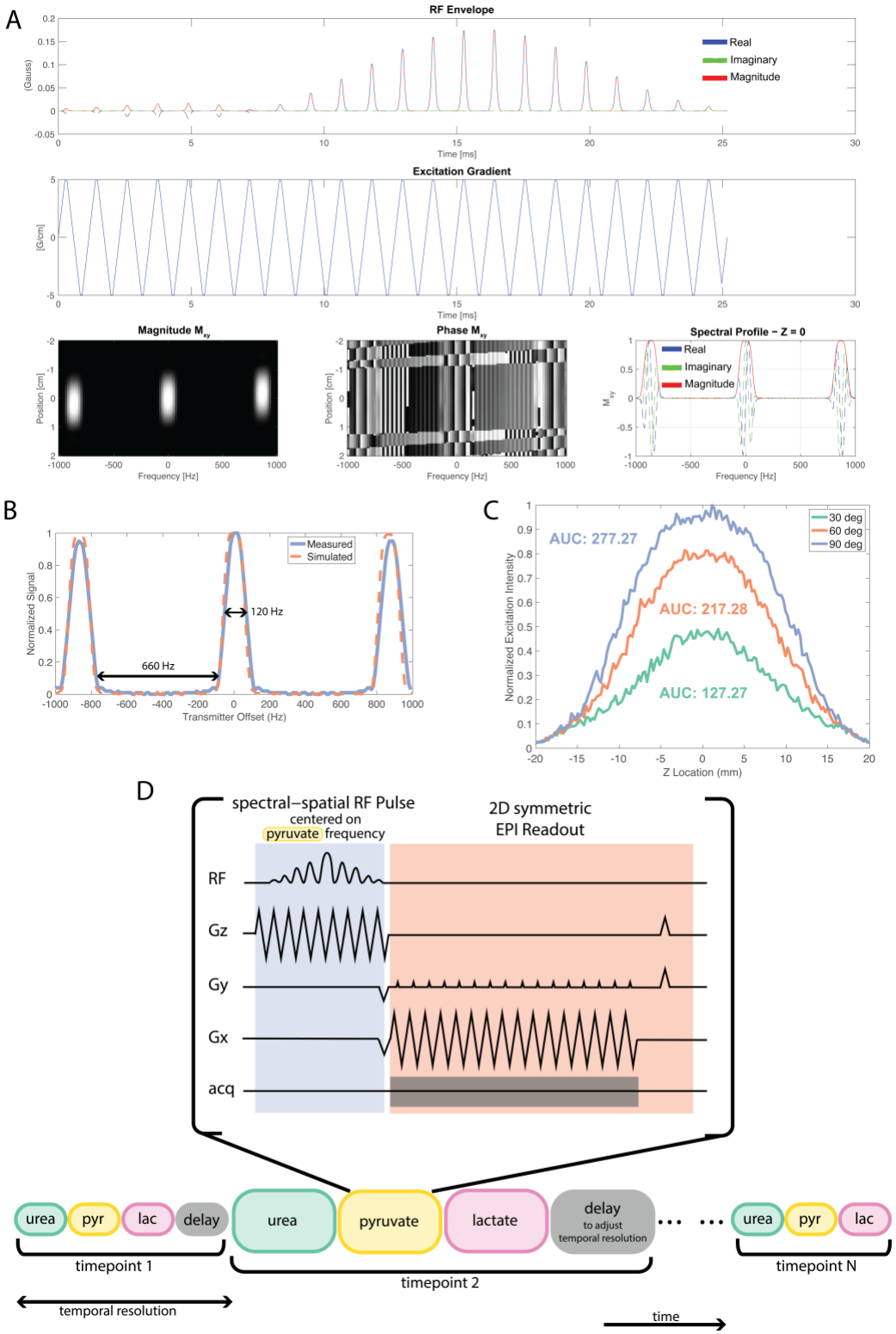

Figure 3.1: EPI spectral-spatial RF pulse design. (A) RF pulse design using the SPSP RF pulse design toolbox [20]. (B) SPSP RF pulse frequency selectivity measurements were performed with a 4M ^{13}C Urea sphere phantom. For this pulse, the measured passband had a FWHM of 120 Hz and stopband of 660 Hz. (C) Slice profile and (Figure caption continued on the next page.)

(Figure caption continued from the previous page.) corresponding area-under-the-curve (AUC) values for 30°, 60°, and 90° excitations. Corresponding FWHM values are 16.77 mm, 18.68 mm, and 20.10 mm, respectively. (D) During one timepoint, each metabolite is acquired using a spsp RF pulse with an EPI readout. Delay time is added at the end of a timepoint to achieve preferred temporal resolution.

3.4 Results

3.4.1 Spectral–Spatial Pulse Design and Calibration

The spectral–spatial RF pulse design and pulse profile measurements are shown in **Figure 3.1**. There is excellent agreement between the simulated and measured frequency profile of the pulse, confirming the 120 Hz FWHM passband and a stopband of over 600 Hz. The spsp pulse power was calibrated on a 4M ^{13}C-urea sphere phantom by using a one-dimensional slab acquisition and stepping through the power for a 23.5 ms pulse length and determining the 90° flip angle that corresponds to the maximal signal (when covering a full 180 nutation). Additionally, the varying RF flip angle and subsequent slice profile of the pulse was tested in the spspEPI sequence using a long 4M Urea phantom as demonstrated in **Figure 3.1C**. The FWHM of the slice profile for 30°, 60°, and 90° excitations were 16.77 mm, 18.68 mm, and 20.10 mm, respectively. The AUC values were 127.27, 217.28, and 277.27, respectively.

3.4.2 Comparison of EPI and CSI

A 2D PSF was simulated for both CSI and EPI acquisitions (**Figure 3.2**). The simulated EPI PSF was effectively a delta function with no signal blurring across voxels whereas the simulated CSI PSF resulted in signal blurring for both pyruvate and lactate due to varying signal amplitudes across phase encoding steps. From the CSI PSF profile with a 10 degree flip angle, the FWHM was 5.603 mm and 5.209 mm for pyruvate and lactate, respectively, which is broader than the nominal resolution of 4 mm. The width at 10% of max signal was 13.827 mm and 20.410 mm

for pyruvate and lactate. In comparison, for the EPI PSF profile, the FWHM and width at 10% of max signal was 2.415 mm and 10.809 mm for both pyruvate and lactate. For in vivo experiments, the simulations indicate that CSI will have a higher likelihood of signal bleeding, for example between the vasculature to kidney tumors, compared to EPI. This would typically result in lower k_{PL} estimates for voxels adjacent to large vessels because of the additional vascular pyruvate signal bleed into nearby regions.

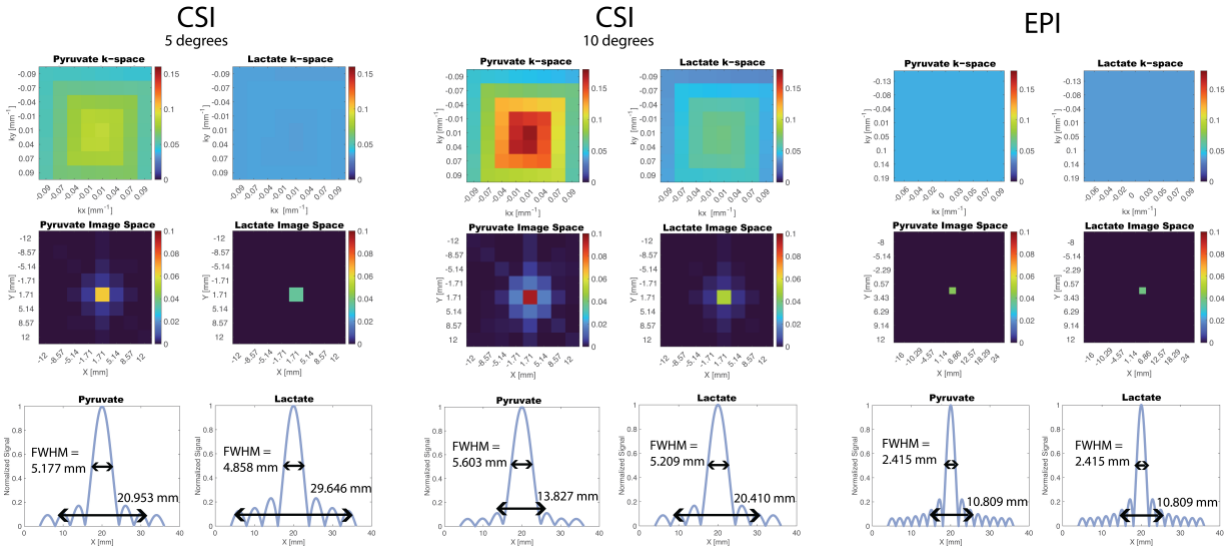

Figure 3.2: Simulation of the point spread function (PSF) for CSI and EPI Acquisition. Magnetization decay was modelled across k-space using a pharmacokinetic model. The CSI PSFs for two different flip angles are shown: 5 degrees and 10 degrees.

Pyruvate and lactate AUC images of CSI and EPI scans overlaid on proton T_2 images of the same mouse were compared side by side (**Figure 3.3**). CSI maps showed a strong metabolic signal from the vasculature but did not show any signal from the tumor region that was clearly differentiable from the vasculature signal. Meanwhile, the EPI maps showed metabolite signals that were better delineated and clearly originating from the tumor as well as the vasculature. Line plot profiles of the lactate signal show two distinct peaks for EPI compared to a single peak for

CSI. This agrees with the PSF results from the simulation and suggests the tumor signal for the CSI maps is obscured by the blurred vasculature signal.

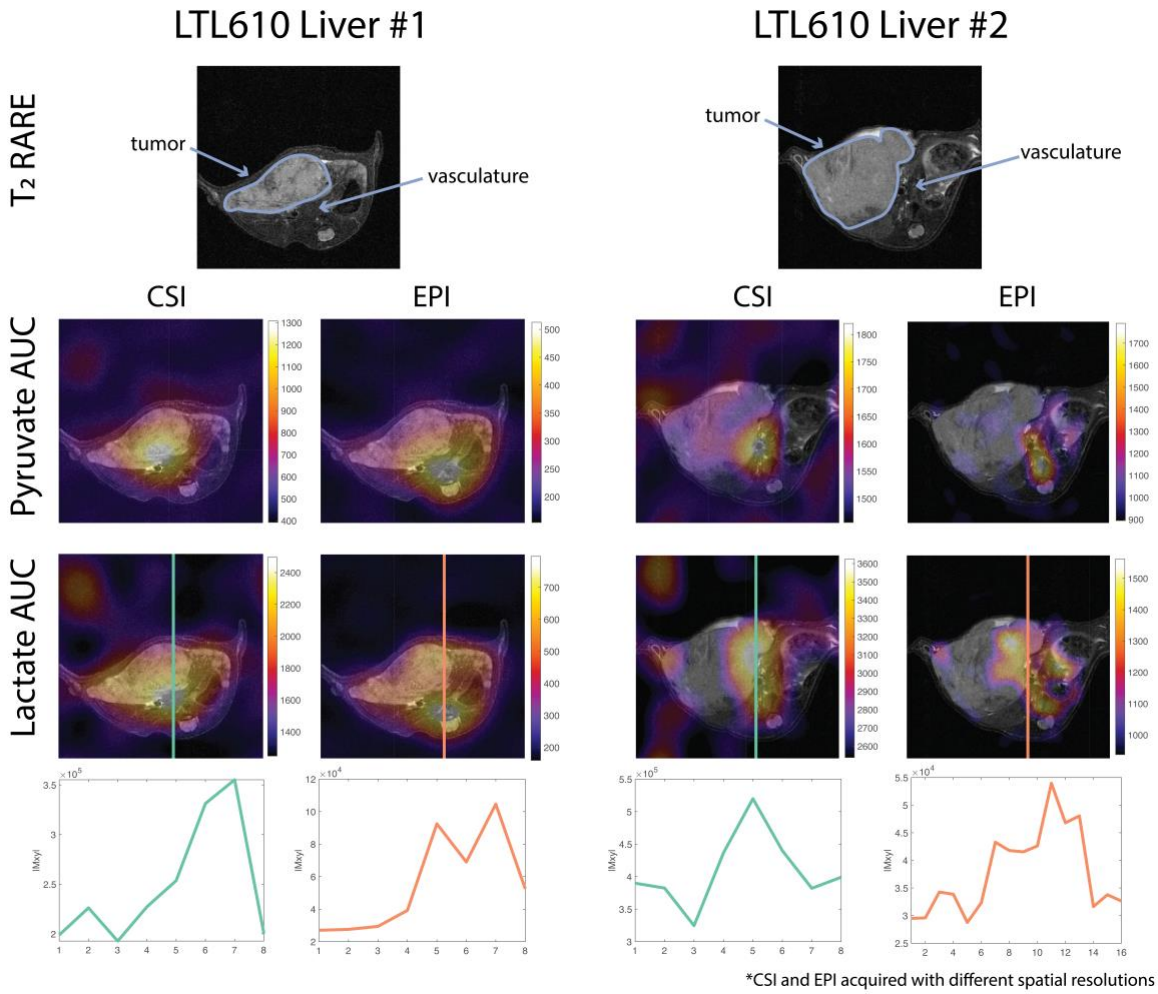

Figure 3.3: In vivo pyruvate and lactate area-under-the-curve (AUC) maps of two mice overlaid on T_2 RARE images. Both examples are of an LTL610 tumor implanted in the mouse liver. The bottom row shows line profiles drawn through the lactate AUC. For both examples, CSI was acquired before EPI.

3.4.3 Testing In Vivo EPI Parameters Optimization for Robust SNR and k_{PL}

Relative pyruvate and lactate SNR was calculated for various pyruvate–lactate flip angle pairs and temporal resolutions that can be used in a metabolite-specific EPI experiments (**Figure 3.4**). Pyruvate SNR was only dependent on the flip angle of pyruvate and not lactate, as expected.

Pyruvate SNR was the highest for pyruvate flip angles of 30 to 45 degrees. The highest lactate SNR resulted when using lower pyruvate flip angles (less than 15 degrees) and lactate flip angles between 25 and 40 degrees. For pyruvate–lactate flip angle pairs, the standard deviation of k_{PL} fitting error was also calculated. For a temporal resolution of 2 s, k_{PL} fitting error variation was the lowest for pyruvate flip angles of 15–20 degrees and lactate flip angles of 30 to 50 degrees. For a temporal resolution of 3 s, k_{PL} fitting error variation was minimized for pyruvate flip angles of 15–25 degrees and lactate flip angles of 30–60 degrees. For a temporal resolution of 5 s, k_{PL} fitting error variation was minimized for pyruvate flip angles of 20–35 degrees and lactate flip angles of 40–60 degrees.

A simulated EPI acquisition, with a shorter temporal resolution of 2 s, resulted in a relative increase in pyruvate SNR. In contrast, lactate SNR peaked with a temporal resolution of 3 s. A longer temporal resolution decreased the k_{PL} fitting error for a mid-range of flip angles. According to the simulation, a pyruvate flip angle between 10° to 20°, a lactate flip angle of 25° to 40°, and a temporal resolution of 3 s will optimize lactate SNR without compromising pyruvate SNR and maintain a low k_{PL} fitting error.

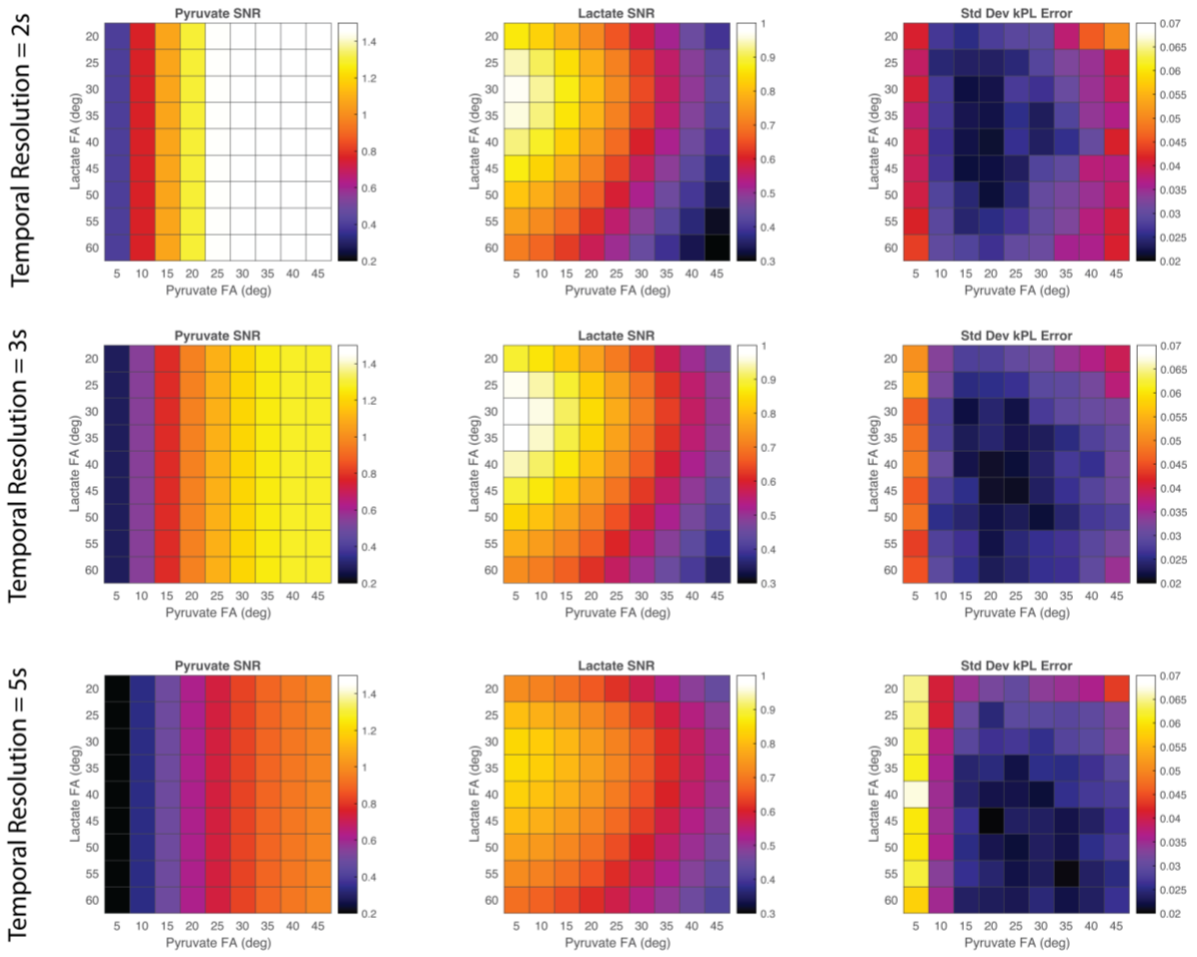

Figure 3.4: Pyruvate and lactate SNR and k_{PL} fitting error of simulated EPI signal for various temporal resolutions and pyruvate and lactate flip angles (FAs).The simulation used the following parameters: k_{PL} = 0.05 1/s, $T_{1,pyruvate}$ = 20 s, and $T_{1,lactate}$ = 30 s.

The results of the simulation (**Figure 3.4**) were used to guide EPI parameter choices. A pyruvate flip angle of 15° and a lactate flip angle of 30° were chosen as the simulation suggested high lactate SNR and low k_{PL} error. A smaller pyruvate flip angle was not used as previous experiments found shorter pyruvate flip angles did not provide sufficient signal. Larger flip angles of 20° and 50° for pyruvate and lactate were chosen for comparison. A temporal resolution of 3 s was chosen as lactate SNR was the highest and a 4 s temporal resolution was

used for comparison. The feasibility of these chosen parameters was evaluated with in vivo experiments.

Average pyruvate and lactate time courses within tumor and blood vessel ROIs for EPI scans with varying parameters were plotted (**Figure 3.5**). Using a temporal resolution of 3 s resulted in higher relative SNR and area-under-the-curve (AUC) for pyruvate and lactate compared with a temporal resolution of 4 s. A coarser spatial resolution of 4 mm × 4 mm also resulted in a higher AUC for pyruvate and lactate compared with a finer spatial resolution of 2 mm × 2 mm. Additionally, a coarser spatial resolution paired with an optimized flip angle choice of 15° for pyruvate and 30° for lactate increased the AUC for pyruvate and lactate in the tumor compared with the finer spatial resolution and flip angles of 20° and 50° for pyruvate and lactate. These experiments showed that changing spatial resolution from 2 mm to 4 mm and temporal resolution from 4 s to 3 s improved pyruvate and lactate SNR. Nevertheless, it is important to consider that these comparisons were conducted with a very limited sample size and some of the data have limited SNR (**Figure 3.5**, center top) which interfere with drawing strong conclusions. Instead, these results support previously shown simulations (**Figure 3.4**).

Voxel-wise k_{PL} maps were calculated for CSI and EPI data in implanted tumors (**Figure 3.6**). In one mouse, the k_{PL} values within the liver tumor were very similar between CSI and EPI sequences, and ranged from 0.08–0.11 1/s. In another mouse, EPI k_{PL} values were consistent between two consecutive days for the same liver tumor with average tumor k_{PL} of 0.029 1/s and 0.028 1/s. The three mice with the same type of implanted RCC tumors also demonstrated

relatively similar k_{PL} values of 0.02–0.035 1/s across the tumors, with some differences in heterogeneity between the animals. All k_{PL} values were similar to the previous literature [27].

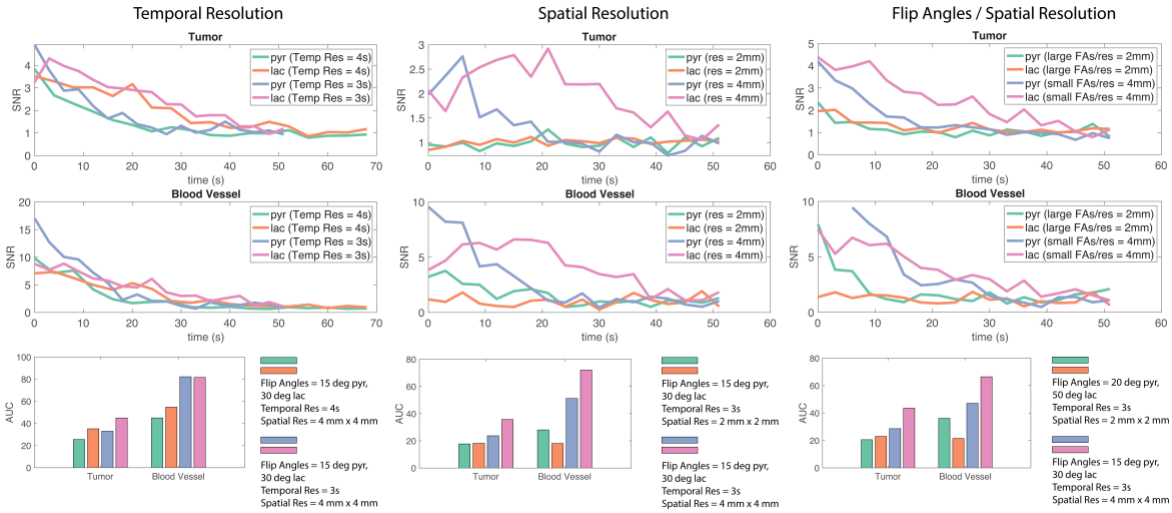

Figure 3.5: SNR over time and area-under-the-curve (AUC) values for various in vivo mice experiments. Tumor model and location from left to right: LuCap93 kidney; LTL kidney; and LTL kidney.

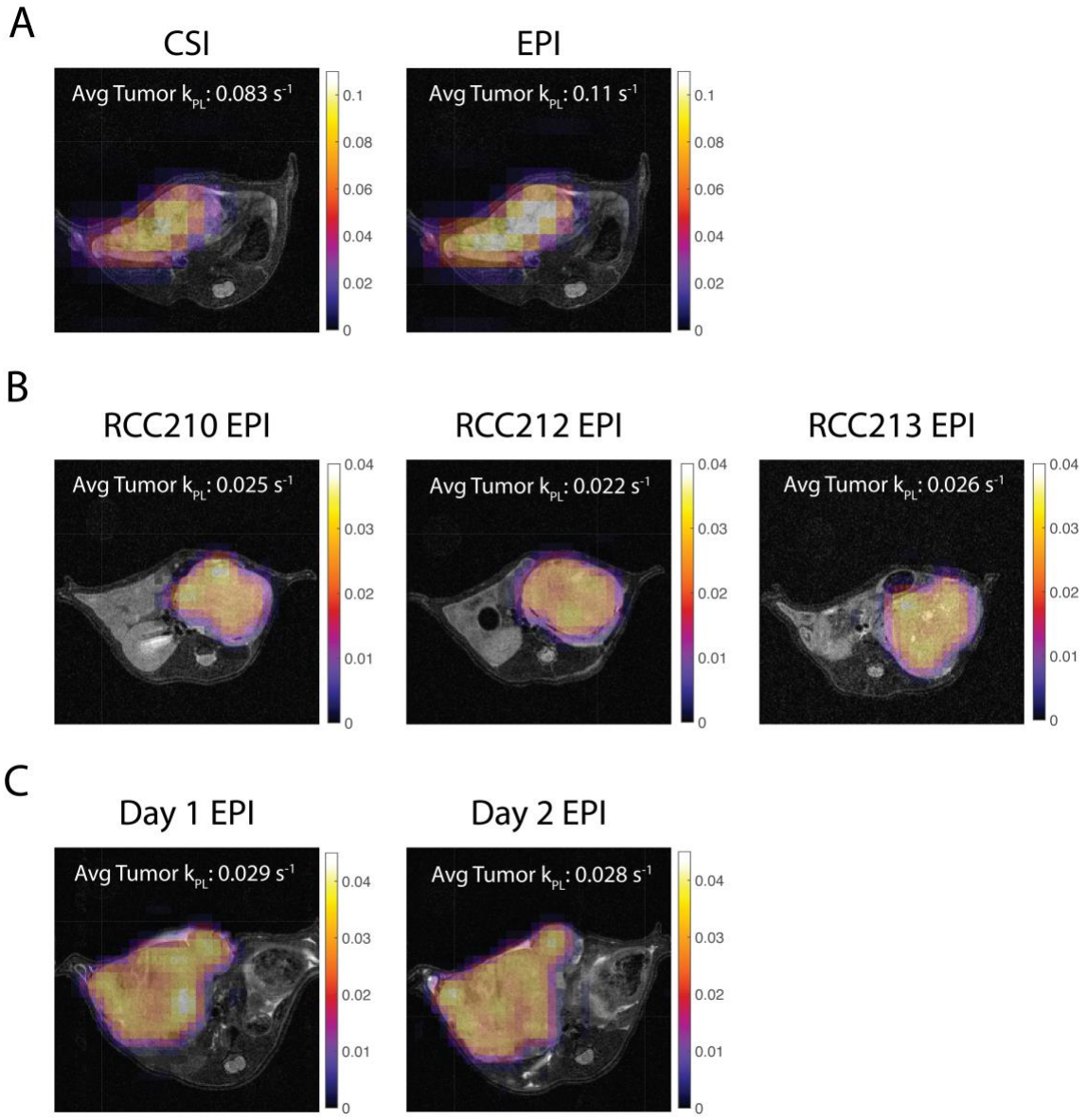

Figure 3.6: Pharmacokinetic model fits of k_{PL} for in vivo mice overlaid on ^{1}H T2 RARE images. (A) CSI vs EPI k_{PL} maps are compared for the same mouse with an LTL liver tumor. (B) EPI k_{PL} maps are compared for three different mice with RCC tumors. (C) EPI k_{PL} maps are compared for the same mouse with an LTL liver tumor imaged on two consecutive days.

3.5 Discussion

We have successfully implemented and optimized a preclinical two-dimensional (2D) spsp EPI sequence to better match the state-of-the-art clinical hyperpolarized ^{13}C metabolic imaging

studies. These are being performed as part of a co-clinical trial of metastatic prostate cancer patients prior to and after chemotherapy which is a project funded under the Co-Clinical Imaging Research Program (U24CA253377).

3.5.1 Spectral–Spatial Pulse

We have presented testing procedures and results of RF power calibration and spatial selectivity that can be unique to the vendor implementation of the spsp pulse and its implementation in a sequence. Both parameters are critical for the spsp pulse performance.

3.5.2 CSI vs. spspEPI

A metabolite-specific EPI sequence with a spectral–spatial pulse can improve flexibility and innovation in preclinical hyperpolarized ^{13}C studies. In this work, we demonstrate how a preclinical spspEPI pipeline may work as well as highlighting some of the advantages in comparison to CSI methods.

An advantage of a spspEPI sequence is its speed which can allow for shorter temporal resolutions for multi-metabolite studies, multi-slice, or even 3D acquisitions without losing spatial resolution. In addition, using a spspEPI acquisition may make translation of preclinical studies to the clinic straightforward in terms of expectation of signal observation, dynamics, and kinetic rates.

SpspEPI sequences also allow for flexibility in acquisition trajectories and flip angles. With a spsp pulse, the flip angle of an individual metabolite can be adjusted allowing for manipulation

of the signal to improve the SNR of downstream metabolites [28]. The EPI trajectory supports variable spatial resolutions for an individual metabolite which can also be used to manipulate the signal to improve SNR[29].

Another consideration is signal blurring in CSI due to T_1 decay and metabolic conversion experienced between signals acquired across phase encodings. This may be minimized with center-out k-space trajectories, but still leads to a broadening of the PSF especially compared to EPI. This was confirmed in this work with a simulation (**Figure 3.2**) and in vivo data (**Figure 3.3**). This blurring is particularly impactful when imaging small animals where the vasculature is anatomically close to regions or organs of interest. The higher vasculature signal may bleed into the signal from other organs making them difficult to differentiate and more difficult to quantify the metabolism. In our experience, a spspEPI acquisition allowed for better localization of signal in small animals.

3.5.3 Optimization of EPI Parameters

A spspEPI acquisition allows for more flexibility which in turn specifies more parameter choices. In this work, three parameters were optimized through simulations and confirmed with in vivo experiments. With a fast EPI readout, there is flexibility in the choice of temporal resolution dependent on the delay between time point acquisitions. Simulations demonstrated shorter temporal resolutions resulted in higher pyruvate SNR as expected since more of the hyperpolarized signal is captured before T_1 decay. In contrast, lactate SNR peaks at a temporal resolution of 3 s as there is more time for metabolic conversion from pyruvate to lactate (**Figure 3.4**).

A metabolite-specific flip angle scheme can be used to adjust SNR for downstream metabolites in spsp acquisitions. For example, pyruvate flip angle is a trade-off between pyruvate and lactate SNR. Higher pyruvate flip angles result in more pyruvate signal, but the RF uses up more of the limited hyperpolarized signal and there is limited lactate signal. A smaller pyruvate flip angle scheme will result in higher lactate SNR (**Figures 3.4** and **3.5**).

Spatial resolution can also be adjusted easily with a fast readout such as EPI. A finer resolution, although more advantageous for anatomical specificity, can result in lower SNR, although this is dependent on the metabolism within the animal, tumor, or organ imaged. Considerations for a coarser resolution may be appropriate for anatomy with lower perfusion, such as bone, and when vasculature is further from the ROI.

Other parameters may also need to be considered for spspEPI studies that were not explored in this work. For example, the imaging delay after start of injection was kept constant at 10 s. Shorter delays may capture more of the metabolic signal and lead to better quantification and pharmacokinetic model fitting.

3.5.4 Pharmacokinetic Modelling and Quantification

One method of quantification for hyperpolarized ^{13}C-Pyruvate imaging is to use a pharmacokinetic model to fit for the apparent rate constant, k_{PL}. This biomarker holds promise to be comparable across different acquisition methods and timings. In this study, the generality of k_{PL} was demonstrated as it remained consistent across different acquisitions (CSI vs. EPI), different days of acquisition, and different mice for the same tumor type (**Figure 3.6**). The values

were also consistent to previous studies using the same pharmacokinetic model for in vivo RCC tumors [27].

3.6 Conclusions

In this study, a 2D metabolite-specific EPI sequence was developed, calibrated, and tested for use on a preclinical Bruker system. A spectral–spatial pulse for hyperpolarized [1-^{13}C]pyruvate was tested and implemented for acquisition. PSF simulations and in vivo data suggest this developed spspEPI sequence may be more favorable for preclinical studies in comparison to CSI sequences, due to minimized blurring from signal loss across phase encoding. The spspEPI sequence parameters (flip angles, temporal, and spatial resolution) were optimized to improve SNR and rate constant fitting precision using simulations and found to provide good results with in vivo experiments. Pyruvate to lactate rate constant, k_{PL}, fitting using a pharmacokinetic model revealed comparable values across sequences, days, mice with similar tumors, and the previous literature [27].

3.7 References

1. Nelson, S.; Kurhanewicz, J.; Vigneron, D.; Larson, P.; Harzstark, A.; Ferrone, M.; Van Criekinge, M.; Chang, J.; Bok, R.; Park, I.; et al. Metabolic Imaging of Patients with Prostate Cancer Using Hyperpolarized [1-13C]Pyruvate. *Sci. Transl. Med.* **2013**, *5*, 198ra108. https://doi.org/10.1126/scitranslmed.3006070.
2. Miloushev, V.Z.; Granlund, K.L.; Boltyanskiy, R.; Lyashchenko, S.K.; DeAngelis, L.M.; Mellinghoff, I.K.; Brennan, C.W.; Tabar, V.; Yang, T.J.; Holodny, A.I.; et al. Metabolic Imaging of the Human Brain with Hyperpolarized 13C Pyruvate Demonstrates 13C Lactate Production in Brain Tumor Patients. *Cancer Res.* **2018**, *78*, 3755–3760. https://doi.org/10.1158/0008-5472.CAN-18-0221.
3. Gallagher, F.A.; Woitek, R.; McLean, M.A.; Gill, A.B.; Manzano Garcia, R.; Provenzano, E.; Riemer, F.; Kaggie, J.; Chhabra, A.; Ursprung, S.; et al. Imaging Breast Cancer Using Hyperpolarized Carbon-13 MRI. *Proc. Natl. Acad. Sci. USA* **2020**, *117*, 2092–2098. https://doi.org/10.1073/pnas.1913841117.
4. Tang, S.; Meng, M.V.; Slater, J.B.; Gordon, J.W.; Vigneron, D.B.; Stohr, B.A.; Larson, P.E.Z.; Wang, Z.J. Metabolic Imaging with Hyperpolarized 13C Pyruvate Magnetic Resonance Imaging in Patients with Renal Tumors—Initial Experience. *Cancer* **2021**, *127*, 2693–2704. https://doi.org/10.1002/cncr.33554.
5. Rider, O.J.; Apps, A.; Miller, J.J.J.J.; Lau, J.Y.C.; Lewis, A.J.M.; Peterzan, M.A.; Dodd, M.S.; Lau, A.Z.; Trumper, C.; Gallagher, F.A.; et al. Noninvasive In Vivo Assessment of Cardiac Metabolism in the Healthy and Diabetic Human Heart Using Hyperpolarized 13C MRI. *Circ. Res.* **2020**, *126*, 725–736. https://doi.org/10.1161/CIRCRESAHA.119.316260.

6. Wang, Z.J.; Ohliger, M.A.; Larson, P.E.Z.; Gordon, J.W.; Bok, R.A.; Slater, J.; Villanueva-Meyer, J.E.; Hess, C.P.; Kurhanewicz, J.; Vigneron, D.B. Hyperpolarized 13C MRI: State of the Art and Future Directions. *Radiology* **2019**, *291*, 273–284. https://doi.org/10.1148/radiol.2019182391.
7. Gordon, J.W.; Chen, H.; Autry, A.; Park, I.; Van Criekinge, M.; Mammoli, D.; Milshteyn, E.; Bok, R.; Xu, D.; Li, Y.; et al. Translation of Carbon-13 EPI for Hyperpolarized MR Molecular Imaging of Prostate and Brain Cancer Patients. *Magn. Reson. Med.* **2018**, *81*, 2702–2709. https://doi.org/10.1002/mrm.27549.
8. Gordon, J.W.; Chen, H.-Y.; Dwork, N.; Tang, S.; Larson, P.E.Z. Fast Imaging for Hyperpolarized MR Metabolic Imaging. *J. Magn. Reson. Imaging* **2021**, *53*, 686–702. https://doi.org/10.1002/jmri.27070.
9. Cunningham, C.H.; Chen, A.P.; Lustig, M.; Hargreaves, B.A.; Lupo, J.; Xu, D.; Kurhanewicz, J.; Hurd, R.E.; Pauly, J.M.; Nelson, S.J.; et al. Pulse Sequence for Dynamic Volumetric Imaging of Hyperpolarized Metabolic Products. *J. Magn. Reson.* **2008**, *193*, 139–146. https://doi.org/10.1016/j.jmr.2008.03.012.
10. Shang, H.; Sukumar, S.; von Morze, C.; Bok, R.A.; Marco-Rius, I.; Kerr, A.; Reed, G.D.; Milshteyn, E.; Ohliger, M.A.; Kurhanewicz, J.; et al. Spectrally Selective 3D Dynamic Balanced SSFP for Hyperpolarized C-13 Metabolic Imaging with Spectrally Selective RF Pulses. *Magn. Reson. Med.* **2017**, *78*, 963–975. https://doi.org/10.1002/mrm.26480.
11. Milshteyn, E.; von Morze, C.; Gordon, J.W.; Zhu, Z.; Larson, P.E.Z.; Vigneron, D.B. High Spatiotemporal Resolution BSSFP Imaging of Hyperpolarized [1-13C]Pyruvate and [1-13C]Lactate with Spectral Suppression of Alanine and Pyruvate-Hydrate. *Magn. Reson. Med.* **2018**, *80*, 1048–1060. https://doi.org/10.1002/mrm.27104.

12. Lee, P.M.; Chen, H.-Y.; Gordon, J.W.; Wang, Z.J.; Bok, R.; Hashoian, R.; Kim, Y.; Liu, X.; Nickles, T.; Cheung, K.; et al. Whole-Abdomen Metabolic Imaging of Healthy Volunteers Using Hyperpolarized [1-13C]Pyruvate MRI. *J. Magn. Reson. Imaging* **2022**, *56*, 1792–1806. https://doi.org/10.1002/jmri.28196.
13. Walker, C.M.; Fuentes, D.; Larson, P.E.Z.; Kundra, V.; Vigneron, D.B.; Bankson, J.A. Effects of Excitation Angle Strategy on Quantitative Analysis of Hyperpolarized Pyruvate. *Magn. Reson. Med.* **2019**, *81*, 3754–3762. https://doi.org/10.1002/mrm.27687.
14. Tang, S.; Milshteyn, E.; Reed, G.; Gordon, J.; Bok, R.; Zhu, X.; Zhu, Z.; Vigneron, D.B.; Larson, P.E.Z. A Regional Bolus Tracking and Real-Time B1 Calibration Method for Hyperpolarized 13C MRI. *Magn. Reson. Med.* **2019**, *81*, 839–851. https://doi.org/10.1002/mrm.27391.
15. Yen, Y.-F.; Kohler, S.J.; Chen, A.P.; Tropp, J.; Bok, R.; Wolber, J.; Albers, M.J.; Gram, K.A.; Zierhut, M.L.; Park, I.; et al. Imaging Considerations for in Vivo 13C Metabolic Mapping Using Hyperpolarized 13C-Pyruvate. *Magn. Reson. Med.* **2009**, *62*, 1–10. https://doi.org/10.1002/mrm.21987.
16. Michel, K.A.; Ragavan, M.; Walker, C.M.; Merritt, M.E.; Lai, S.Y.; Bankson, J.A. Comparison of Selective Excitation and Multi-Echo Chemical Shift Encoding for Imaging of Hyperpolarized [1-13C]Pyruvate. *J. Magn. Reson.* **2021**, *325*, 106927. https://doi.org/10.1016/j.jmr.2021.106927.
17. Blazey, T.; Reed, G.D.; Garbow, J.R.; von Morze, C. Metabolite-Specific Echo-Planar Imaging of Hyperpolarized [1-13C]Pyruvate at 4.7 T. *Tomography* **2021**, *7*, 466–476. https://doi.org/10.3390/tomography7030040.

18. Larson, P.E.Z.; Chen, H.Y.; Gordon, J.W.; Korn, N.; Maidens, J.; Arcak, M.; Tang, S.; Criekinge, M.; Carvajal, L.; Mammoli, D.; et al. Investigation of Analysis Methods for Hyperpolarized 13C-Pyruvate Metabolic MRI in Prostate Cancer Patients. *NMR Biomed.* **2018**, *31*, e3997. https://doi.org/10.1002/nbm.3997.
19. Qin, Q. Point Spread Functions of the T2 Decay in K-Space Trajectories with Long Echo Train. *Magn. Reson. Imaging* **2012**, *30*, 1134–1142. https://doi.org/10.1016/j.mri.2012.04.017.
20. Hyperpolarized-MRI-Toolbox. Available online https://github.com/LarsonLab/hyperpolarized-mri-toolbox (accessed on 20 March 2023).
21. Agarwal, S.; Bok, R.; Peehl, D.; Sriram, R. *Protocol: Intrahepatic Implantation of Tumor Cells*; University of California, San Francisco, CA, USA, 2021. https://doi.org/10.17504/protocols.io.bvrtn56n.
22. Agarwal, S.; Peehl, D.; Sriram, R. *Protocol: Intratibial Implantation of Tumor Cells*; University of California, San Francisco, CA, USA, 2021. https://doi.org/10.17504/protocols.io.bvrsn56e.
23. Agarwal, S.; Peehl, D.; Sriram, R. *Protocol: Single Cell Digestion of Tumor Tissue*; University of California, San Francisco, CA, USA, 2021. https://doi.org/10.17504/protocols.io.bvrun56w.
24. Agudelo, J.P.; Upadhyay, D.; Zhang, D.; Zhao, H.; Nolley, R.; Sun, J.; Agarwal, S.; Bok, R.A.; Vigneron, D.B.; Brooks, J.D.; et al. Multiparametric Magnetic Resonance Imaging and Metabolic Characterization of Patient-Derived Xenograft Models of Clear Cell Renal Cell Carcinoma. *Metabolites* **2022**, *12*, 1117. https://doi.org/10.3390/metabo12111117.

25. Crane, J.C.; Gordon, J.W.; Chen, H.-Y.; Autry, A.W.; Li, Y.; Olson, M.P.; Kurhanewicz, J.; Vigneron, D.B.; Larson, P.E.Z.; Xu, D. Hyperpolarized 13C MRI Data Acquisition and Analysis in Prostate and Brain at University of California, San Francisco. *NMR Biomed.* **2021**, *34*, e4280. https://doi.org/10.1002/nbm.4280.
26. Khegai, O.; Schulte, R.F.; Janich, M.A.; Menzel, M.I.; Farrell, E.; Otto, A.M.; Ardenkjaer-Larsen, J.H.; Glaser, S.J.; Haase, A.; Schwaiger, M.; et al. Apparent Rate Constant Mapping Using Hyperpolarized [1–13C]Pyruvate. *NMR Biomed.* **2014**, *27*, 1256–1265. https://doi.org/10.1002/nbm.3174.
27. Ahamed, F.; Van Criekinge, M.; Wang, Z.J.; Kurhanewicz, J.; Larson, P.; Sriram, R. Modeling Hyperpolarized Lactate Signal Dynamics in Cells, Patient-derived Tissue Slice Cultures and Murine Models. *NMR Biomed.* **2021**, *34*, e4467. https://doi.org/10.1002/nbm.4467.
28. Larson, P.E.Z.; Kerr, A.B.; Chen, A.P.; Lustig, M.S.; Zierhut, M.L.; Hu, S.; Cunningham, C.H.; Pauly, J.M.; Kurhanewicz, J.; Vigneron, D.B. Multiband Excitation Pulses for Hyperpolarized 13C Dynamic Chemical-Shift Imaging. *J. Magn. Reson.* **2008**, *194*, 121–127. https://doi.org/10.1016/j.jmr.2008.06.010.
29. Gordon, J.W.; Autry, A.W.; Tang, S.; Graham, J.Y.; Bok, R.A.; Zhu, X.; Villanueva-Meyer, J.E.; Li, Y.; Ohilger, M.A.; Abraham, M.R.; et al. A Variable Resolution Approach for Improved Acquisition of Hyperpolarized 13 C Metabolic MRI. *Magn. Reson. Med.* **2020**, *84*, 2943–2952. https://doi.org/10.1002/mrm.2842

CHAPTER 4: A PHARMACOKINETIC MODEL FOR HYPERPOLARIZED 13C-PYRUVATE MRI WHEN USING METABOLITE-SPECIFIC BSSFP SEQUENCES

4.1 Abstract

Metabolite-Specific bSSFP (MS-bSSFP) sequences are increasingly used in Hyperpolarized [1-^{13}C]Pyruvate (HP ^{13}C) MRI studies as they improve SNR by refocusing the magnetization each TR. Currently, pharmacokinetic models used to fit conversion rate constants, k_{PL} and k_{PB}, and rate constant maps do not account for differences in the signal evolution of MS-bSSFP acquisitions.

In this work, a flexible MS-bSSFP model was built that can be used to fit conversion rate constants for these experiments. The model was validated in vivo using paired animal (healthy rat kidneys n=8, transgenic adenocarcinoma of the mouse prostate n=3) and human renal cell carcinoma (n=3) datasets. GRE acquisitions were used with a previous GRE model to compare to the results of the proposed GRE-bSSFP model.

Within simulations, the proposed GRE-bSSFP model fits the simulated data well whereas a GRE model shows bias due to model mismatch. For the in vivo datasets, the estimated conversion rate constants using the proposed GRE-bSSFP model are consistent with a previous GRE model. Jointly fitting the lactate T_2 with k_{PL} resulted in less precise k_{PL} estimates.

The proposed GRE-bSSFP model provides a method to estimate conversion rate constants, k_{PL} and k_{PB}, for MS-bSSFP HP ^{13}C experiments. This model may also be modified and used for other applications, e.g., estimating rate constants with other hyperpolarized reagents or multi-echo bSSFP.

4.2 Introduction

Hyperpolarized [1-^{13}C]Pyruvate (HP ^{13}C) MRI is a powerful method of spatially measuring metabolic activity within healthy, inflamed, stressed, cancerous, or diseased tissue in vivo[1–3]. For cancer, HP ^{13}C MRI is particularly advantageous as it can provide in vivo measurements of the Warburg effect. This effect states that aggressive, growing tumors rely more readily on aerobic glycolysis rather than oxidative phosphorylation, resulting in increased lactate production[4,5].

With HP ^{13}C studies, we can probe the glycolysis and oxidative phosphorylation pathways as we capture ^{13}C-pyruvate and its' products, ^{13}C-lactate and ^{13}C-bicarbonate, dynamically within a few minutes[1,2]. To assess tumor aggressiveness we are interested in the rate of lactate production from pyruvate[3]. The rate of bicarbonate production from pyruvate serves as a surrogate marker for oxidative phosphorylation[1,6] and is valuable for identifying dysfunctional glucose metabolism, for example, in the brain and heart.

To quantify the rate of lactate and bicarbonate production from pyruvate, pharmacokinetic (PK) models have previously been used to describe the dynamics and estimate values for k_{PL}, the pyruvate-to-lactate conversion rate constant, and k_{PB}, the pyruvate-to-bicarbonate conversion rate constant[7–10]. As a metric, k_{PL} is critical for cancer treatment planning to differentiate aggressive tumors from indolent ones[4,5]. PK models are used to describe the biochemical interactions of pyruvate and its conversion to its metabolic products described by a set of differential equations. These equations can be solved to model the pyruvate, lactate, and bicarbonate dynamics given values of k_{PL} and k_{PB} in 1/s. With such a model, acquired dynamics per voxel can be used to fit k_{PL} and k_{PB}, and estimate k_{PL} and k_{PB} maps.

Existing PK models do not currently account for the signal progression of a metabolite-specific balanced SSFP (MS-bSSFP) acquisition. MS-bSSFP HP ^{13}C studies have recently emerged as an alternative to typical spoiled GRE sequences due to their improved SNR. With a bSSFP sequence, the transverse magnetization is refocused every TR rather than spoiled, which preserves more of the quickly decaying HP magnetization. Previous studies have demonstrated two to three-fold SNR improvement when a MS-bSSFP sequence was used to acquire ^{13}C-lactate[11], [^{13}C,^{15}N]-urea[12] and ^{13}C-bicarbonate[13]. The improved SNR is paramount to furthering HP ^{13}C technologies and improving resolution in low-yield metabolites.

To fully take advantage of the MS-bSSFP studies, PK models must be adapted for bSSFP acquisitions which have inherent differences compared to spoiled GRE acquisitions, such as T_2/T_1 contrast and refocusing of transverse magnetizations across each TR. The objective of this work is to derive a bSSFP PK model that can be used for MS-bSSFP HP ^{13}C acquisitions[14–16]. We have built a flexible framework to model both bSSFP and GRE acquisitions for HP ^{13}C metabolites to estimate k_{PL} and k_{PB} values per voxel. The bSSFP PK model-based k_{PL} and k_{PB} estimates will be validated using two previously acquired paired datasets[11,13] with MS-bSSFP and GRE acquisitions. Estimates will be compared to a previous GRE method[9]. Simulations and in vivo data will be used to assess the model's sensitivity to input parameters particularly, ^{13}C-lactate T_2 (T_{2L}).

4.3 Theory

For HP C13 data acquisition with a metabolite-specific methodology, we can effectively use a different sequence for each metabolite where the excitations and readouts of different

metabolites are interleaved with each other. We developed a model supporting multiple pulse sequences, which we will call the GRE-bSSFP model, that includes a GRE acquisition for pyruvate followed by a bSSFP or GRE acquisition for lactate and bicarbonate.

Thus, the objective of this work is:

1. Model the bSSFP signal
2. Incorporate the modeled bSSFP signal for a single metabolite within an acquisition where other metabolites may be acquired with a GRE acquisition
3. Account for acquisition and reconstruction differences between bSSFP and GRE
4. Estimate the arterial input function

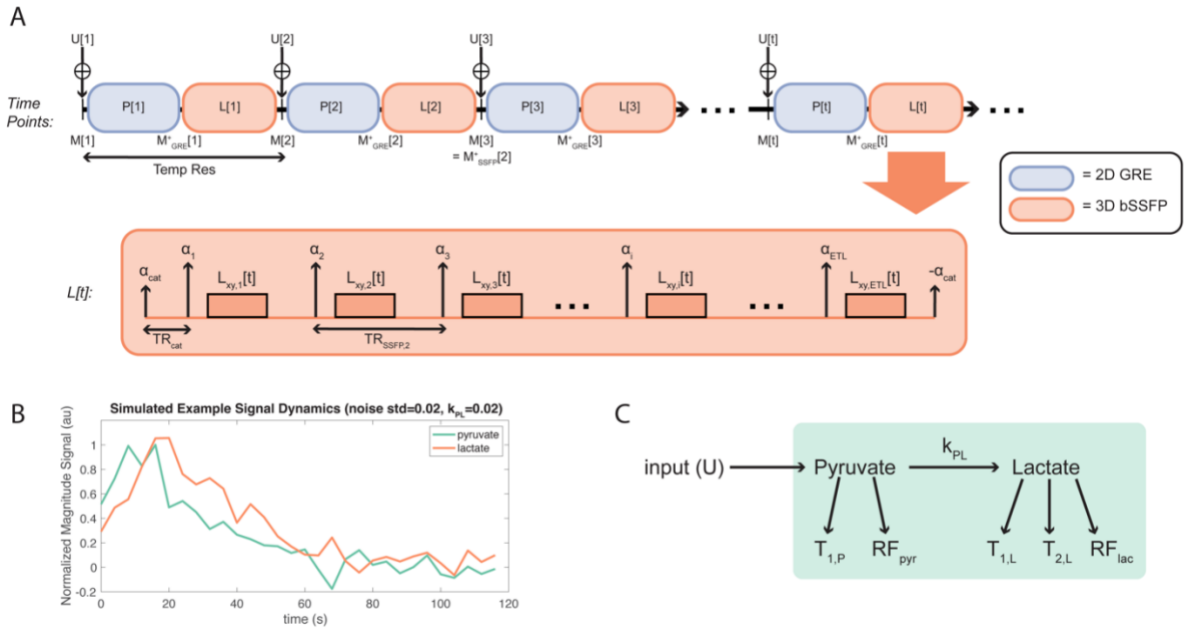

Figure 4.1: Overview of bSSFP model. Model diagram shows the interleaved metabolite-specific 2D GRE pyruvate and 3D bSSFP lactate acquisitions. Lactate is acquired with a 3D bSSFP acquisition with alternating flip angles. New hyperpolarized signal is introduced every time point via the input function (U). Note the catalyzation pulses (bSSFP preparation echoes) are simplified in the diagram. (B) Sample dynamics of simulated pyruvate and lactate dynamics with added noise. (C) Diagram of the one physical compartment, two-site pharmacokinetic model with unidirectional conversion. U = input function, P = pyruvate, L = lactate, α = RF flip angles, M = net magnetization vector, cat = catalyzation, t = time point, I = excitation number, ETL = echo train length, k_{PL} = pyruvate-to-lactate rate constant

4.3.1 Alternating MS-GRE and MS-bSSFP Model

A pharmacokinetic model with one physical compartment was used to estimate magnetization evolution across repetition times for a MS-bSSFP acquisition. This GRE-bSSFP model is flexible and allows for pyruvate and up to three metabolites. For each of these metabolites, there is a choice as to whether they were acquired with a 3D bSSFP, 2D GRE or 3D GRE metabolite-specific acquisition. For simplicity, **Figure 4.1** and Eqs. 4.1-4.11 will outline the two-site situation where pyruvate is acquired with a 2D GRE sequence and lactate is acquired with a 3D bSSFP sequence.

During each TR, we can assume there are three conversion and decay processes happening: (1) pyruvate is converted to lactate (this is assumed to be unidirectional, but can trivially be made bi-directional), (2) pyruvate and lactate decay due to T_1 and T_2 relaxation and (3) some pyruvate and lactate magnetization is lost due to excitation pulse effects. Some further assumptions can also be made to simplify the model: there's no off-resonance, the excitation pulse is instantaneous (i.e. there is no signal decay during excitation), metabolic conversion between pyruvate and lactate only occurs in the longitudinal (z) components and pyruvate-to-lactate conversion is unidirectional (i.e. k_{LP}, lactate-to-pyruvate conversion is neglected). The model also neglects any equilibrium magnetization, as this is typically orders of magnitude lower than the hyperpolarized magnetization. With these assumptions, we model the magnetization in a discrete-continuous fashion as follows.

The magnetization at the end of time point, t, M[t], for the two metabolites can be separated into its transverse and longitudinal components as a vector:

$$M[t] = \left[P_x[t], P_y[t], P_z[t], L_x[t], L_y[t], L_z[t]\right]^T \quad 4.1$$

For pyruvate acquisition (2D GRE), the input for timepoint t, U[t], is added to the prior magnetization. Then, the magnetization is calculated after an excitation pulse with flip angle, α, which is modelled as a rotation matrix:

$$M_{GRE}[t] = rot_P(\alpha_P) \cdot spoil \cdot (M[t-1] + U[t]) \quad 4.2$$

where

$$rot_P(\alpha_P) = \begin{bmatrix} rotation(\alpha_P) & 0 \\ 0 & I_3 \end{bmatrix} \quad 4.3$$

$$spoil = \begin{bmatrix} diag([0\ 0\ 1]) & 0 \\ 0 & diag([0\ 0\ 1]) \end{bmatrix} \quad 4.4$$

Here, rotation(α_P) is a 3D rotation matrix about the y-axis with rotation angle α_P. The final pyruvate signal at timepoint t, P[t], is:

$$P[t] = M_{GRE}^{(1)}[t] + iM_{GRE}^{(2)}[t] \quad 4.5$$

Where (1) and (2) are the first and second elements of the M_{GRE} vector at time t. The rest of the pyruvate acquisition period is modeled to get the magnetization at the end of pyruvate acquisition for time t, M^+_{GRE}:

$$M_{GRE}^+[t] = spoil \cdot exp(R \cdot \tau_{GRE}) \cdot M_{GRE}[t] \quad 4.6$$

where τ_{GRE} is the total acquisition time for the GRE acquisition and R is the matrix that contains the metabolic rate constants and relaxation rates:

$$R = \begin{bmatrix} -R_{2,P} & 0 & 0 & 0 & 0 & 0 \\ 0 & -R_{2,P} & 0 & 0 & 0 & 0 \\ 0 & 0 & -k_{PL} - R_{1,P} & 0 & 0 & 0 \\ 0 & 0 & 0 & -R_{2,L} & 0 & 0 \\ 0 & 0 & 0 & 0 & -R_{2,L} & 0 \\ 0 & 0 & k_{PL} & 0 & 0 & -R_{1,L} \end{bmatrix} \quad 4.7$$

Here, k_{PL} is the apparent rate constant for pyruvate to lactate conversion, and R_1 and R_2 are the reciprocals of the T_1 and T_2 relaxation rate constants. Eqs. 4.6 and 4.7 are the solution to a one physical compartment, two-site exchange model, with unidirectional conversion and no input to the system[9]. Note that because of the result of the *spoil* operation, $R_{2,P}$ is ultimately not included in the model fit.

For lactate acquisition (3D bSSFP) including a series of catalyzation pulses (labelled "cat") the magnetization vector at each phase encode, i, can be calculated:

$$M_{SSFP,i}[t] = \left(\prod_{j=1}^{i} rot_L(\alpha_{L,j}) \cdot exp(R \cdot TR_{SSFP,j}) \right) \cdot \left(\prod_{k=1}^{K} rot_L(\alpha_{cat,k}) \cdot exp(R \cdot TR_{cat,k}) \right) \cdot M_{GRE}^{+}[t] \quad 4.8$$

Where TR is the repetition time, K is the number of catalyzation pulses and

$$rot_L(\alpha_L) = \begin{bmatrix} I_3 & 0 \\ 0 & rotation(\alpha_L) \end{bmatrix} \quad 4.9$$

Catalyzation pulses, or bSSFP preparation echoes, gradually increase in flip angle prior to image acquisition and are necessary for efficiently and smoothly reaching a stable, pseudo steady-state bSSFP frequency response[17,18]. After image acquisition, reversed catalyzation pulses are used to restore magnetization to Mz to preserve magnetization. For the bSSFP acquisition, the sign of the flip angle is alternated each TR. The final lactate signal for time point, t, is calculated as follows:

$$L[t] = \frac{\sum_{i=1}^{N_{PE}} L_{xy,i}[t]}{N_{PE}} = \frac{\sum_{i=1}^{N_{PE}} \left(M_{SSFP,i}^{(4)}[t] + iM_{SSFP,i}^{(5)}[t] \right)}{N_{PE}} \quad 4.10$$

where N_{PE} is the number of phase encodes for the lactate acquisition. Finally, the magnetization at the end of the timepoint, M[t+1], after reversed catalyzation can be calculated as:

$$M[t+1] = M_{SSFP}^{+}[t] = \left(\prod_{k=1}^{K} rot_L(-\alpha_{cat,k}) \cdot exp(R \cdot TR_{cat,k}) \right) \cdot M_{SSFP,N_{PE}}[t] \quad 4.10$$

For simplicity, the two-site case of pyruvate to lactate conversion is described in the Eqs. 4.1-4.11 above but these equations can be expanded to allow for additional metabolites, such as bicarbonate. These updated equations can be found in the supporting materials.

4.3.2 Acquisition differences between GRE and bSSFP acquisitions

Either a 2D or 3D GRE pyruvate acquisition followed by a 3D bSSFP acquisition was used to acquire the in vivo data. The bSSFP and GRE acquisitions have different acquisition times, and the SNR is dependent on the total acquisition time as follows:

$$SNR \propto voxel\ size \cdot \sqrt{total\ acq\ time} = voxel\ size \cdot \sqrt{N_{PE}\, T_{READ}} \quad 4.12$$

Where T_{READ} is the readout duration in a single TR.

The signal scaling in the resulting images will depend on whether the raw data is averaged or accumulated. However, this expected SNR change can be used to normalize the acquisitions regardless of what signal scaling is present between the two sequences.

4.3.3 Arterial Input Function Estimation

An important modeling consideration is the perfusion of the ^{13}C-pyruvate into the tissue of interest, otherwise known as the input function. Previously, there has been success modeling the input function from pyruvate dynamics, called inputless fitting[19,9]. With inputless fitting, the model of choice, in this case the GRE-bSSFP model, is used to estimate the pyruvate signal for time point t given pyruvate at time t-1. As the model inherently does not take into account added signal from pyruvate coming into the tissue, the difference between the modeled signal at time t and the acquired signal at time t is estimated as the input for time t. In this work, the input function is estimated with this method, i.e., inputless fitting using the model and acquired pyruvate signal.

4.4 Methods

4.4.1 In Vivo Data Acquisition and Reconstruction

Previously acquired datasets were used to evaluate the model in vivo[11,13]. The following is a brief description of the parameters. For a complete description of the acquisition protocols, imaging parameters and reconstruction please reference the original texts[11,13].

Tang et al.[11] measured pyruvate and lactate in healthy rat data (n=3), transgenic adenocarcinoma of the mouse prostate (TRAMP, n=3), and human kidney data from patients with renal cell carcinoma (RCC, n=3). For each of these datasets, two HP C-13 scans were acquired on the same day: one where pyruvate and lactate were acquired with a MS-GRE acquisition ("GRE-all") and another where pyruvate was acquired with MS-GRE and lactate was acquired with a MS-bSSFP acquisition ("lactate-bSSFP"). The MS-bSSFP acquisition included a spectrally selective lactate

excitation pulse and 3D stack-of-spirals acquisition with four in-plane interleaves and 16 stack encodes[11]. For the animal acquisitions, the MS-GRE acquisitions were a 3D stack-of-spiral acquisition with one in-plane encoding and 16 stack encodes and for the human kidney data the MS-GRE acquisitions were 2D multi-slice single-shot spiral acquisition. The GRE acquisitions used a spectral-spatial RF excitation pulse[20].

The animal studies had a resolution of 4 mm x 4 mm x 10mm, 3° flip angle for pyruvate, 60° flip angle with a nonlinear catalyzation sequence for lactate, TR of 100 ms for pyruvate, TR of 15.29 ms for lactate and a temporal resolution of 4s. For the human study, the resolution was 15 mm x 15 mm x 21 mm, 20° flip angle for pyruvate, 60° flip angle with a nonlinear catalyzation sequence for lactate, TR of 100 ms for pyruvate, TR of 15.29 ms for lactate and temporal resolution of 4 s. Single slice Bloch-Seigert B_1^+ maps were acquired prior to metabolic imaging for the human dataset. The B_1^+ maps were centered along the center slice of the kidneys.

Liu et al.[13] measured pyruvate, lactate and bicarbonate in healthy rats (n=5). Two HP C-13 scans were acquired on the same day: one where pyruvate, lactate, and bicarbonate were acquired with an MS-GRE acquisition ("GRE-all") and another where pyruvate and lactate were acquired with an MS-GRE acquisition and bicarbonate was acquired with an MS-bSSFP acquisition ("bicarbonate-bSSFP"). The MS-GRE acquisitions used a pyruvate flip angle of 20°, lactate and bicarbonate flip angles of 30°, a TR of 100 ms and temporal resolution of 2.5 s. The MS-bSSFP acquisition in this study included a spectrally selective bicarbonate excitation pulse, a 3D stack-of-spirals acquisition with four in-plane interleaves and 16 stack encodes, a TR of 9.8 ms, a flip angle of 60° with a non-linear catalyzation sequence, and a temporal resolution of 2.8 s. This

study used a multi-resolution technique: pyruvate had a resolution of 2.5 mm x 2.5 mm x 21 mm, lactate of 5 mm x 5 mm x 21 mm, and bicarbonate of 7.5 mm x 7.5 mm x 21 mm.
For reconstruction for all in vivo datasets, the k-space data was gridded, followed by a 2D or 3D Fourier transform. For the human dataset, the RefPeak coil combination method was used with pyruvate signals as the coil sensitivity maps[21].

Animal studies were conducted under protocols approved by the University of California San Francisco Institutional Animal Care and Use Committee and patient studies were conducted under a University of California San Francisco Institutional Review Board approved protocol.

4.4.2 Preprocessing

For the dataset from Liu et al.[13], the lactate and bicarbonate data was zero-padded in order to match pyruvate resolution after reconstruction. The noise was normalized across the different studies for the MS-bSSFP images. [22,23] To account for the multi-resolution acquisition, the lactate and bicarbonate signal amplitudes were scaled relative to pyruvate based on the expected change in SNR due to the varying voxel sizes. Specifically, lactate was scaled by 1/4 and bicarbonate was scaled by 1/9 (Eq. 4.12).

4.4.3 GRE-to-bSSFP Scaling

For the cases where pyruvate was acquired with a 2D GRE sequence and lactate or bicarbonate was acquired with 3D bSSFP sequence, additional signal scaling was found to be necessary in the model to match the acquired in vivo data from the different sequences. Different approaches were used for the lactate and bicarbonate bSSFP studies to determine the scaling factor.

To determine the scale used for the human dataset from Tang et al.[11], a phantom experiment was performed using a cylindrical 8M ^{13}C-Urea phantom doped with a Gd-based contrast agent such that $T_1 \approx 1$ s. The acquisition parameters were matched with those of the in vivo data except for the 3D bSSFP acquisition, where the TR was lengthened to 500 ms to mitigate T_2 relaxation effects. The phantom data was reconstructed, and the maximum urea signal was used to calculate the ratio between the 2D GRE acquisition and the 3D bSSFP acquisition. From this phantom data, the scale was found to be 6.905 for bSSFP/GRE for the FOV and flip angle parameters used in the human in vivo data. The scale was validated with simulations by comparing the relative peak amplitudes between pyruvate and lactate with the scaled modeled data and the in vivo data. During the fitting procedure, the modeled bSSFP (lactate) signal curves were scaled by 6.905 before fitting to the in vivo data.

For the dataset from Liu et al.[13], a range of scaling factors were iterated over to determine the scale that would result in the best correspondence between the fit k_{PB} from the "GRE-all" and "bicarbonate-bSSFP" acquisitions. This scale value was found to be 1.8.

4.4.4 k_{PL} and k_{PB} Fitting

The model described in Eqs. 4.1-4.11 was implemented in MATLAB (Mathworks, Natick, MA, USA). A nonlinear least squares optimization (lsqnonlin() on MATLAB) was used to fit the signal dynamics to one or more variables. The normalized root mean square error (NRMSE) between simulated and fit curves was calculated to evaluate fit quality. The model and fitting function are available in the Hyperpolarized MRI Toolbox[11].

During fitting, pyruvate T_1 was fixed to 30 s, lactate T_1 was fixed to 25 s and bicarbonate T_1 was fixed to 10s[9,13,24]. The input functions were estimated from pyruvate using the model (inputless[9,19]).

For Tang et al.[11] data, k_{PL} and/or lactate T_{2L} were fit while all other parameters were fixed. Lactate T_2 was either jointly fit with k_{PL} or fixed to 0.8 s (for healthy rat kidney and human kidney datasets) or 1.3 s (for TRAMP dataset). These T_{2L} values were chosen empirically to give the best fits and lowest NMRSE across all datasets. For the animal data, no scaling was used but for the human studies a scale of 6.905 was used. Additionally, when fitting k_{PL} for the human RCC dataset, the Bloch-Seigert B_1^+ maps were used to scale the flip angles in the fitting model either per voxel for voxel-wise k_{PL} fitting or as an average scale for average signal k_{PL} fitting. For Liu et al.[23] data, k_{PL} and k_{PB} were fit while the remaining parameters were fixed. Bicarbonate T_2 (T_{2B}) was fixed to 0.5 s for this study[13].

For the healthy rat kidney and human RCC datasets, ROI masks of the kidneys were manually drawn. The same was done for the tumor of the TRAMP dataset. When fitting rate constants voxel-wise on the datasets from Tang et al.[11], the ROI mask that was dilated in 2D was used for rate constant fitting and then masked with the true ROI mask for display. For the Liu et al.[13] dataset, true ROIs were used for the entire analysis. For scatter plot displays of the k_{PL} and k_{PB} maps, a linear trend line was fit with a fixed y-intercept of 0. Outliers were removed using the interquartile range method when fitting the linear trend line. Pearson correlation coefficient (PCC) was computed including outliers. Lactate/pyruvate and bicarbonate/pyruvate area-under-

the-curve (AUC) ratio maps were calculated by dividing the sum of the lactate and bicarbonate images over time by the sum of pyruvate images over time.

For validation, the fit k_{PL} and k_{PB} values were compared to k_{PL} and k_{PB} values fit using the inputless GRE fitting model on the corresponding "GRE-all" datasets[9]. The pyruvate T_1 was fixed to 30 s, lactate T_1 was fixed to 25 s, bicarbonate T_1 was fixed to 10s, and the input was estimated from pyruvate. This GRE model is available publicly in the Hyperpolarized MRI Toolbox[22].

4.4.5 Simulation

To evaluate the robustness of the model and fitting method, simulated "lactate-bSSFP" data was created using the GRE-bSSFP model using a gamma-variate input function and added random noise. The following parameters were used: T_{1P}=30 s, T_{1L}=25 s, T_{2L}=1 s, k_{PL}=0.02 1/s, std_noise=0.02, $T_{arrival}$=0, T_{bolus}=8, TR_P = 0.18 s, TR_L=0.01529 s to best mimic the acquired dataset. The flip angle for pyruvate was 20°, and the flip angle for lactate was 60° with 76 phase encodes, including the catalyzation sequence. The k_{PL} was then fit and the effect of perturbations to the input variables was observed using Monte Carlo simulations (N=100).

4.5 Results

4.5.1 Simulations

A Monte Carlo simulation was used to compare fitting methods of simulated "lactate-bSSFP" experiment signal curves with added random noise (**Figure 4.2**). Using a GRE signal model for bSSFP data resulted in biased k_{PL} results (**Figure 4.2A**) whereas the k_{PL} values fit with the GRE-

bSSFP fitting method matched the simulated k_{PL}s (**Figure 4.2A**, **4.2B**). The GRE fitting method overestimated the k_{PL} due to model mismatch as it fails to take into account increased lactate SNR from the refocusing during the bSSFP acquisition.

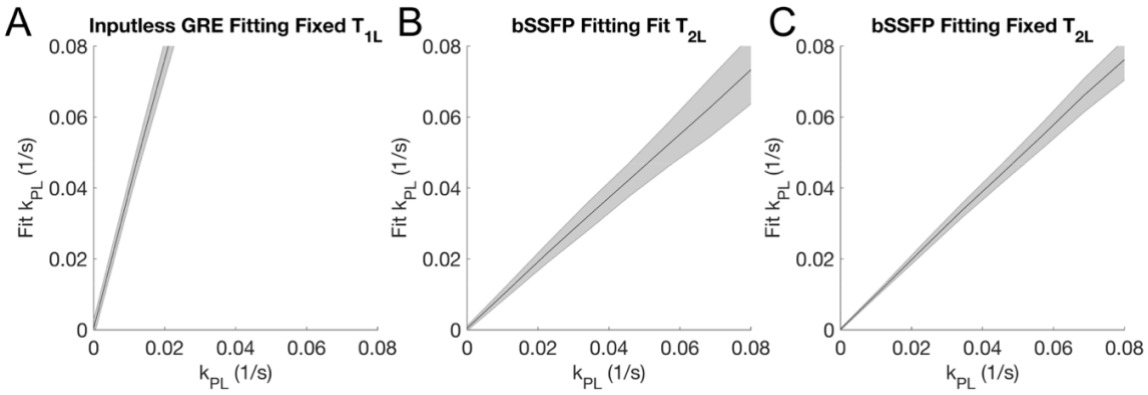

Figure 4.2: The estimated vs simulated k_{PL} for the bSSFP & GRE models for the Monte Carlo simulations (Monte Carlo iterations = 100). For GRE fitting, flip angle was set to half of the bSSFP flip angle (30°).

A Monte Carlo simulation was also used to test the robustness of the fitting methods to perturbations in various experimental parameters (**Figure 4.3**). The models were accurate across the range of k_{PL} and low noise levels. They were also robust to changes in the bolus characteristics ($T_{arrival}$, T_{bolus})[9] and T_{1P}. However, the models show strong sensitivity to variations in T_{2L} when T_{2L} was fixed, as well as modest sensitivity to variations in T_{1L}. This indicates that k_{PL} is strongly coupled to T_{2L} in this acquisition. Jointly fitting lactate T_{2L} and k_{PL} reduced this sensitivity of the model, but at the expense of increased expected variance. When fixing T_{2L}, the model also showed strong sensitivity to B_1^+ errors. However, jointly fitting lactate T_{2L} and k_{PL} reduced sensitivity to B_1^+ error meaning the model may be adjusting the fit lactate T_{2L} values to account for errors in B_1^+. Additionally, with increasing added noise, jointly fitting lactate T_{2L} and k_{PL} resulted in both higher error margins and a negative bias of fit k_{PL}. The jointly fitting method generally resulted in larger error margins than fixing lactate T_{2L}.

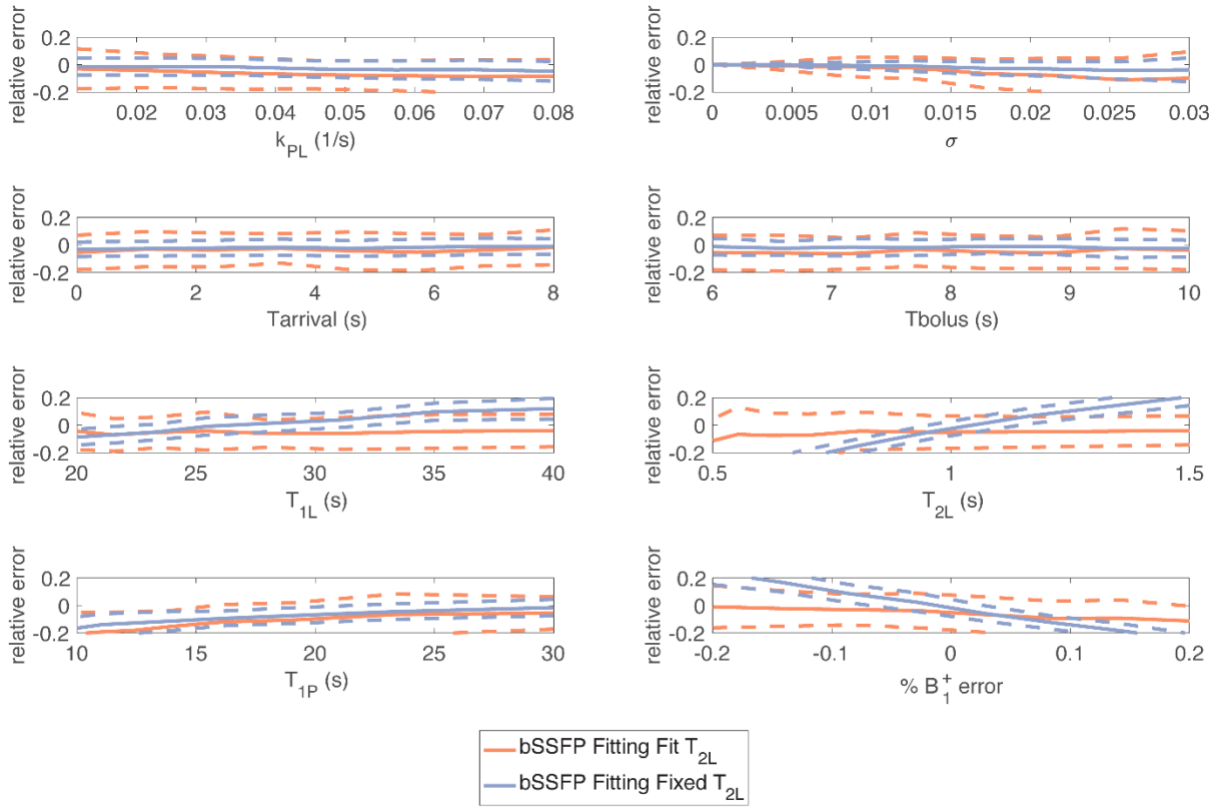

Figure 4.3: Simulated k_{PL} errors of the GRE-bSSFP fitting with perturbations to model parameters (std of noise = 0.02, Monte Carlo iterations=100).

4.5.2 Lactate-bSSFP In Vivo

To show sample fitting results, the average signal dynamics within ROIs were calculated and used to fit average k_{PL} values (**Figure 4.4**). The NRMSE between the actual signal curves and fit curves for both experiments were all below 0.16 indicating good fits. Using the GRE-bSSFP fitting model on the "lactate-bSSFP" data and the GRE model on the "GRE-all" data, resulted in very similar k_{PL} values.

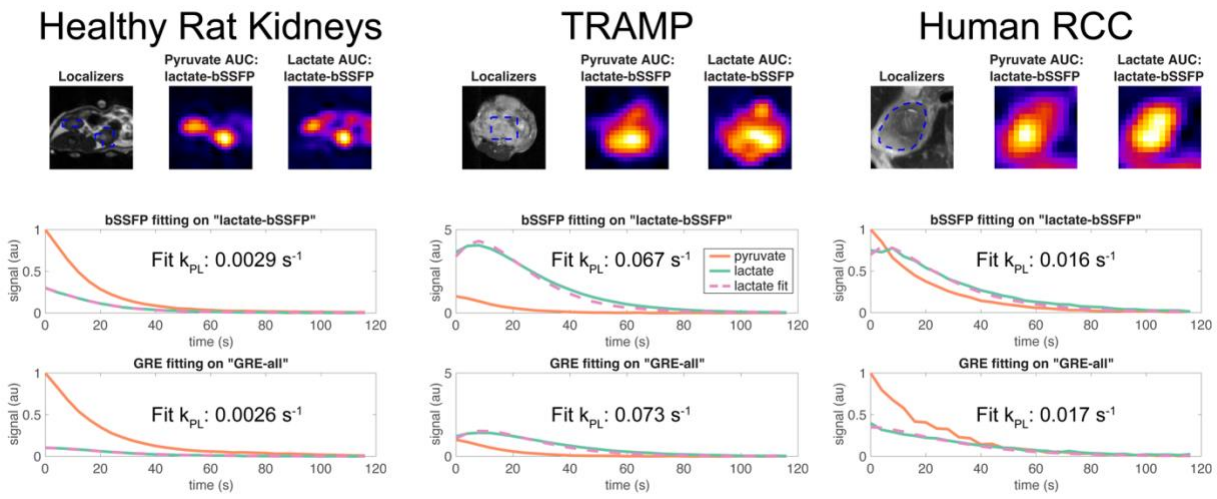

Figure 4.4: Sample data and fitting results across the Tang et al.[11] datasets used. For each in vivo dataset, an example case is displayed with localizers annotated with the ROI, and pyruvate and lactate AUC images from the "lactate-bSSFP" experiment. The average signal within the ROI is fit to k_{PL} using the GRE-bSSFP fitting model for the "lactate-bSSFP" experiment with fixed T_{2L} (middle row). The average signal from the "GRE-all" experiment is fit to k_{PL} using the GRE model (bottom row). Examples used are subject 2 for healthy rat kidneys, subject 2 for TRAMP, and subject 1 for human RCC.

Next, the individual voxel data was used to fit k_{PL} parameter maps in the lactate-bSSFP experiments. These parameter maps were compared to k_{PL} parameter maps fit using the GRE fitting method on the GRE-all dataset (**Figure 4.5**). The k_{PL} values and parameter map patterns matched between the two methods and datasets. The maps showed similar patterns of spatial heterogeneity, including higher k_{PL} in the medulla of the kidneys and lower k_{PL} in the center of the human kidney which likely reflects necrosis in the RCC tumor. The k_{PL} maps also showed similar patterns and heterogeneity to the lactate/pyruvate AUC ratio maps.

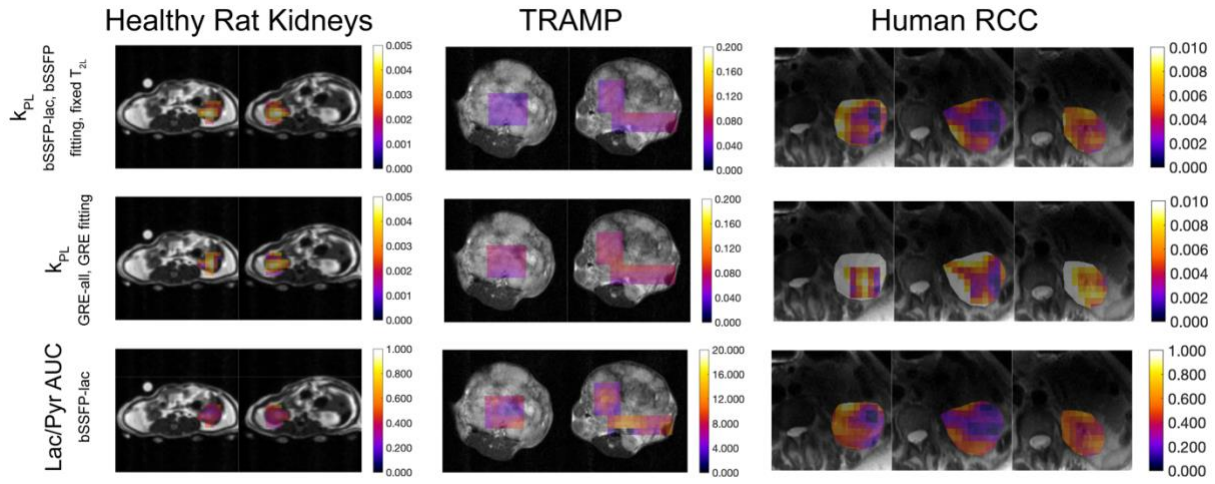

Figure 4.5: Sample metabolism maps across the Tang et al.[11] datasets used. An example case from each dataset of the fit k_{PL} maps using the GRE-bSSFP model on the "lactate-bSSFP" data (first row) compared with k_{PL} values fit with a GRE model[9] on the "GRE-all" data (second row) and lactate/pyruvate AUC ratio maps of the "lactate-bSSFP" data (third row). Examples used are subject 1 for healthy rat kidneys, subject 2 for TRAMP and subject 2 for human RCC. For the healthy rat kidneys and human RCC the T_{2L} was fixed to 0.8 s and for the TRAMP the T_{2L} was fixed to 1.3 s.

The voxel-wise k_{PL} values were compared in scatter plots for all datasets (**Figure 4.6** and **4.7**). Each point in the plots correspond to one voxel where k_{PL} was estimated using the GRE-bSSFP model on the "lactate-bSSFP" data and k_{PL} was estimated using the GRE model on the "GRE-all" data. The lactate/pyruvate AUC ratio values were also calculated per voxel for "lactate-bSSFP" and "GRE-all" data. These lactate/pyruvate AUC ratio values are often used as metabolism metrics in HP ^{13}C studies. When comparing AUC ratio values to k_{PL} values a positive linear relationship is expected[9]. For each scatter plot a line of best fit was fit and the slope reported after removing outliers. With fixed T_{2L}, the Pearson correlation coefficients for bSSFP AUC ratio vs bSSFP k_{PL} were 0.476, 0.229, and 0.915 for the healthy rat kidneys, TRAMP, and human RCC, respectively, suggesting positive linear correlations. Other than the healthy rat kidneys, the correlation coefficients were similar to the GRE AUC ratio vs GRE k_{PL} coefficients.

Across animal and human datasets, the GRE-bSSFP fitting method matched the GRE results better when fixing T_{2L} versus fitting T_{2L} (**Figure 4.7**). With fixed T_{2L}, for GRE k_{PL} vs bSSFP k_{PL} the best fit line slopes were 0.816 for healthy rat kidneys, 0.833 for TRAMP, and 0.632 for human RCC. These slopes were all close to 1 and to the x=y reference line. The correlation coefficients for GRE k_{PL} vs bSSFP k_{PL} showed positive linear correlations for the TRAMP and human RCC datasets. In contrast, when k_{PL} and T_{2L} were jointly fit, the best fit line slopes deviated further from 1 and the x=y reference line. The fit T_{2L} values when jointly fitting k_{PL} and T_{2L} demonstrated high variability in all three datasets for at least one subject.

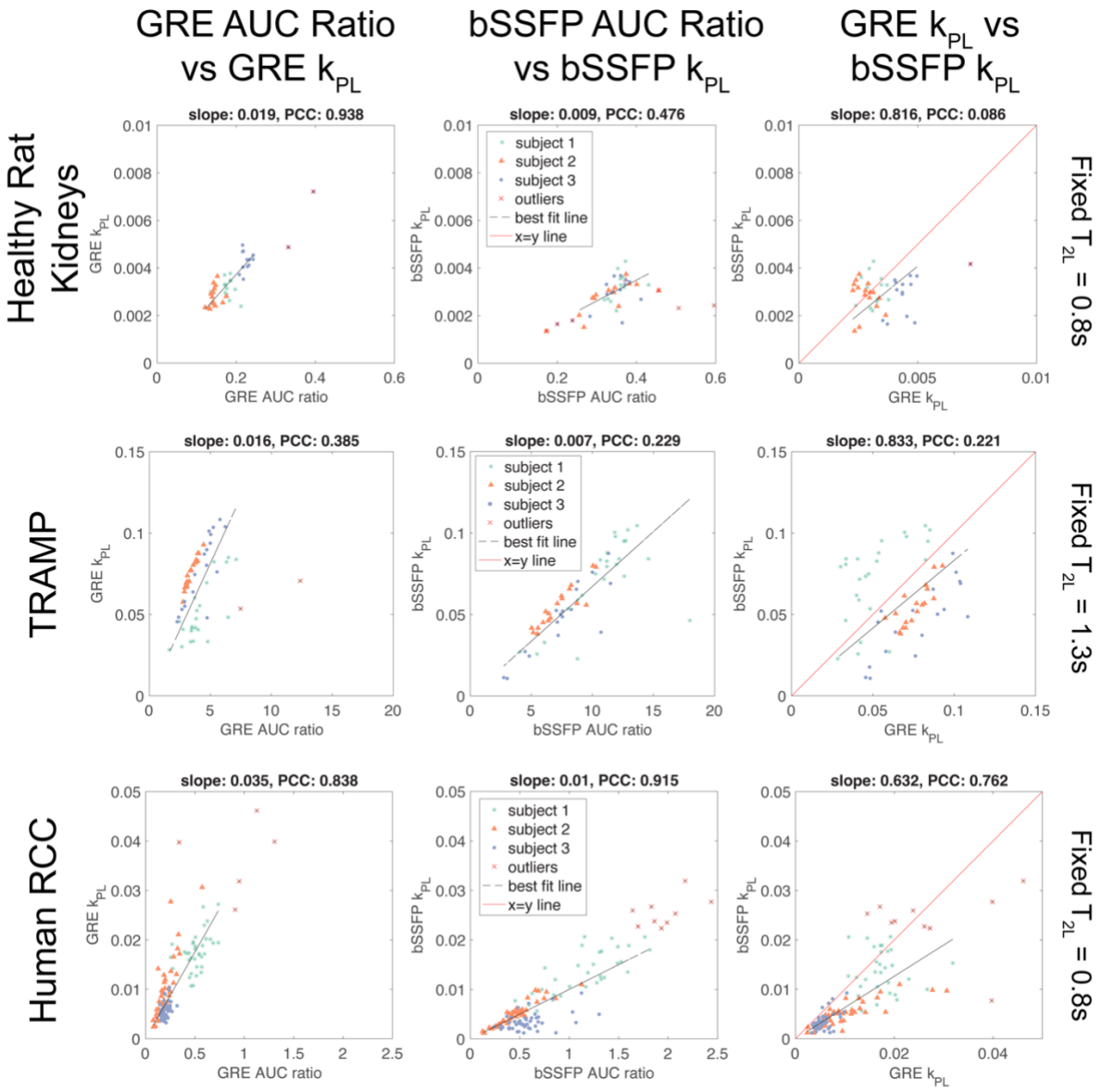

Figure 4.6: Voxel-wise comparisons of the metabolism fitting methods. For each dataset in Tang et al.[11] and all voxels within each ROI, bSSFP k_{PL} values compared to "lactate-bSSFP" lactate/pyruvate AUC ratios and GRE k_{PL} values fit using the GRE model on "GRE-all" data. Note for TRAMP "lactate-bSSFP" AUC plots, one outlier is not displayed.

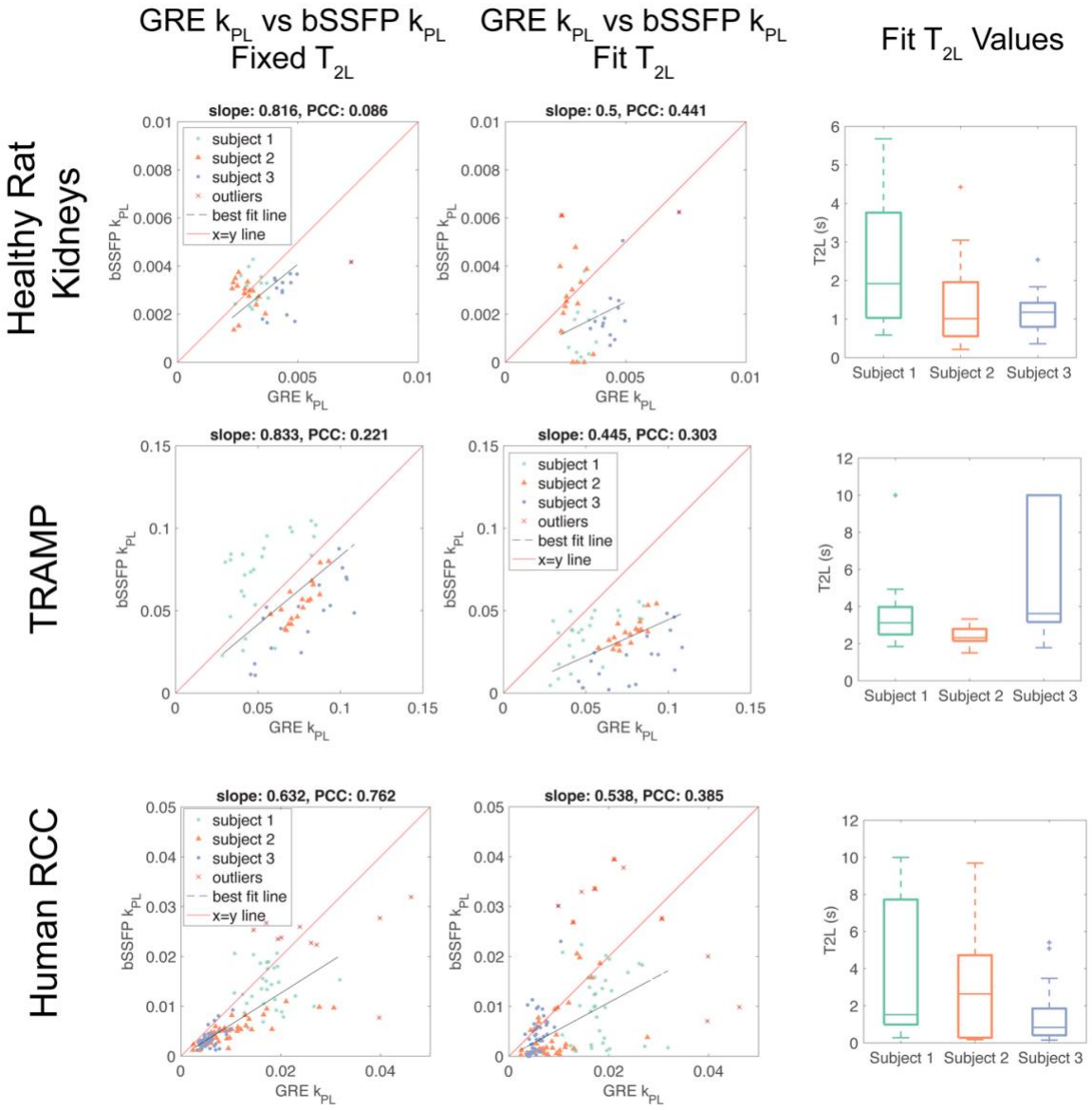

Figure 4.7: Comparison of fitting versus fixing T_{2L} when comparing voxel-wise GRE model and GRE-bSSFP model fits across the Tang et al.[11] datasets. Additionally, distribution of fit T_{2L} values across voxels for each subject is shown (right column).

The sensitivity of the model to the value of the fixed lactate T_2 was also explored on the lactate-bSSFP in vivo data (**Figure 4.8**). Scatter plots comparing the two fitting methods with their respective datasets per voxel were visualized for a range of fixed lactate T_2s. For all datasets, the slope of the best fit line decreased with increasing T_{2L}. The fit bSSFP k_{PL} values approached zero

as T_{2L} increased. The slope of the trend lines also varied per subject. For example, TRAMP subject 1 had higher slopes than the other two subjects for the range of T_{2L}s.

These results agree with the Monte Carlo parameter sensitivity simulations in **Figure 4.3**. Using these plots, across all subjects, a lactate T_2 of 1.3 s for TRAMP data and 0.8 s for healthy rat kidney and human RCC data provided the best matching between the two fitting methods. This is how the fixed T_{2L} values were chosen.

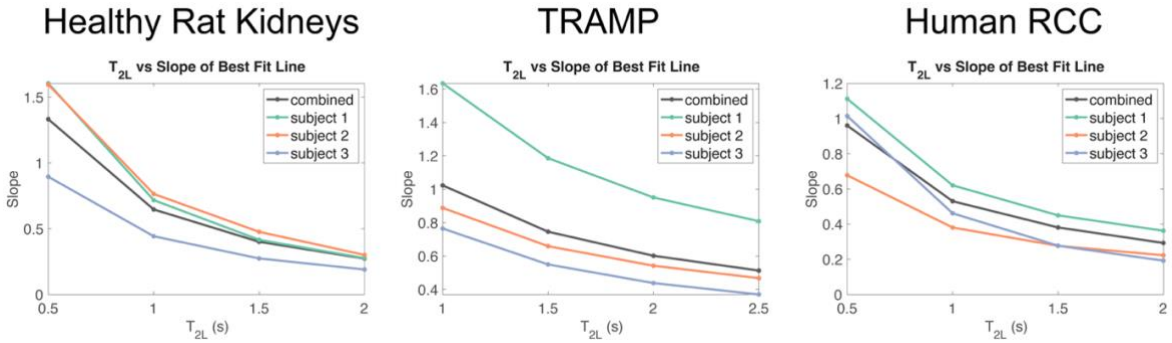

Figure 4.8: Impact of T_{2L} on the fitting results. For each in vivo dataset from Tang et al.[11], the GRE k_{PL} fit (using the GRE model on the "GRE-all" data) versus the bSSFP k_{PL} fit (using the GRE-bSSFP model on the "lactate-bSSFP" data) per each voxel was plotted for a range of fixed T_{2L}s. The slope for the best fit line for each T_{2L} value is reported across all subjects and per subject.

4.5.3 Bicarbonate-bSSFP In Vivo

Similar analysis was performed on the bicarbonate-bSSFP healthy rat dataset from Liu et al.[13]

The average signal in the kidneys was used to fit k_{PL} and k_{PB} for both the bicarbonate-bSSFP using the GRE-bSSFP model and GRE-all data using the GRE model (**Figure 4.9A**). The k_{PL} and k_{PB} values fit between the two experiments were very similar.

Next, k_{PB} was fit voxelwise within the healthy rat kidneys for the bicarbonate-bSSFP and GRE-all experiments. The fit values matched well and showed similar spatial patterns.

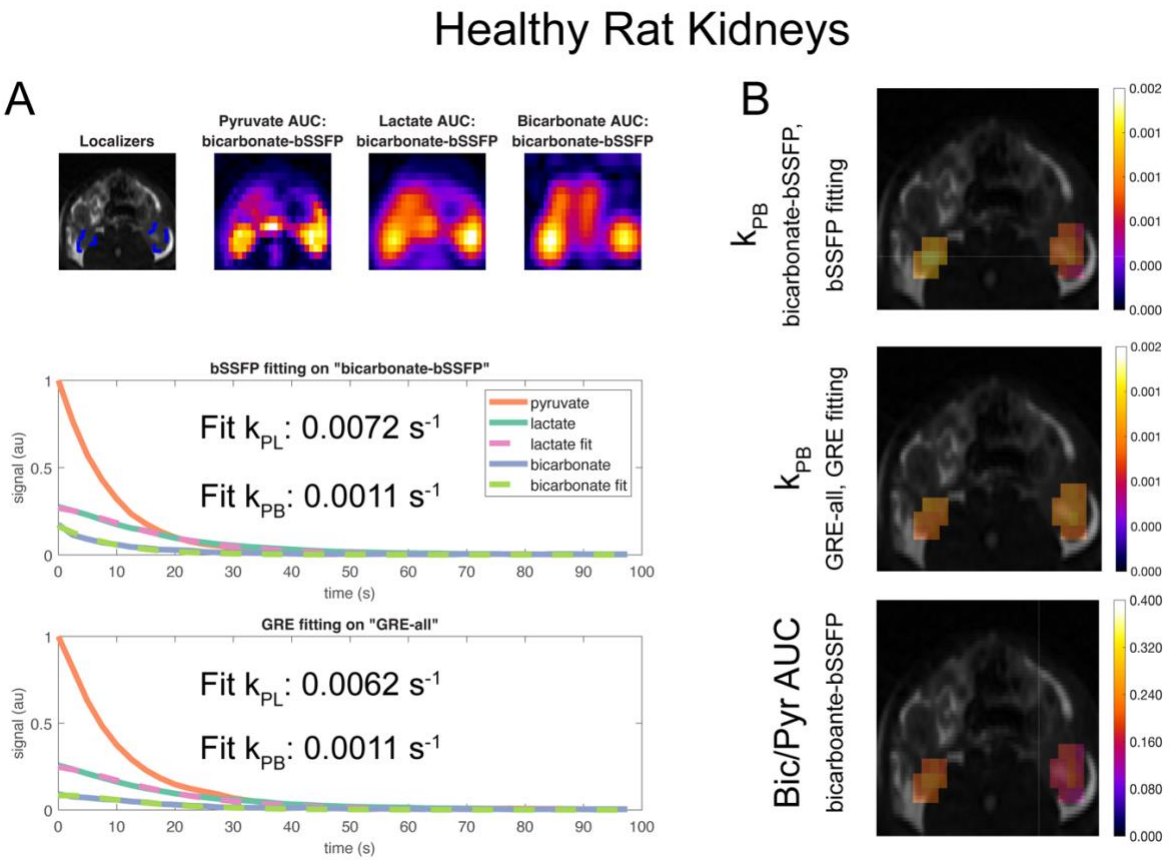

Figure 4.9: Sample data, average fitting results and voxelwise fitting results for the Liu et al.[13] dataset that included bicarbonate. (A) An example healthy rat dataset (subject 1) is displayed with localizers annotated with the kidney ROI, and pyruvate, lactate and bicarbonate AUC images from the bicarbonate-bSSFP experiments. The average signal within the ROI is fit to k_{PL} and k_{PB} using the GRE-bSSFP fitting model for the "bicarbonate-bSSFP" experiment (middle row). The average signal from the "GRE-all" experiment is fit to k_{PL} and k_{PB} using the GRE model (bottom row). The lactate signal is scaled by a factor of 2 and bicarbonate by a factor of 10 for better visualization. (B) Sample k_{PB} maps from one subject (subject 1) using the GRE-bSSFP model on the "bicarbonate-bSSFP" data (first row) compared with k_{PB} values fit with a GRE model[9] on the "GRE-all" data (second row) and bicarbonate/pyruvate AUC ratio maps of the "bicarbonate-bSSFP" data (third row).

Voxel-wise k_{PB} values were compared in scatter plots for the healthy rat kidney data from Liu et al.[13] (**Figure 4.10**). The Pearson correlation coefficients between AUC ratio vs k_{PL} were 0.730 and 0.517 for the "GRE-all" and "bicarbonate-bSSFP" data, respectively, suggesting a positive linear correlation. The GRE k_{PB} vs bSSFP k_{PB} best fit line slope was 0.697. Subject 5 notably

showed the worst correlation in GRE k_{PB} vs bSSFP k_{PB} and demonstrated less linearity with respect to the other subjects in the GRE AUC ratio vs GRE k_{PB} plot as well.

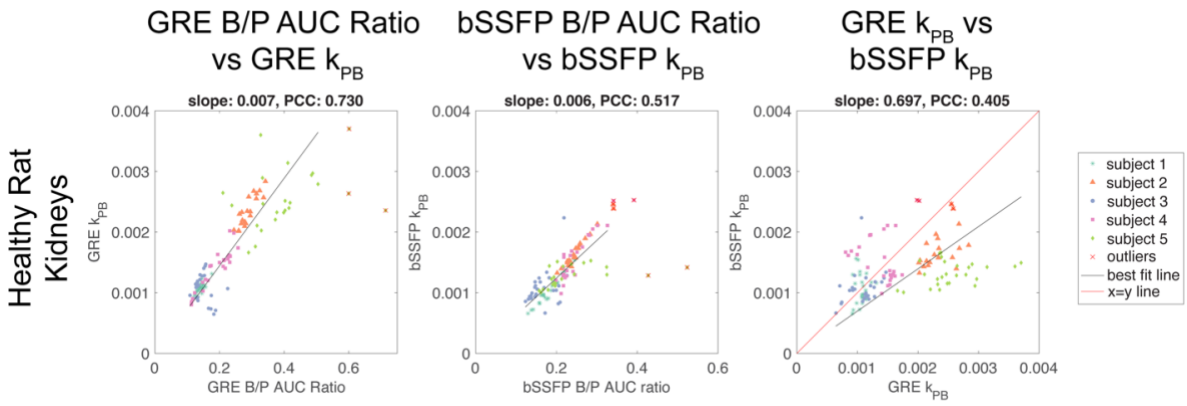

Figure 4.10: Voxel-wise comparisons of the metabolism fitting methods. For each dataset and all voxels within each ROI, bSSFP k_{PB} values are compared to "bicarbonate-bSSFP" bicarbonate/pyruvate AUC ratios and GRE k_{PB} values fit using the GRE model on "GRE-all" data. (B/P = Bicarbonate/Pyruvate)

4.6 Discussion

In this work, a novel pharmacokinetic model for MS-bSSFP HP ^{13}C MRI was described and validated. Through simulations (**Figures 4.2** and **4.3**), the GRE-bSSFP model performed better than the GRE model on "lactate-bSSFP" simulated data due to differences in the acquisition. A bSSFP sequence refocuses transverse magnetization and has T_2/T_1 contrast, which is advantageous to preserve SNR of the transient HP signals, but also differs greatly from spoiled GRE acquisitions, necessitating this updated PK model. The simulations demonstrated that jointly fitting T_{2L} and k_{PL} resulted in higher noise variance but greater robustness to T_{2L} and B_1^+ errors.

To validate the model, previously acquired animal and human datasets were used that included two HP ^{13}C injections, one where pyruvate was acquired with GRE and lactate or bicarbonate

were acquired with bSSFP acquisitions ("lactate-bSSFP", "bicarbonate-bSSFP") and another where all metabolites were acquired with a GRE sequence ("GRE-all")[11,13]. The GRE-all data was fit to k_{PL} and k_{PB} values using a previous GRE model[9]. These values served as comparisons for the k_{PL} and k_{PB} values that were fit with our GRE-bSSFP model to the "lactate-bSSFP" and "bicarbonate-bSSFP" data.

We showed high consistency and similar spatial patterns in k_{PL} and k_{PB} values across the healthy rat kidneys, TRAMP mouse, and human RCC datasets. Across the datasets, the human RCC data from Tang et al.[11] showed the most consistency in k_{PL} between the methods in **Figure 4.6** with the highest correlation coefficient. Meanwhile, the Tang et al.[11] healthy rat kidney results were the most variable with a low correlation coefficient, which could in part be explained by model mismatch, as the kidneys may accumulate lactate substantially due to their role in filtering the blood. Our model does not account for lactate originating outside of the voxel. We expect that some inconsistency in these results could also be explained by B_1^+ calibration errors, as this can directly lead to changes in kinetic rates and AUC ratios.

The results from the bicarbonate-bSSFP data from Liu et al.[13] demonstrated that when the GRE-bSSFP model was extended to incorporate another metabolite, bicarbonate, the fit k_{PB} values matched the GRE-all results. Subject 5 in the Liu et al.[13] dataset had the worst correlation in GRE k_{PB} vs bSSFP k_{PB} and was not as linear with respect to the other subjects in the GRE AUC vs k_{PB} plot (**Figure 4.10**). These results could suggest a difference in the acquisition of subject 5, such as acquisition timing or B_1^+ power calibration[9].

4.6.1 ^{13}C-Lactate and ^{13}C-bicarbonate T_2

An important consideration while fitting k_{PL} and k_{PB} with the GRE-bSSFP model is the T_{2L} and T_{2B}. It is difficult to measure T_2 in vivo from these metabolic products and thus few previous sources exist which have measured or estimated T_{2L} and T_{2B} in vivo[13,25,26]. With the in vivo data results (**Figure 4.7**), we showed that fitting T_{2L} may lead to errors in k_{PL} estimation especially in the voxel-wise scenario where noise is more of a concern. Conversely, we also showed the accuracy of the fixed T_{2L} is important as changes in T_{2L} varied the bSSFP k_{PL} relationship with GRE k_{PLS} (**Figure 4.8**).

The results from **Figure 4.8** also potentially suggest some variation in T_{2L} across subjects and experiments, which could potentially be due to the different microstructure and compartmentalization between vasculature, intracellular, and extracellular spaces. The variation across subjects could also be explained for the human RCC cases by their different pathologies. Subject 1 is a chromophobe subtype, subject 2 is a low-grade clear cell case, and subject 3 is a high-grade clear cell case. The variations in apparent or fitted T_{2L} values could also be due to unknown B_1^+ errors. **Figure 4.3** shows that T_{2L} and B_1^+ lead to strong changes in k_{PL} meaning these parameters are tightly coupled in the model. For example, an increase in fit k_{PL} can be due to either increase in T_{2L} or a decrease in B_1^+ error. The fitting of k_{PB} is similarly tightly coupled to bicarbonate T_2. Thus, in this work, the bicarbonate T_2 was fixed to 0.5s when fitting k_{PB}[13]. As a result, we recommend fixing T_2 values to an estimate based on a literature review[13,26,27]. If possible, an empirical experiment can be used to validate chosen T_2.

4.6.2 GRE to bSSFP Scaling

For cases where there were 2D GRE and 3D bSSFP metabolite-specific acquisitions, the modeled data was not scaled properly to in vivo data. In order to compensate for this difference, we used an empirical scale. This empirical scale was found to be highly dependent on the field-of-view, flip angles of the data, and even the reconstruction. Particularly important to consider are noise characteristics between the GRE and bSSFP studies, noise decorrelation before coil combination, and gridding, which can also lead to significant changes in image scaling. In this work, we used two different methods to arrive at the empirical scale. For the Tang et al.[11] human RCC dataset, we used a phantom study to determine the scale and validated this scale with the data. In contrast, for the Liu et al.[13] rat kidney dataset, the scale was arrived at by using an iterative approach. For future studies with new parameters, one of these methods would have to be used to arrive at a scale. However, the iterative method may not be sustainable for finding the scale value, as it necessitates an additional "GRE-all" acquisition. The in vivo metabolite data cannot be used to determine the scale as the bSSFP and GRE acquisitions were acquired for two different metabolites, so the scaling would be obscured by metabolite dynamics and concentrations. Large inaccuracies in the scaling parameter would lead to inaccuracies in estimated k_{PL} and $k_{PB,}$ so it is important to validate this scale with a comparison between scaled simulation and in vivo data, as was done in this work.

4.6.3 Multi-Resolution Data

In Liu et al.[13], ^{13}C-lactate and ^{13}C-bicarbonate were acquired at a coarser resolution than pyruvate to improve SNR for low concentration metabolites[28]. The resolution mismatch was handled by zero-padding the k-space of the coarser resolution metabolites to match the pyruvate

image resolution. Increasing the resolution of metabolites rather than decreasing that of pyruvate, allows for the visualization of smaller structures and may provide more accurate quantification of k_{PL} and k_{PB}[29]. However, it is important to note that this approach assumes uniform signal distribution, meaning finer spatial variations are not captured in the zero-padded ^{13}C-lactate and ^{13}C-bicarbonate images. The healthy rat kidney data displayed low pyruvate AUC in the medulla, and due to its small size, it could not be captured by the ^{13}C-lactate and ^{13}C-bicarbonate images, thus k_{PL} and k_{PB} might be incorrectly inflated in the medulla voxels.

4.6.4 Model Compartment Size

In this work, the model described has one physical compartment. More physical compartments, although more accurate to the biochemistry, result in more unknown parameters that are typically not measured in HP ^{13}C studies. Prior work has shown that using two physical compartment PK models is more appropriate for in vivo HP ^{13}C-pyruvate studies[7]. The model presented here can be integrated into this approach in future work.

4.6.5 Extended Applications

In these experiments, the focus was on experiments where pyruvate was acquired with GRE, and lactate acquired with bSSFP. However, the fitting and modeling framework is flexible and can support pyruvate plus multiple metabolites with each metabolite acquired with bSSFP or GRE. The model could also be readily adapted for variable flip angle acquisitions, or other hyperpolarized reagents. A further application is to other HP bSSFP studies such as multi-echo bSSFP or bSSFP with off-resonant excitations[30–33].

4.7 Conclusions

In this work, we propose and define a MS-bSSFP pharmacokinetic model to use for fitting conversion rate constants, k_{PL} and k_{PB}, for dynamic HP ^{13}C studies. With preclinical and human in vivo acquisitions, this fitting method is shown to provide high quality fits to the data that are relatively consistent with a previous GRE model. Through simulations the model is shown to fit k_{PL} accurately especially with fixed T_{2L}. The choice of T_{2L} is important and directly impacts k_{PL}. Additionally, the model was extended to include bicarbonate and validated with bicarbonate bSSFP data to estimate k_{PB} values which were found to be consistent with those fit with the GRE model. This model provides a strong backbone for MS-bSSFP HP ^{13}C studies, which are increasing in popularity, and can be adjusted for a variety of specific applications or acquisition parameter sets. For fitting k_{PL}, the GRE-bSSFP model is pertinent to quantify and evaluate tumor metabolism for HP ^{13}C studies with metabolite-specific bSSFP acquisitions.

4.8 References

1. Wang ZJ, Ohliger MA, Larson PEZ, Gordon JW, Bok RA, Slater J, et al. Hyperpolarized 13C MRI: State of the Art and Future Directions. *Radiology*. 2019;291(2):273-284. doi:10.1148/radiol.2019182391

2. Nelson S, Kurhanewicz J, Vigneron D, Larson P, Harzstark A, Ferrone M, et al. Metabolic Imaging of Patients with Prostate Cancer Using Hyperpolarized [1-13C]Pyruvate. *Sci Transl Med*. 2013;5(198):198ra108. doi:10.1126/scitranslmed.3006070

3. Tang S, Meng MV, Slater JB, Gordon JW, Vigneron DB, Stohr BA, et al. Metabolic imaging with hyperpolarized 13C pyruvate magnetic resonance imaging in patients with renal tumors—Initial experience. *Cancer*. 2021;127(15):2693-2704. doi:https://doi.org/10.1002/cncr.33554

4. Girgis H, Masui O, White NM, Scorilas A, Rotondo F, Seivwright A, et al. Lactate Dehydrogenase A is a potential prognostic marker in clear cell renal cell carcinoma. *Mol Cancer*. 2014;13:101. doi:10.1186/1476-4598-13-101

5. Sriram R, Gordon J, Baligand C, Ahamed F, Delos Santos J, Qin H, et al. Non-Invasive Assessment of Lactate Production and Compartmentalization in Renal Cell Carcinomas Using Hyperpolarized 13C Pyruvate MRI. *Cancers*. 2018;10(9). doi:10.3390/cancers10090313

6. Park JM, Spielman DM, Josan S, Jang T, Merchant M, Hurd RE, et al. Hyperpolarized 13C lactate-to-bicarbonate ratio as a biomarker for monitoring acute response of anti-VEGF treatment. *NMR Biomed*. 2016;29(5):650-659. doi:10.1002/nbm.3509

7. Bankson JA, Walker CM, Ramirez MS, Stefan W, Fuentes D, Merritt ME, et al. Kinetic modeling and constrained reconstruction of hyperpolarized [1-13C]-pyruvate offers improved metabolic imaging of tumors. *Cancer Res*. 2015;75(22):4708-4717. doi:10.1158/0008-5472.CAN-15-0171

8. Daniels CJ, Mclean MA, Schulte RF, Robb FJ, Gill AB, Mcglashan N, et al. A comparison of quantitative methods for clinical imaging with hyperpolarized 13C-pyruvate. *NMR Biomed*. 2016;29(4):387-399. doi:10.1002/nbm.3468

9. Larson PEZ, Chen HY, Gordon JW, Korn N, Maidens J, Arcak M, et al. Investigation of analysis methods for hyperpolarized 13C-pyruvate metabolic MRI in prostate cancer patients. *NMR Biomed*. 2018;31(11):1-17. doi:10.1002/nbm.3997

10. Mammoli D, Gordon J, Autry A, Larson PEZ, Li Y, Chen HY, et al. Kinetic Modeling of Hyperpolarized Carbon-13 Pyruvate Metabolism in the Human Brain. *IEEE Trans Med Imaging*. 2020;39(2):320-327. doi:10.1109/TMI.2019.2926437

11. Tang S, Bok R, Qin H, Reed G, VanCriekinge M, Delos Santos R, et al. A metabolite-specific 3D stack-of-spiral bSSFP sequence for improved lactate imaging in hyperpolarized [1- 13 C]pyruvate studies on a 3T clinical scanner. *Magn Reson Med*. 2020;84(3):1113-1125. doi:10.1002/mrm.28204

12. Liu X, Tang S, Mu C, Qin H, Cui D, Lai YC, et al. Development of specialized magnetic resonance acquisition techniques for human hyperpolarized [13C,15N2]urea + [1-13C]pyruvate simultaneous perfusion and metabolic imaging. *Magn Reson Med*. n/a(n/a). doi:10.1002/mrm.29266

13. Liu X, Tang S, Cui D, Bok RA, Chen HY, Gordon JW, et al. A metabolite specific 3D stack-of-spirals bSSFP sequence for improved bicarbonate imaging in hyperpolarized [1-13C]Pyruvate MRI. *J Magn Reson*. 2023;353:107518. doi:10.1016/j.jmr.2023.107518

14. Sahin S, Tang S, Vaidya M, Larson P. Fitting Kinetic Rate Constants in Metabolite-Specific bSSFP Hyperpolarized [1-13C]Pyruvate MRI. In: *Annual Meeting of ISMRM*. Virtual; 2021:2840.

15. Sahin S, Dwork N, Tang S, Liu X, Wang ZJ, Larson PEZ. Mapping Pyruvate-to-Lactate Rate Constants in Hyperpolarized Data with bSSFP Acquisitions. In: *Annual Meeting of ISMRM*. London, England; 2022:3571.

16. Sahin S, Liu X, Dwork N, Tang S, Wang ZJ, Larson PEZ. Estimating T2 relaxation rates of Lactate with Hyperpolarized C13 MRI using bSSFP and Pharmacokinetic Modelling. In: *Annual Meeting of ISMRM*. Toronto, ON; 2023:4325.

17. Bieri O, Scheffler K. Fundamentals of balanced steady state free precession MRI. *J Magn Reson Imaging*. 2013;38(1):2-11. doi:10.1002/jmri.24163

18. Hargreaves BA, Vasanawala SS, Pauly JM, Nishimura DG. Characterization and reduction of the transient response in steady-state MR imaging. *Magn Reson Med*. 2001;46(1):149-158. doi:10.1002/mrm.1170

19. Khegai O, Schulte RF, Janich MA, Menzel MI, Farrell E, Otto AM, et al. Apparent rate constant mapping using hyperpolarized [1–13C]pyruvate. *NMR Biomed*. 2014;27(10):1256-1265. doi:10.1002/nbm.3174

20. Gordon JW, Hansen RB, Shin PJ, Feng Y, Vigneron DB, Larson PEZ. 3D hyperpolarized C-13 EPI with calibrationless parallel imaging. *J Magn Reson*. 2018;289:92-99. doi:10.1016/j.jmr.2018.02.011

21. Zhu Z, Zhu X, Ohliger MA, Tang S, Cao P, Carvajal L, et al. Coil Combination Methods for Multi-Channel Hyperpolarized 13C Imaging Data from Human Studies. *J Magn Reson San Diego Calif 1997*. 2019;301:73-79. doi:10.1016/j.jmr.2019.01.015

22. Hyperpolarized-MRI-Toolbox. :Available at https://github.com/LarsonLab/hyperpolarized-mri-toolbox. doi:10.5281/zenodo.1198915

23. Larson PEZ, Tang S, Liu X, Sinha A, Dwork N, Sivalokanathan S, et al. Regional quantification of cardiac metabolism with hyperpolarized [1-13C]-pyruvate CMR evaluated in an oral glucose challenge. *J Cardiovasc Magn Reson*. 2023;25(1):77. doi:10.1186/s12968-023-00972-7

24. Scholz DJ, Otto AM, Hintermair J, Schilling F, Frank A, Köllisch U, et al. Parameterization of hyperpolarized (13)C-bicarbonate-dissolution dynamic nuclear polarization. *Magma N Y N*. 2015;28(6):591-598. doi:10.1007/s10334-015-0500-9

25. Reed GD, von Morze C, Bok R, Koelsch BL, Van Criekinge M, Smith KJ, et al. High Resolution 13C MRI With Hyperpolarized Urea: In Vivo T2 Mapping and 15N Labeling Effects. *IEEE Trans Med Imaging*. 2014;33(2):362-371. doi:10.1109/TMI.2013.2285120

26. Yen YF, Roux PL, Mayer D, King R, Spielman D, Tropp J, et al. T2 relaxation times of 13C metabolites in a rat hepatocellular carcinoma model measured in vivo using 13C-MRS of

hyperpolarized [1-13C]pyruvate. *NMR Biomed*. 2010;23(4):414-423. doi:10.1002/nbm.1481

27. Milshteyn E, Reed GD, Gordon JW, von Morze C, Cao P, Tang S, et al. Simultaneous T1 and T2 Mapping of Hyperpolarized 13C Compounds using the bSSFP Sequence. *J Magn Reson San Diego Calif 1997*. 2020;312:106691. doi:10.1016/j.jmr.2020.106691

28. Gordon JW, Autry AW, Tang S, Graham JY, Bok RA, Zhu X, et al. A variable resolution approach for improved acquisition of hyperpolarized 13 C metabolic MRI. *Magn Reson Med*. 2020;84(6):2943-2952. doi:10.1002/mrm.28421

29. Hu JY, Kim Y, Autry AW, Frost MM, Bok RA, Villanueva-Meyer JE, et al. Kinetic Analysis of Multi-Resolution Hyperpolarized 13C Human Brain MRI to Study Cerebral Metabolism. *Magn Reson Med*. 2022;88(5):2190-2197. doi:10.1002/mrm.29354

30. Leupold J, Månsson S, Stefan Petersson J, Hennig J, Wieben O. Fast multiecho balanced SSFP metabolite mapping of 1H and hyperpolarized 13C compounds. *Magn Reson Mater Phys Biol Med*. 2009;22(4):251-256. doi:10.1007/s10334-009-0169-z

31. Skinner JG, Topping GJ, Nagel L, Heid I, Hundshammer C, Grashei M, et al. Spectrally selective bSSFP using off-resonant RF excitations permits high spatiotemporal resolution 3D metabolic imaging of hyperpolarized [1-13 C]Pyruvate-to-[1-13 C]lactate conversion. *Magn Reson Med*. 2023;90(3):894-909. doi:10.1002/mrm.29676

32. Varma G, Wang X, Vinogradov E, Bhatt RS, Sukhatme VP, Seth P, et al. Selective spectroscopic imaging of hyperpolarized pyruvate and its metabolites using a single-echo

variable phase advance method in balanced SSFP. *Magn Reson Med*. 2016;76(4):1102-1115. doi:10.1002/mrm.26004

33. Chowdhury R, Mueller CA, Smith L, Gong F, Papoutsaki MV, Rogers H, et al. Quantification of Prostate Cancer Metabolism Using 3D Multiecho bSSFP and Hyperpolarized [1-13C] Pyruvate: Metabolism Differs Between Tumors of the Same Gleason Grade. *J Magn Reson Imaging*. 2023;57(6):1865-1875. doi:10.1002/jmri.28467

CHAPTER 5: SPATIALLY CONSTRAINED ESTIMATION OF HYPERPOLARIZED 13C MRI PHARMACOKINETIC RATE CONSTANT MAPS USING A U-NET

5.1 Abstract

Current methods for fitting rate constants, like k_{PL}, to Hyperpolarized [1-^{13}C]Pyruvate (HP C13) MRI data fit each voxel of the dataset using a least-squares objective based on the difference between the model and the data. Typically, each voxel is considered independently, and the spatial relationships are not considered during fitting.

In this work, we use a convolutional neural network, a U-Net, with convolutions across the spatial and temporal dimensions to estimate k_{PL} maps from dynamic HP C13 datasets. A framework for creating simulated anatomically accurate brain phantom data that also matches typical HP C13 characteristics is described to provide large amounts of data for training. The U-Net is initially trained with the simulated phantom data and then finetuned with in vivo datasets. In simulation, the U-net outperforms voxel-wise fitting with and without spatiotemporal denoising, particularly for low SNR data. However, on in vivo data before finetuning, the U-Net predicted k_{PL} maps appear oversmoothed. After finetuning with in vivo data, the resulting k_{PL} maps appear more realistic.

This study demonstrates how to use a U-Net to estimate rate constant maps for HP C13 data, including a comprehensive framework for generating realistic simulated data. It provides a foundation that can be built upon in the future for improved performance.

5.2 Introduction

Hyperpolarized [1-^{13}C]Pyruvate (HP C13) MRI is a powerful and robust minimally-invasive method to dynamically image metabolism within the body[1–3]. To fully leverage HP C13's power, acquired dynamic metabolite images must be translated to clinically relevant results. The metabolite dynamics can be modelled using pharmacokinetic (PK) modelling, where the apparent rate constants between metabolites, describe the rate of exchange. The pyruvate to lactate PK apparent rate constant, k_{PL}, has previously shown to be an important clinical biomarker to quantify metabolic reprogramming[3–5].

In previous work, PK models have been fit to the dynamics of each voxel to obtain k_{PL} maps[6–11]. With these methods, each voxel is considered independently of one another regardless of spatial proximity. However, spatial relationships are particularly relevant to consider when estimating k_{PL} maps from HP C13 MRI which can suffer from low SNR. With noisy data, spatial constraints may minimize anomalies during k_{PL} fitting and smooth k_{PL} maps.

Limited previous work has explored this challenge within the field of HP C13. Maidens et al.[12] proposed a spatio-temporally constrained PK model fitting using L2 and total variation regularizations. Their method resulted in improved appearance of in vivo parameter maps particularly in low SNR cases.

As an alternative to this optimization-based method, we propose a deep-learning method: to use a convolutional neural network, a U-Net, to estimate k_{PL} maps from dynamic HP C13 data. The convolutional layers will inherently spatially constrain the k_{PL} maps. Additionally, a deep

learning solution could speed up the k_{PL} quantification task compared to least-squares fitting or other iterative methods. In the field of DCE MRI, several others' have found promise in using convolutional neural networks to estimate pharmacokinetic parameters[13–17].

A challenge to training a U-Net to estimate k_{PL} maps is the limited number of HP C13 training data available and the lack of k_{PL} ground truths. As a solution, we propose to develop an anatomically accurate HP C13 brain phantom that matches typical HP C13 characteristics and use this synthetic phantom data for training. The pretrained model will then be further finetuned using in vivo HP C13 brain datasets to improve generalization to in vivo datasets. The objective of this work is to explore the feasibility of using a convolutional neural network to estimate PK parameter maps for HP C13 data.

5.3 Methods

5.3.1 Anatomical Phantom Data Creation

Segmented proton MR data from the BrainWeb[18–24] database from 19 different brains was used as a base of the anatomical phantom (**Figure 5.1**). For each brain, the segmented grey matter, white matter and vasculature masks were each assigned model parameters of k_{PL}, k_{PB}, k_{TRANS} and M_z0 values. These maps were down sampled, then, per voxel a single physical compartment pharmacokinetic model was used to generate dynamics (Eqs 5.1-5.3). The dynamic images were multiplied by coil sensitivity maps, Rician noise was added and then the dynamic images were up sampled to the output size. The data was simulated as a "multi-resolution" or "variable resolution" dataset[25] by varying the sample matrix size when generating the dynamics. The input

function was modeled as a gamma variate function where T_{bolus} was set to 8s and $T_{arrival}$ was varied between -4s and 4s.

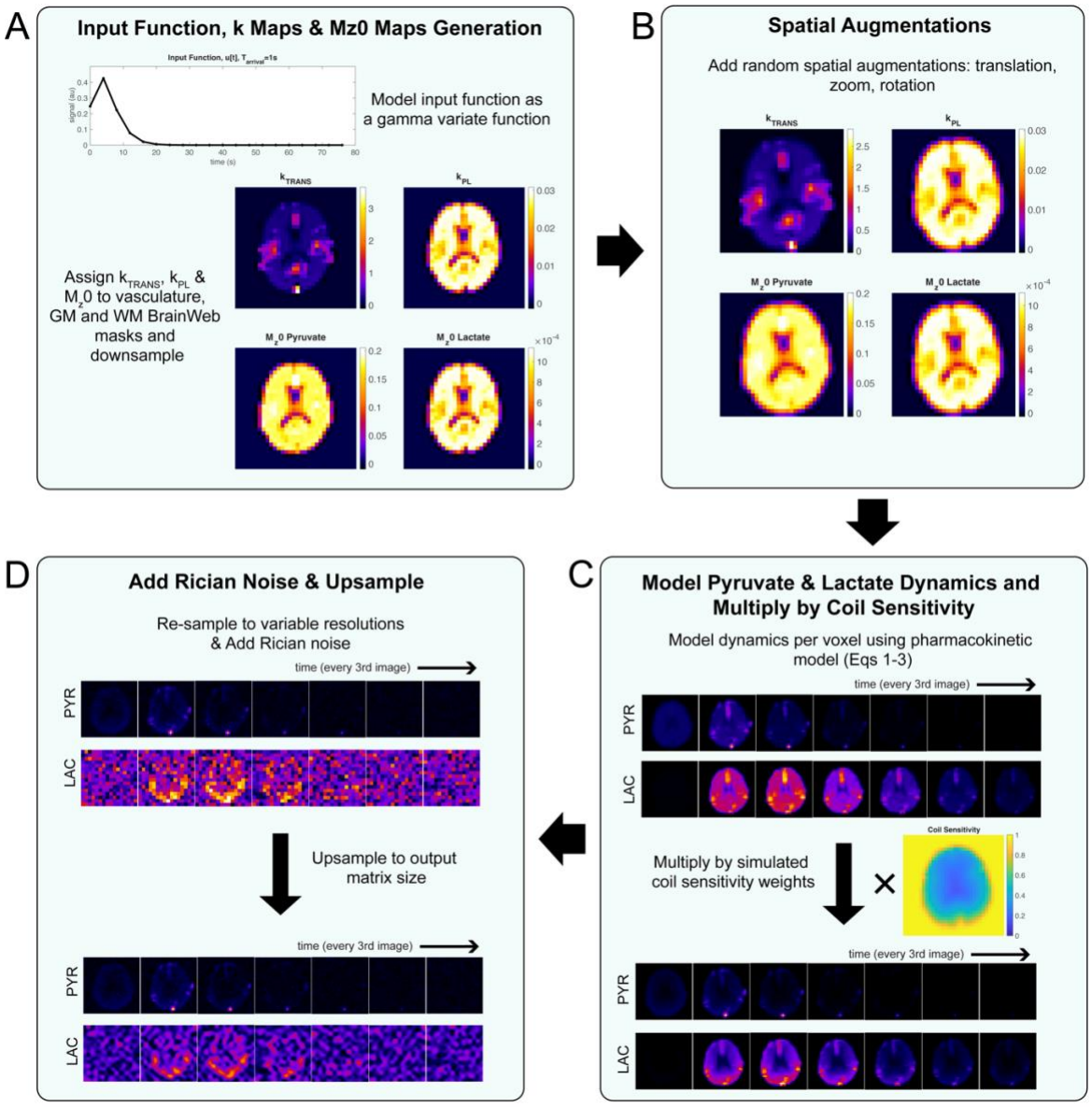

Figure 5.1: Overview of the creation of anatomical BrainWeb-based phantom datasets. Briefly, k_{TRANS}, k_{PL}, M_z0 maps are derived using BrainWeb masks (A). The maps are downsampled and randomly spatially altered (B). Dynamics of each voxel are then modeled using pharmacokinetic equations (Eqs 1-3, C). The dynamics are multiplied by coil sensitivity maps and noise is added to the dynamics (C,D).

The dynamics were modeled including the effect of RF excitation pulses using the sim_Nsite_model() function from the Hyperpolarized MRI Toolbox[6,26] which can be described with the following equations:

For $1 < t \leq N_t$:

$$M_z^+[t] = \exp(\mathbf{A} \cdot \mathrm{TR}) \left(M_z[t-1] + \begin{bmatrix} k_{TRANS} * u[t-1] \\ 0 \end{bmatrix} \right)$$

$$M_z[t] = \begin{bmatrix} P_z[t] \\ L_z[t] \end{bmatrix} = M_z^+[t] \begin{bmatrix} \cos \alpha_P \\ \cos \alpha_L \end{bmatrix} \quad 5.1$$

$$M_{xy}[t] = \begin{bmatrix} P_{xy}[t] \\ L_{xy}[t] \end{bmatrix} = M_z^+[t] \begin{bmatrix} \sin \alpha_P \\ \sin \alpha_L \end{bmatrix}$$

For $t = 1$:

$$M_z[t] = \begin{bmatrix} P_z[t] \\ L_z[t] \end{bmatrix} = M_{z,0} \begin{bmatrix} \cos \alpha_P \\ \cos \alpha_L \end{bmatrix} \quad 5.2$$

$$M_{xy}[t] = \begin{bmatrix} P_{xy}[t] \\ L_{xy}[t] \end{bmatrix} = M_{z,0} \begin{bmatrix} \sin \alpha_P \\ \sin \alpha_L \end{bmatrix}$$

where:

$$\mathbf{A} = \begin{bmatrix} -R_{1P} - k_{PL} & 0 \\ k_{PL} & -R_{1L} \end{bmatrix} \quad 5.3$$

In these equations, N_t is the number of time points, TR is the temporal resolution or time between subsequent pyruvate image acquisitions, u is the input function modeled as a gamma variate function and α_P and α_L are the flip angles for pyruvate and lactate, respectively, $M_{z,0}$ is the initial longitudinal magnetization of pyruvate and lactate. $M_{xy}[t]$ is used as the signal dynamics for each voxel of the anatomical brain phantom.

To create a diverse training, validation and test set, many parameters for the anatomical brain phantom were randomly varied. Parameter ranges were chosen based on previous literature[8,9,27–29] and in vivo data characteristics. The flip angles and temporal resolution were kept consistent and matched the in vivo data acquisition. For most of the parameters the random value was sampled from a normal distribution. The full set of parameters for the anatomical phantom used for training data can be found in **Table 5.1**. The final MATLAB function used to generate the anatomical brain phantom data is available in the Hyperpolarized MRI Toolbox[26].

Using the parameters and ranges from **Table 5.1**, a dataset of 500 was created with 8 slices each for a total of 4000 2D data examples. These were split into a training set of 3200, a validation set of 400 and a test set of 400 (referred to as the "simulated test set").

Table 5.1: Parameter values or ranges for various simulation parameters for the anatomical phantom data creation. (*= sampled from a uniform distribution, otherwise ranges are sampled from a normal distribution)

Parameter	Vasculature (Vasc)	Grey Matter (GM)	White Matter (WM)
k_{TRANS} low limit (s^{-1}) [min, max]	[1, 1]	[0.15, 0.25]	[GM $k_{TRANS,LOW}$-0.015, GM $k_{TRANS,LOW}$ -0.005]
k_{TRANS} upper limit (s^{-1}) [min, max]	[5, 11]	[0.35, 0.45]	[GM $k_{TRANS,HIGH}$-0.015, GM $k_{TRANS,HIGH}$ -0.005]
k_{PL} (s^{-1}) [min, max]	[0, 0]	[0.007, 0.035]	[GM k_{PL}-0.005, GM k_{PL}+0.005]
k_{PB} (s^{-1}) [min, max]	[0, 0]	[0.002, 0.007]	GM k_{PB}

	Pyruvate	Lactate	Bicarbonate
$M_{z,0}$ Scale [min, max]	Vasc: [1, 1] GM/WM: [0.5, 1]	Vasc: [0, 0] GM/WM: [0, 0.01]	Vasc: [0, 0] GM/WM: [0, 0.005]
Flip Angle (deg)	20	30	30
T_1 (s)	30	25	25
SNR [min, max]	[70, 320]	[15, 75]	[10, 35]
Sample Matrix Size [Nx, Ny, Nz]	[32, 32, 8]	[16, 16, 8]	[16, 16, 8]

	Value
Temporal Resolution (s)	**4**
$T_{arrival}$ (s) [min, max]	[-4, 4]
T_{bolus} (s)	8
Coil Sensity Dropoff Scale [min, max]	[0.2, 0.6]
Output Matrix Size [Nx, Ny, Nz]	[64, 64, 8]
X Translation (# voxels)* [min, max]	[-2, 2]
Y Translation (# voxels)* [min, max]	[-2, 2]
X Reflection*	True/False
Scale* [min, max]	[0.95, 1.2]
Rotation (deg)* [min, max]	[-5, 5]
Brain Index* [min, max]	[-5, 5]

Out of distribution (OOD) simulated datasets were created with the following parameters: high SNR: 350 and 90 for pyruvate and lactate, low SNR: 50 and 10 for pyruvate and lactate, high k_{PL}: 0.05, 0.051, 0 for grey matter, white matter and vasculature, low k_{PL}: 0.001, 0.002, 0 for grey matter, white matter and vasculature.

5.3.2 In Vivo Dataset

To test generalization to in vivo data and as training data for finetuning the model, a dataset of 21 healthy volunteer in vivo HP C13 brain images were used for validation[30–32]. All of these datasets were variable resolution acquisitions[25,28] where lactate was acquired at 2x coarser resolution than pyruvate. The data was acquired with a broadband EPI (bbEPI) sequence with a spectrally and spatially selective RF excitation. The flip angles used for acquisition were 20°, 30°, 30° for pyruvate, lactate and bicarbonate. Metabolite data was acquired dynamically for 20 time points with a temporal resolution of 3s. All datasets were acquired with a 24 channel RAPID Biomedical receive coil.

Briefly, EPI reconstruction was performed using MATLAB and the GE Orchestra Toolbox. Nyquist ghost artifact correction was performed, the data was prewhitened and coil combination was performed using the RefPeak method[33].

The in vivo dataset was split into finetuning (n=16) and test (n=5) 3D sets randomly. The finetuning dataset was further split so 12 2D slice images were used for validation and the remaining 116 images were used for training during finetuning.

5.3.3 U-Net Model & Training

A 2D Basic U-Net model[34] from MONAI[35] was used with feature layers of (32, 32, 64, 128, 256, 32). The input into the model was the simulated dynamics of pyruvate and lactate concatenated in the time dimension (**Figure 5.2**). The output was a single channel k_{PL} map. The model was trained for 1500 epochs and the weights that resulted in the lowest validation loss were used (epoch 106). A voxel-wise L1 loss was used and summed across the k_{PL} map. ADAM optimizer was used with a learning rate of 1e-3. For training and validation, the batch size was 2 and dropout probability was set to 0.3. The model was trained in Python with PyTorch and PyTorch Lightning. A Quadro RTX 8000 GPU was used to speed up training.

After initial training with the simulated data, the in vivo training and validation dataset was used for finetuning. During this finetuning experiment, all the layers of the network were updated. For finetuning, the learning rate was decreased to 1e-5 and was trained for 3000 epochs with model weights saved every 300 epochs.

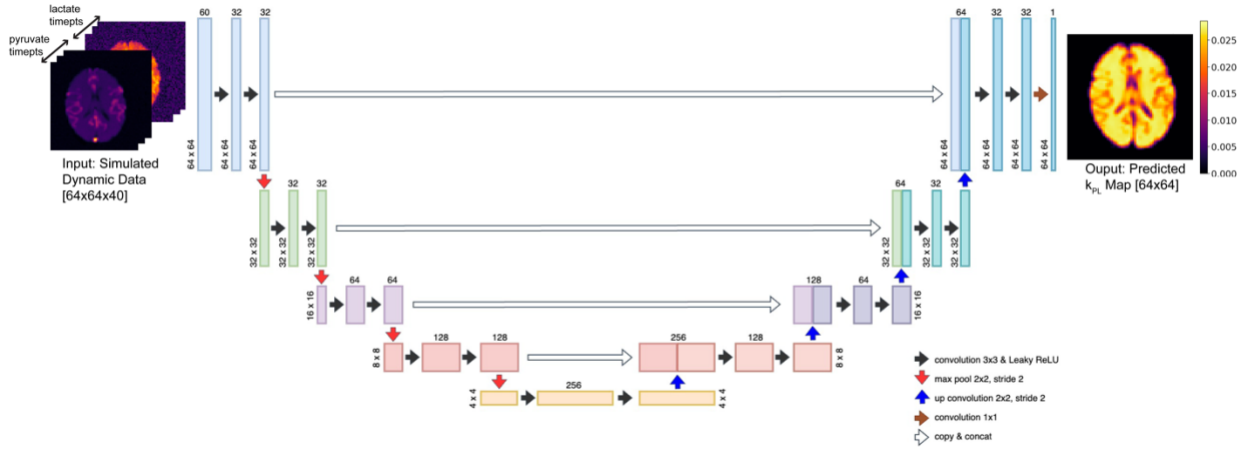

Figure 5.2: A graphical representation of the U-Net architecture used. This model is taken from MONAI's[35] Basic U-Net implementation which was inspired by Falk et al[34]. The dynamics are input into the model with pyruvate and lactate concatenated in the time dimension. The output is a single channel k_{PL} map.

5.3.4 Pharmacokinetic Modeling & Denoising

As comparisons to the U-Net results, pharmacokinetic fitting was performed with and without data denoising to obtain k_{PL} maps. The data was denoised using the global-local higher order SVD (GL-HOSVD) denoising method[36] with the following parameters: kglobal=0.4, klocal = 0.8, patchsize =5, step=2 and search window radius=11 as recommended in prior work[36]. The data with or without denoising was fit to k_{PL} maps using an inputless one physical compartment pharmacokinetic model[6,8,26]. For fitting, initial k_{PL} = 0.02, initial k_{PB} = 0.005, pyruvate T_1=30s, lactate T_1=25s, bicarbonate T_1=25s. Pharmacokinetic model-derived k_{PL} maps were masked with a brain mask. For simulated data, the k_{PL} map was thresholded to derive a brain mask. For in vivo data, the lactate SNR was thresholded to obtain a brain mask.

As another comparison to the U-Net results, a spatio-temporally constrained modeling technique proposed by Maidens et al.[12] was used to derive k_{PL} maps. The parameters used were pyruvate T_1=30s, lactate T_1=25s, ρ = 1e4, λ_{TV} = 20 and λ_{l2} = 500. The ρ and λ values were chosen such that the model converged in less than 100 iterations and the resulting k_{PL} values were similar to the inputless pharmacokinetic model. The spatio-temporally constrained model maps were only compared with in vivo data maps as a new set of parameters would have to be chosen for simulated datasets.

5.4 Results

5.4.1 Simulated Anatomical Brain Phantom Data

Examples from the simulated brain phantom data are shown in **Figure 5.3**. The simulated data examples resemble in vivo datasets. The sagittal sinus signal dominates the pyruvate signal. The

typical signal drop-off in the center of the brain is also modeled using the simulated coil sensitivity maps. The third simulated example depicting slice 2 is less similar to in vivo examples as the pyruvate maps have high signal regions outside of the sagittal sinus. Additionally, in the simulated examples, pyruvate signal is higher for more time points whereas in the in vivo examples the signal decays faster. The reverse is true for lactate. In the simulated examples lactate decays faster than the in vivo examples.

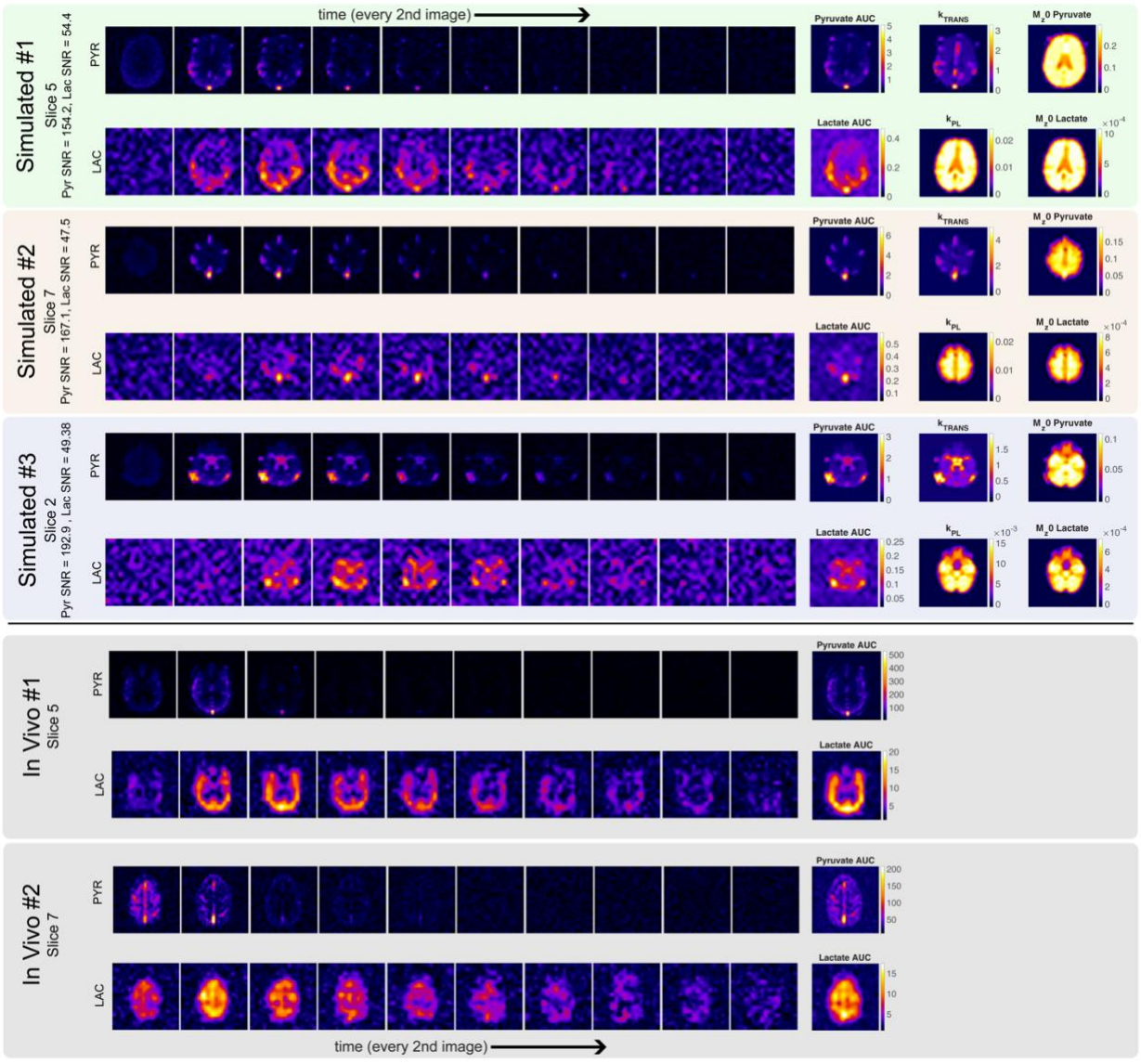

Figure 5.3: Three examples of simulated anatomical brain phantom datasets and two examples of in vivo datasets. Each example is a different dataset and a different image slice (5, 7 and 2, top to bottom). On the left are the dynamics of pyruvate (Figure caption continued on the next page.)

(Figure caption continued from the previous page.) (PYR) and lactate (LAC) and on the right is pyruvate & lactate AUC, k_{PL}, k_{TRANS}, pyruvate & lactate M_z0 maps.

5.4.2 Base U-Net

A 2D U-Net was trained with the simulated anatomical brain phantom data. The validation loss reached a minimum at epoch 106. **Figure 5.4** shows examples of U-Net predicted k_{PL} maps on the simulated test set. These are compared with using pharmacokinetic model fitting and using pharmacokinetic model fitting after HOSVD denoising.

The U-Net predicted results were more robust to added noise compared with the PK model results even with HOSVD denoising (**Figure 5.4**). The U-Net inherently ignores low SNR regions outside the brain, whereas the PK model maps had to be manually thresholded. Using denoised data for the PK model only resulted in small improvements to using raw data as input into the model. Comparing these methods quantitatively, the U-Net predictions performed better on the simulated test data (**Table 5.2**).

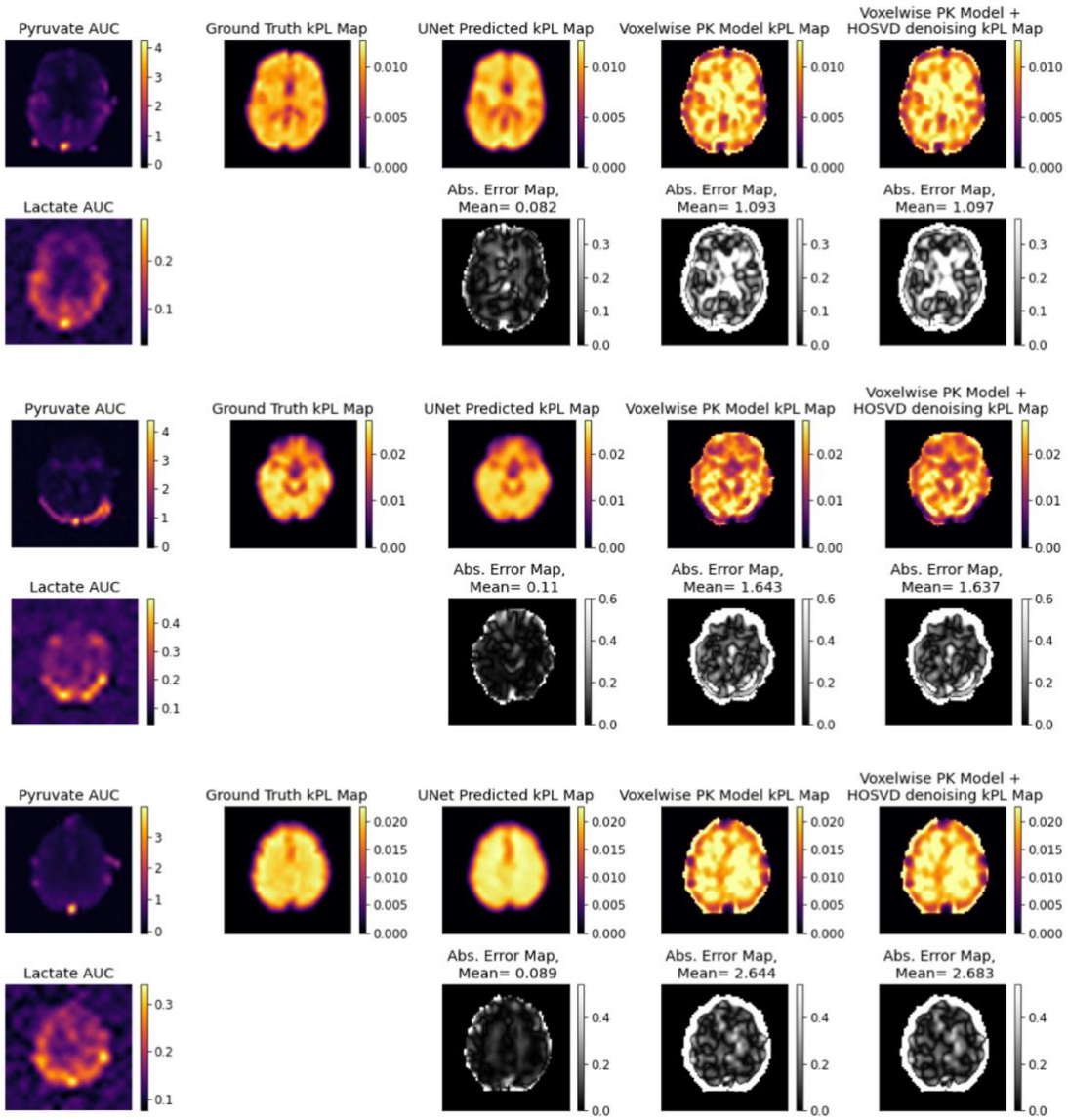

Figure 5.4: U-Net k_{PL} map predictions for three examples of slices from the simulated test set. The U-Net predictions are compared to using a Voxelwise PK model without denoising data and a Voxelwise PK model with HOSVD denoised data. Error maps for each k_{PL} map estimation method are below. The PK model maps are thresholded.

Table 5.2: Simulated Test Metrics for U-Net, PK Model and PK Model with HOSVD denoising.

Metrics	U-Net Prediction	Voxelwise PK Model	HOSVD Denoising + Voxelwise PK Model
Sum of Abs Error	0.164	3.178	3.217
Sum of Sq Error	0.00003	0.049	0.051
Avg SSIM	0.905	0.352	0.357

The U-Net model was tested further with out of distribution (OOD) simulated data examples, where the datasets were created with SNR or k_{PL} values outside of the training range (**Figure 5.5**). In the low SNR case, the U-Net performed significantly better than PK modeling, but still suffered in recreating the ground truth k_{PL} map, specifically in the locations of the ventricles. In the high SNR case, the U-Net predicted maps performed better than the PK model. For both low k_{PL} and high k_{PL}, the U-Net either overestimated or underestimated the k_{PL}, resulting in large bias in the k_{PL} map.

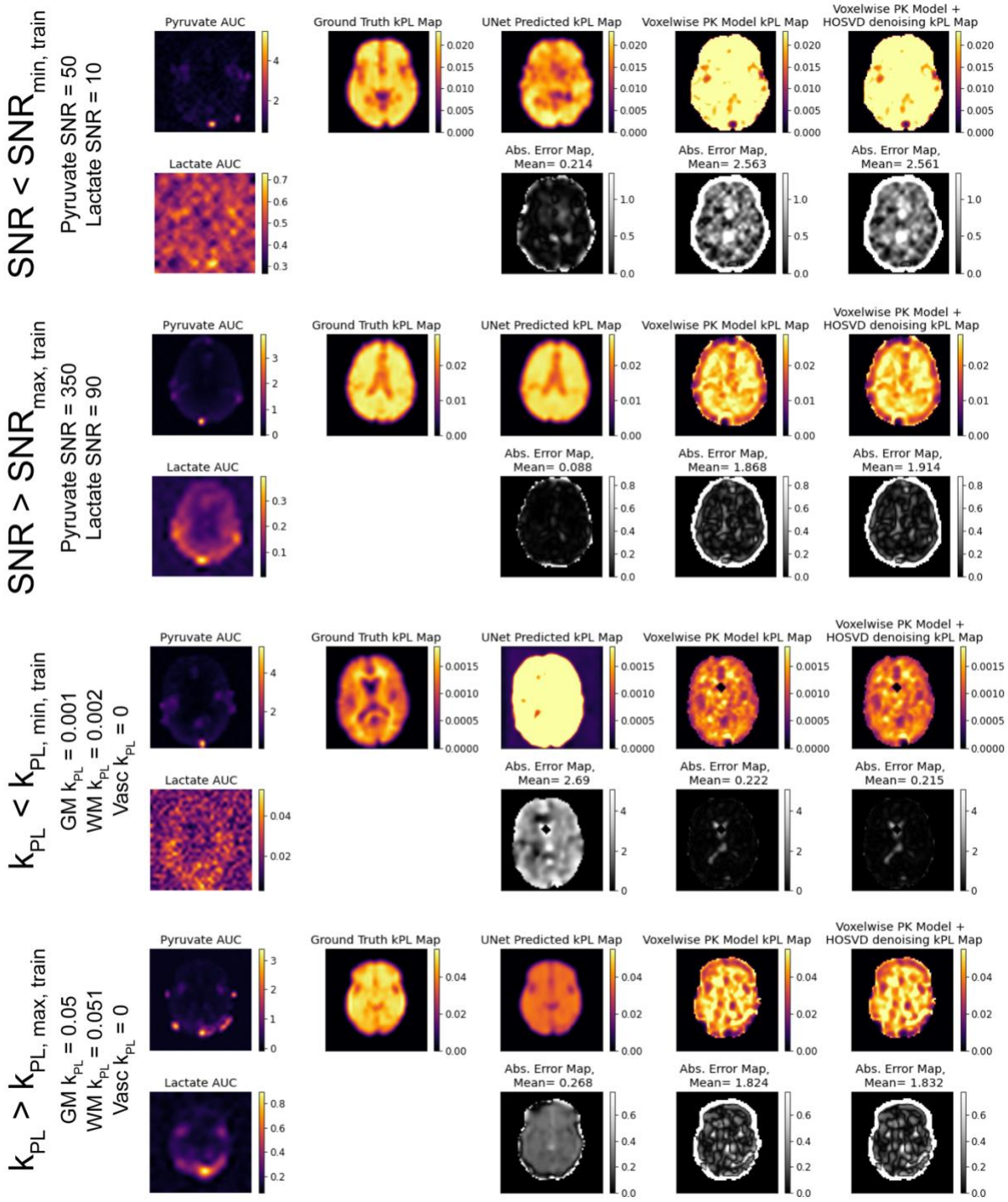

Figure 5.5: U-Net and PK model k_{PL} map estimations shown for four out of distribution cases. The data had either k_{PL} values or SNR above or below the training data. The PK model maps are thresholded.

The U-Net's performance was next tested with in vivo data (**Figure 5.6**). The U-Net predicted k_{PL} maps were compared with the PK model derived k_{PL}. Similar to the simulated test data, the U-Net successfully SNR thresholded the resulting k_{PL} maps, ignoring regions outside the brain with no signal. The U-Net predicted maps were more uniform in k_{PL} value compared to the voxelwise PK model and spatio-temporally constrained results. Quantitatively, the U-Net predicted maps reflected k_{PL} values within the same range as the PK model maps.

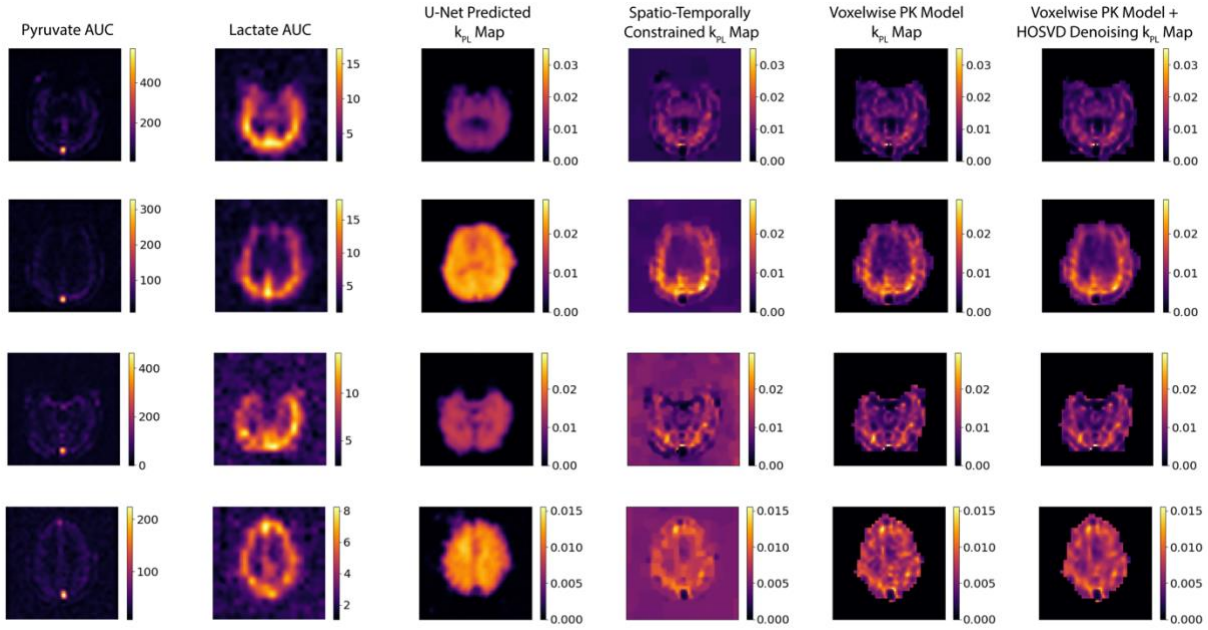

Figure 5.6: Five examples of the U-Net's performance on the in vivo test set. For each example, the U-Net predicted k_{PL} map is compared with the PK model estimated maps with or without HOSVD denoising and spatio-temporally constrained maps. The voxelwise PK model maps are manually SNR thresholded whereas the U-Net internally SNR thresholds the estimated k_{PL} maps. The spatio-temporally constrained maps are also not thersholded.

5.4.3 Finetuning

To improve generalization of the model to the in vivo dataset. All of the layers of the previously simulated data-trained U-Net were finetuned with more training steps using the in vivo dataset with PK model derived k_{PL} maps as the ground truth. To investigate the effect of finetuning, the U-Net predicted k_{PL} maps were compared before finetuning and after finetuning for 300, 1200

and 3000 epochs (**Figure 5.7**). As finetuning proceeded, the U-Net predictions gained more similarities to the voxelwise PK model and spatio-temporally constrained k_{PL} maps, and similar regions had the same k_{PL} values. Compared with the results prior to finetuning, the U-Net predictions no longer fully SNR threshold and fit a k_{PL} values greater than 0 to the background.

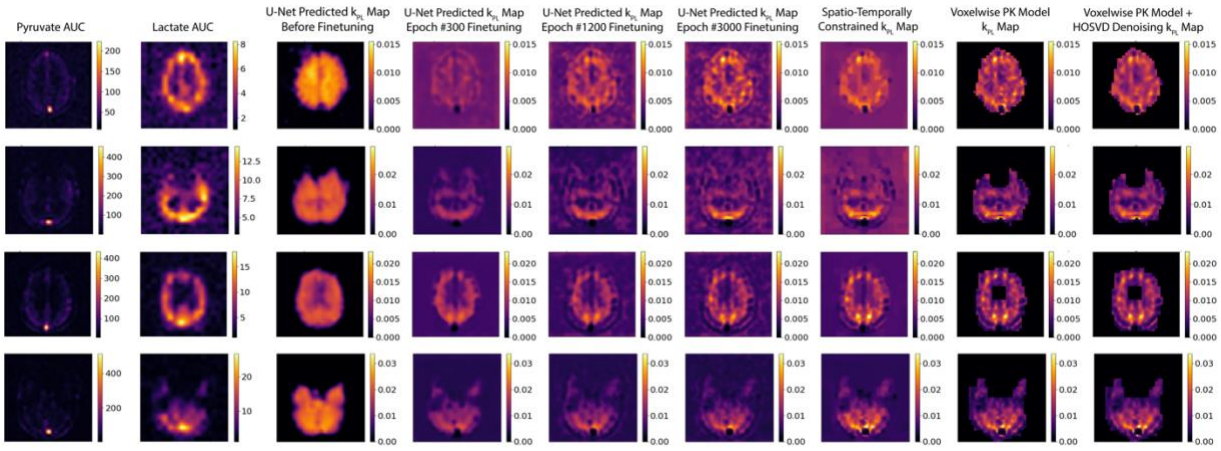

Figure 5.7: U-Net predicted k_{PL} maps for five images from the in vivo test set before finetuning and after 300, 1200 and 3000 epochs of finetuning. The voxelwise PK model maps are SNR thresholded.

5.5 Discussion

To our knowledge, we are the first group to estimate k_{PL} maps for HP C13 data using a U-Net. One of the biggest disadvantages of the most common least-squares based PK models to estimate k_{PL} is evaluating each voxel independently rather than taking advantage of the relationships between voxels. Convolutional layers within the U-Net naturally spatially constrain and can improve k_{PL} estimation for noisy HP 13C data. Additionally, at inference time the U-Net estimates a full k_{PL} map in less than a second which is a large time improvement compared with iterative, least-squares methods.

In this work, to overcome the limited HP C13 data available for supervised learning, an anatomically accurate HP brain phantom was developed. Using simulated phantom data for

training, a base U-Net was trained. Although this U-Net performed well on the simulated test data (**Figure 5.4**, **Table 5.2**), it resulted in over-smoothed k_{PL} maps in the in vivo datasets (**Figure 5.6**). To improve performance on in vivo data, the model was finetuned using a limited in vivo dataset. The finetuned models performed more similarly to the PK model while also minimizing, potentially erroneous, deviations in k_{PL} when using the PK model (**Figure 5.7**). The level of finetuning (number of epochs for a given learning rate) must be optimized in future work to obtain the correct tradeoff between spatial blurring and k_{PL} accuracy.

5.5.1 Anatomical Phantom Limitations

The anatomical phantom developed and used for training data of the U-Net is a good approximation of in vivo data, yet it makes some assumptions and has limitations.
During simulated data generation, the k_{PL} values for WM were chosen based on k_{PL} of GM (**Table 5.1**) which resulted in low contrast between WM and GM. This may have contributed to the over-smoothing seen in the in vivo maps when using the base U-Net. In future work, the WM and GM k_{PL} should be chosen independently.

Another limitation of the phantom was that the simulated coil sensitivity maps were simple and didn't include much variation across subjects. The input function, including arrival time were kept constant across the brain and resulted in dynamics that are somewhat varied from in vivo data (**Figure 5.3**). Additionally, a single physical compartment PK model is used to simulate the dynamics whereas more complicated models may be more reflective of the biochemistry. This framework could easily be adapted for other PK models when generating the dynamics.

5.5.2 Matrix Size & Resampling

An important consideration in this work is resampling. The anatomical phantom data during generation is resampled in multiple steps during the process. Since the in vivo data is multi-resolution, the coarser resolution lactate must be resampled to match the matrix size of pyruvate. In some of the error maps (**Figure 5.4**, **5.5**), a pattern is visible which may be attributed to resampling operations.

5.5.3 Extensions & Future Work

This work was specifically concerned with estimating k_{PL} maps using a U-Net. However, the same pipeline be extended to estimating other rate constant maps of interest, such as k_{PB} or k_{PA}. To estimate more than one rate constant map using the U-Net, one could output multiple channels from the U-Net and calculate a multi-channel loss.

The low lactate SNR example (**Figure 5.5**) may reflect the U-Net's performance in estimating k_{PB} or k_{PA} as bicarbonate and alanine typically have lower SNR than lactate.

The in vivo dataset used here was uniform and had the same acquisition parameters using the same scanner. The question remains as to how well the U-Net would generalize to external HP C13 cases, specifically those with different acquisition parameters such as flip angles. We did not explore whether full training would need to be repeated or just the finetuning when implementing this framework for a completely new dataset.

To overcome the limited number of HP C13 datasets, the simulated anatomical brain phantom data was used for training. A different and perhaps more direct workaround to this challenge

could instead be considering unsupervised deep learning methods. Taking inspiration from DCE parameter estimation, Oh et al.[17] and Ottens et al.[14] both used unpaired methods with a physics-informed loss. This could be readily applied to HP C13 data to overcome the lack of paired data.

Other neural network architectures may also be considered. Again in the field of DCE MRI, there has been promising work using recurrent neural networks (GRU, LSTM)[14] or attention-based[37] networks for PK parameter estimation which could be explored in addition to convolution-only networks.

5.6 Conclusion

In this work, we have provided a demonstration of convolutional neural networks to estimate k_{PL} maps as well as a framework to generate anatomically accurate dynamic brain HP C13 datasets. The simulated anatomical phantom data resembled in vivo data and constituted a diverse training dataset. In simulation, the U-net outperforms voxel-wise fitting with and without spatiotemporal denoising, particularly for low SNR data. The base U-Net trained with the simulated data resulted in over-smoothed appearing k_{PL} maps for in vivo datasets. After finetuning the U-Net, the U-Net predicted parameter maps more similar to PK model derived maps. The U-Net showed advantages over using a PK model in low SNR datasets. Further exploration of using neural networks to estimate k_{PL} for HP C13 datasets is valuable and feasible.

5.6 References

1. Kurhanewicz J, Vigneron DB, Ardenkjaer-Larsen JH, Bankson JA, Brindle K, Cunningham CH, et al. Hyperpolarized 13C MRI: Path to Clinical Translation in Oncology. *Neoplasia*. 2019;21(1):1-16. doi:10.1016/j.neo.2018.09.006

2. Wang ZJ, Ohliger MA, Larson PEZ, Gordon JW, Bok RA, Slater J, et al. Hyperpolarized 13C MRI: State of the Art and Future Directions. *Radiology*. 2019;291(2):273-284. doi:10.1148/radiol.2019182391

3. Nelson S, Kurhanewicz J, Vigneron D, Larson P, Harzstark A, Ferrone M, et al. Metabolic Imaging of Patients with Prostate Cancer Using Hyperpolarized [1-13C]Pyruvate. *Sci Transl Med*. 2013;5(198):198ra108. doi:10.1126/scitranslmed.3006070

4. Larson PEZ, Tang S, Liu X, Sinha A, Dwork N, Sivalokanathan S, et al. Regional quantification of cardiac metabolism with hyperpolarized [1-13C]-pyruvate CMR evaluated in an oral glucose challenge. *J Cardiovasc Magn Reson*. 2023;25(1):77. doi:10.1186/s12968-023-00972-7

5. Ursprung S, Woitek R, McLean MA, Priest AN, Crispin-Ortuzar M, Brodie CR, et al. Hyperpolarized 13C-Pyruvate Metabolism as a Surrogate for Tumor Grade and Poor Outcome in Renal Cell Carcinoma—A Proof of Principle Study. *Cancers*. 2022;14(2):335. doi:10.3390/cancers14020335

6. Larson PEZ, Chen HY, Gordon JW, Korn N, Maidens J, Arcak M, et al. Investigation of analysis methods for hyperpolarized 13C-pyruvate metabolic MRI in prostate cancer patients. *NMR Biomed*. 2018;31(11):1-17. doi:10.1002/nbm.3997

7. Sahin S, Garnæs MF, Bennett A, Dwork N, Tang S, Liu X, et al. A pharmacokinetic model for hyperpolarized C-pyruvate MRI when using metabolite-specific bSSFP sequences. *Magn Reson Med*. 2024;92(4):1698-1713. doi:10.1002/mrm.30142

8. Mammoli D, Gordon J, Autry A, Larson PEZ, Li Y, Chen HY, et al. Kinetic Modeling of Hyperpolarized Carbon-13 Pyruvate Metabolism in the Human Brain. *IEEE Trans Med Imaging*. 2020;39(2):320-327. doi:10.1109/TMI.2019.2926437

9. Kazan SM, Reynolds S, Kennerley A, Wholey E, Bluff JE, Berwick J, et al. Kinetic modeling of hyperpolarized 13C pyruvate metabolism in tumors using a measured arterial input function. *Magn Reson Med*. 2013;70(4):943-953. doi:10.1002/mrm.24546

10. Bankson JA, Walker CM, Ramirez MS, Stefan W, Fuentes D, Merritt ME, et al. Kinetic modeling and constrained reconstruction of hyperpolarized [1-13C]-pyruvate offers improved metabolic imaging of tumors. *Cancer Res*. 2015;75(22):4708-4717. doi:10.1158/0008-5472.CAN-15-0171

11. Khegai O, Schulte RF, Janich MA, Menzel MI, Farrell E, Otto AM, et al. Apparent rate constant mapping using hyperpolarized [1–13C]pyruvate. *NMR Biomed*. 2014;27(10):1256-1265. doi:10.1002/nbm.3174

12. Maidens J, Gordon JW, Chen HY, Park I, Van Criekinge M, Milshteyn E, et al. Spatio-Temporally Constrained Reconstruction for Hyperpolarized Carbon-13 MRI Using Kinetic Models. *IEEE Trans Med Imaging*. 2018;37(12):2603-2612. doi:10.1109/TMI.2018.2844246

13. Fang K, Wang Z, Li Z, Wang B, Han G, Cheng Z, et al. Convolutional neural network for accelerating the computation of the extended Tofts model in dynamic contrast-enhanced magnetic resonance imaging. *J Magn Reson Imaging*. 2021;53(6):1898-1910. doi:10.1002/jmri.27495

14. Ottens T, Barbieri S, Orton MR, Klaassen R, van Laarhoven HWM, Crezee H, et al. Deep learning DCE-MRI parameter estimation: Application in pancreatic cancer. *Med Image Anal*. 2022;80:102512. doi:10.1016/j.media.2022.102512

15. Arledge CA, Sankepalle DM, Crowe WN, Liu Y, Wang L, Zhao D. Deep learning quantification of vascular pharmacokinetic parameters in mouse brain tumor models. *Front Biosci-Landmark*. 2022;27(3):99. doi:10.31083/j.fbl2703099

16. Ulas C, Das D, Thrippleton MJ, Valdés Hernández M del C, Armitage PA, Makin SD, et al. Convolutional Neural Networks for Direct Inference of Pharmacokinetic Parameters: Application to Stroke Dynamic Contrast-Enhanced MRI. *Front Neurol*. 2019;9. doi:10.3389/fneur.2018.01147

17. Oh G, Moon Y, Moon WJ, Ye JC. Unpaired deep learning for pharmacokinetic parameter estimation from dynamic contrast-enhanced MRI without AIF measurements. *NeuroImage*. 2024;291:120571. doi:10.1016/j.neuroimage.2024.120571

18. Aubert-Broche B, Evans AC, Collins L. A new improved version of the realistic digital brain phantom. *NeuroImage*. 2006;32(1):138-145. doi:10.1016/j.neuroimage.2006.03.052

19. Aubert-Broche B, Griffin M, Pike GB, Evans AC, Collins DL. Twenty new digital brain phantoms for creation of validation image data bases. *IEEE Trans Med Imaging*. 2006;25(11):1410-1416. doi:10.1109/TMI.2006.883453

20. Cocosco C, Kollokian V, Kwan RK, Evans AC. BrainWeb: Online Interface to a 3D MRI Simulated Brain Database. *NeuroImage*. 1997. https://www.semanticscholar.org/paper/BrainWeb%3A-Online-Interface-to-a-3D-MRI-Simulated-Cocosco-Kollokian/2bb7426e6ecdab0f120c89f6a324cf0c2a7266d4. Accessed April 17, 2024.

21. Collins DL, Zijdenbos AP, Kollokian V, Sled JG, Kabani NJ, Holmes CJ, et al. Design and construction of a realistic digital brain phantom. *IEEE Trans Med Imaging*. 1998;17(3):463-468. doi:10.1109/42.712135

22. Kwan RK, Evans AC, Pike GB. MRI simulation-based evaluation of image-processing and classification methods. *IEEE Trans Med Imaging*. 1999;18(11):1085-1097. doi:10.1109/42.816072

23. Kwan RKS, Evans AC, Pike GB. An Extensible MRI Simulator for Post-Processing Evaluation. In: *Proceedings of the 4th International Conference on Visualization in Biomedical Computing*. VBC ’96. Berlin, Heidelberg: Springer-Verlag; 1996:135-140.

24. BrainWeb: Simulated Brain Database. https://brainweb.bic.mni.mcgill.ca/brainweb/. Accessed April 17, 2024.

25. Hyperpolarized-MRI-Toolbox. :Available at https://github.com/LarsonLab/hyperpolarized-mri-toolbox. doi:10.5281/zenodo.1198915

26. Autry AW, Vaziri S, Gordon JW, Chen HY, Kim Y, Dang D, et al. Advanced Hyperpolarized 13C Metabolic Imaging Protocol for Patients with Gliomas: A Comprehensive Multimodal MRI Approach. *Cancers*. 2024;16(2):354. doi:10.3390/cancers16020354

27. Hu JY, Kim Y, Autry AW, Frost MM, Bok RA, Villanueva-Meyer JE, et al. Kinetic Analysis of Multi-Resolution Hyperpolarized 13C Human Brain MRI to Study Cerebral Metabolism. *Magn Reson Med*. 2022;88(5):2190-2197. doi:10.1002/mrm.29354

28. Bøgh N, Gordon JW, Hansen ESS, Bok RA, Blicher JU, Hu JY, et al. Initial Experience on Hyperpolarized [1-13C]Pyruvate MRI Multicenter Reproducibility—Are Multicenter Trials Feasible? *Tomography*. 2022;8(2):585-595. doi:10.3390/tomography8020048

29. Gordon JW, Chen HY, Dwork N, Tang S, Larson PEZ. Fast Imaging for Hyperpolarized MR Metabolic Imaging. *J Magn Reson Imaging*. 2021;53(3):686-702. doi:https://doi.org/10.1002/jmri.27070

30. Gordon JW, Chen H, Autry A, Park I, Van Criekinge M, Mammoli D, et al. Translation of Carbon-13 EPI for hyperpolarized MR molecular imaging of prostate and brain cancer patients. *Magn Reson Med*. 2018;81(4):2702-2709. doi:10.1002/mrm.27549

31. Crane JC, Gordon JW, Chen HY, Autry AW, Li Y, Olson MP, et al. Hyperpolarized 13C MRI data acquisition and analysis in prostate and brain at University of California, San Francisco. *NMR Biomed*. 2021;34(5):e4280. doi:https://doi.org/10.1002/nbm.4280

32. Gordon JW, Autry AW, Tang S, Graham JY, Bok RA, Zhu X, et al. A variable resolution approach for improved acquisition of hyperpolarized 13 C metabolic MRI. *Magn Reson Med*. 2020;84(6):2943-2952. doi:10.1002/mrm.28421

33. Zhu Z, Zhu X, Ohliger MA, Tang S, Cao P, Carvajal L, et al. Coil Combination Methods for Multi-Channel Hyperpolarized 13C Imaging Data from Human Studies. *J Magn Reson San Diego Calif 1997*. 2019;301:73-79. doi:10.1016/j.jmr.2019.01.015

34. Falk T, Mai D, Bensch R, Çiçek Ö, Abdulkadir A, Marrakchi Y, et al. U-Net: deep learning for cell counting, detection, and morphometry. *Nat Methods*. 2019;16(1):67-70. doi:10.1038/s41592-018-0261-2

35. MONAI. https://monai.io/. Accessed July 22, 2024.

36. Kim Y, Chen HY, Autry AW, Villanueva-Meyer J, Chang SM, Li Y, et al. Denoising of hyperpolarized 13 C MR images of the human brain using patch-based higher-order singular value decomposition. *Magn Reson Med*. 2021;86(5):2497-2511. doi:10.1002/mrm.28887

37. Zeng, Qingyuan, Zhou, Wu. An Attention Based Deep Learning Model for Direct Estimation of Pharmacokinetic Maps from DCE-MRI Images | IEEE Conference Publication | IEEE Xplore. In: ; 2021. Accessed July 22, 2024.

CHAPTER 6: CURATION OF A MULTI-PHASE RENAL CELL CARCINOMA CT DATASET WITH TUMOR SEGMENTATIONS

6.1 Abstract

To optimize treatment planning for patients with renal tumors, assessing the pathology of the tumor and the tumor grade is imperative. Current standard of care imaging practices cannot reliably differentiate among certain renal tumors such as benign oncocytoma and clear cell renal cell carcinoma (RCC), and between low and high grade RCCs.

Previous work has explored using deep learning, radiomics, and texture analysis to predict renal tumor subtypes and differentiate between low and high grade RCCs with mixed success. All studies have struggled with access to a large diverse dataset. Access to more datasets with a diverse representation of institutions and patient populations will improve deep learning model performance.

In this work, a dataset of 500+ multiphase 3D CT exams was curated. Each contained at least one contrast-enhanced CT phase (arterial, portal venous and delay) that was registered in space to the unenhanced pre-contrast CT. Tumor outlines or bounding boxes were annotated and registered to the image volumes. The pathology results for each tumor are included as well as relevant patient metadata.

6.2 Introduction

Accurate pathology grade and characterization of renal masses is crucial for proper treatment planning. CT imaging is the gold standard and most common imaging for renal tumor diagnosis

and staging. These CT exams usually consist of an unenhanced pre-contrast CT scan, and one or more post-contrast phases with varied delay times after contrast administration. However, even with contrast-enhanced CT, it is difficult to reliably differentiate malignant renal masses from benign renal masses[1–5]. The most common malignant renal masses are renal cell carcinomas (RCCs), which are further characterized as clear cell (ccRCC), papillary (pRCC) and chromophobe (chRCC) subtypes. The most common type of benign renal masses are oncocytomas and angiomyolipomas (AMLs). Oncocytomas and lipid-poor AMLs are particularly difficult to distinguish from RCCs using CT[1–5]. It is similarly challenging to differentiate between the subtypes of RCCs with contrast-enhanced CT[1,2,6].

Another important consideration for treatment planning is the differentiation between low-grade and high-grade RCC cases. Low-grade RCCs may benefit from active surveillance to avoid overtreatment and poor outcomes post surgery[7]. The current gold standard for tumor grading prior to surgery uses an invasive procedure called percutaneous biopsy which may underestimate tumor grade, and has been reported to have a diagnosis failure rate of 20 percent[8,9].

Previously, researchers have explored deep learning[10–17] and radiomics with texture analysis[18–21] to differentiate pathologies or pathology grades using unenhanced or contrast enhanced CT. Uhm et al.[13] presents an end-to-end segmentation and classification neural network pipeline to classify multiphase CT images as AML, oncocytoma, ccRCC, chRCC, or pRCC. They report that the network performed better at classifying chRCC, AML and oncocytoma correctly than radiologists who misclassified as ccRCC. Coy et al.[10] leveraged transfer learning to classify ccRCC vs oncocytoma on multiphase CT datasets and achieved the highest accuracy of 75%

using the excretory phase. Lin et al. predicted low vs high grade of ccRCC cases using ResNet for multiphase CT and reported 73-77% accuracy. A meta-analysis of 11 studies by Yu et al.[18] using CT texture analysis to differentiate low-grade vs high-grade RCC notes an ROC-AUC of 0.88 suggesting strong diagnostic power.

Of these previous studies, most studies had datasets smaller than 500 renal tumor cases and most training sets have been acquired at a single institution. Larger datasets from a diverse set of institutions could improve the results of these techniques and improve the model's generalization to new data during inference.

Other publicly available multiphase renal tumor CT datasets are limited in the number of patient cases. The TCGA-KIRC[22] (n=267), TCGA-KIRP[23] (n=33), TCGA-KICH[24] (n=15) datasets include ccRCC, pRCC, and chRCC CT datasets, respectively, hosted on the Cancer Imaging Archive (TCIA)[25]. The 2023 Kidney and Kidney Tumor Segmentation challenge (KiTS)[26] hosted by MICCAI also offers a publicly available dataset with a total of 599 cases combined from the 2021 and 2023 challenge (489 training, 110 test) including ccRCC, chRCC, AML, oncocytoma, and unclassified RCC. However, this data only includes a single CT phase, either corticomedullary or nephrogenic, making it unsuitable for multi-phase approaches.

In this work, we provide and describe a 3D multiphase renal mass CT dataset with tumor masks gathered from over 15 years of data from UCSF. The data inclusion and exclusion criteria, and curation steps, are described along with suggestions of further additions to this dataset.

6.3 Methods

6.3.1 DICOM Retrieval & Inclusion Criteria

For the time range between 2002-2018, the UCSF pathology database was searched for renal masses ≤7cm (T1 stage). The exams were included only if they patient had a preoperative CT which included an unenhanced pre-contrast scan and at least one post-contrast scan. The DICOM images were imported from UCSF PACS, and the images headers were anonymized and deidentified.

6.3.2 Conversion to NifTI

DICOM data was converted to Neuroimaging Informatics Technology Initiative (NifTI) file format for easy volume manipulation using the dicom2nifti Python package. Of the full dataset, 172 images could not be converted into volumes as multiple phases were stacked on top of each other. For these cases, the individual DICOMs corresponding to each phase were separated into folders before converting to NifTI. The Python package Nibabel was used to load, save and manipulate NifTI data.

6.3.3 Tumor Segmentations & Phase Labeling

Renal lesions were identified and segmented by an experienced Radiology resident on MD.ai. During this segmentation, the resident also labeled the phase of the post-contrast images as arterial, portal-venous or delay.

Using MD.ai, for each labelled phase scan, one of three types of tumor annotations were used: (1) Polygonal tumor annotation defined by vertices, (2) Bounding box tumor annotation and (3)

Bounding box on center slice and center point of tumor on superiormost and inferiormost slice of tumor (**Figure 6.1**). All annotations were made on axial slices. Annotation type (2) was used to accelerate the annotation process. Annotation type (3) was used where the tumor boundary was not visible and difficult to annotate, which is common on images without contrast.

The annotations were exported from MD.ai as Javascript Object Notation (JSON) files and converted to NifTI masks. For annotation types (1) and (2) the polygonal or bounding box vertices were used to determine the masks. For annotation type (3), the bounding box was extended and linearly interpolated to the superiormost and inferiormost slice using the center markers.

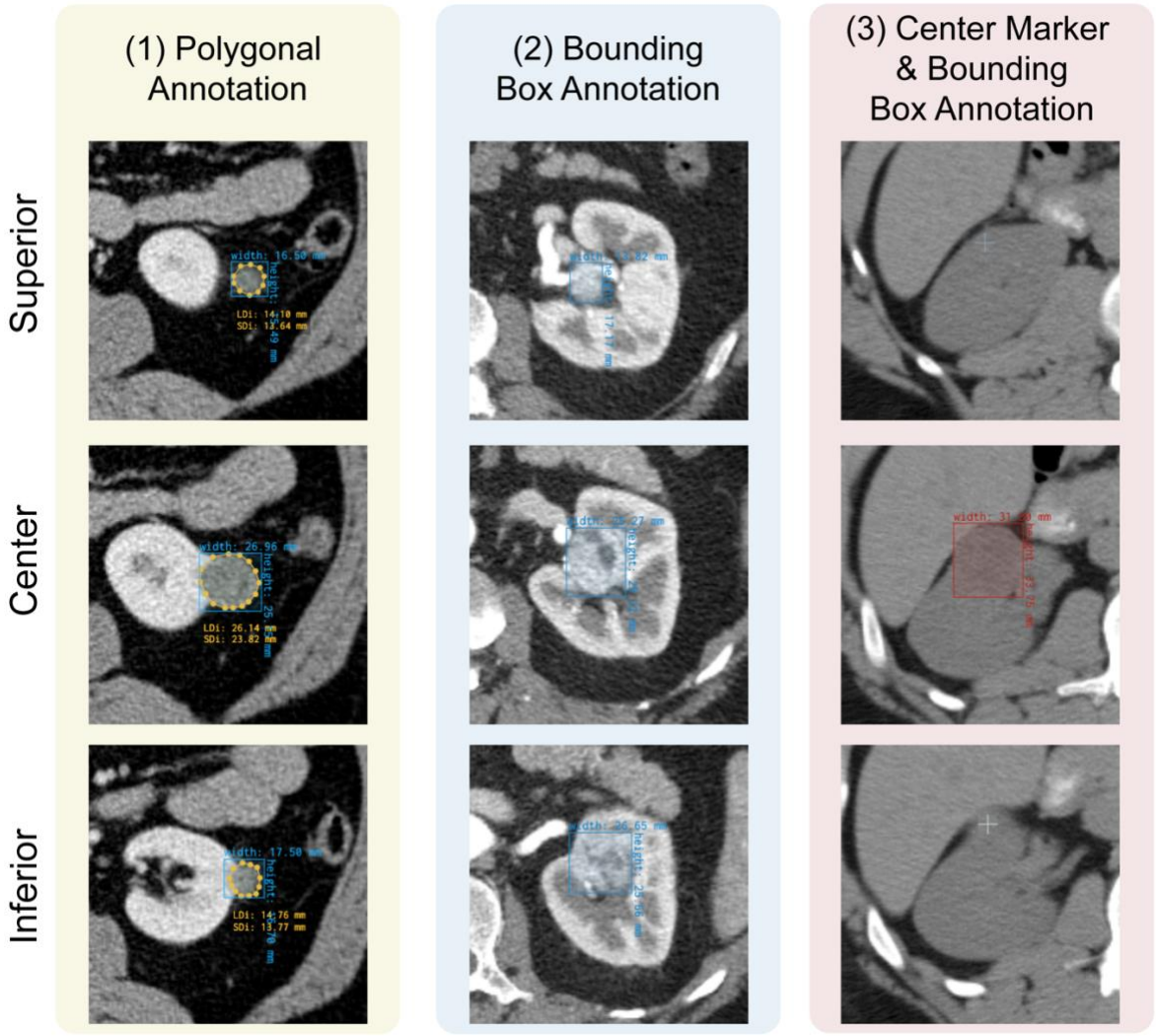

Figure 6.1: Example renal mass segmentations on MD.ai. Three examples of each type of renal mass annotation: (1) polygonal segmentation, shown on an arterial phase image, (2) bounding box segmentation on each slice, shown on a portal-venous phase image, and (3) bounding box on center slice as well as center markers on the superiormost and inferiormost slices, shown on an unenhanced pre-contrast image. For each example, the superiormost (top row), central (middle row) and inferiormost (bottom row) slice is shown. Note: For the polygonal annotation (first column) the images also show bounding box annotations. The yellow annotations are the polygonal annotation referenced.

6.3.4 Registration

For each patient, the post-contrast phase images and their tumor masks (moving images) were registered to the pre-contrast image (static image). Prior to registration the post-contrast images and tumor masks were cropped in the slice dimension to match the FOV of the pre-contrast

image. Then affine registration was performed using the ANTS toolbox. Following phase registration, the same deformation matrix was applied to the tumor masks to register the masks to the pre-contrast image.

Each case was manually quality controlled to ensure proper registration by visualizing the first, middle and last 5 slices of the post-contrast images overlaid on to the pre-contrast image. As there were many cases that failed ANTS registration, an affine registration from the Dipy toolbox was used on the cases that failed.

6.3.5 Conversion to hdf5

For each exam, the best tumor mask was chosen by annotation type with preference rank in the following order: (1) polygonal segmentation, (2) bounding box on all slices, (3) bounding box on central slice and center markers at end slices. The pre-contrast volume, the registered post-contrast phase volumes, best tumor mask and relevant metadata (tumor type, pathology, pathology grade) were all saved together as a single Hierarchal Data Format 5 (HDF5) file for each exam.

6.4 Results

6.4.1 Data Curation

In the end 573 exams were registered with tumor masks and converted to 573 HDF5 files to make up the final dataset. During the data curation process, 389 exams were excluded in total (**Figure 6.2**). For 21 exams, there was no identified pre-contrast scan. Another 86 exams were excluded as they were repeat exams from subjects who had another exam included. These were

excluded so that each exam was completely independent of the other exams. For 10 exams, there were errors converting from DICOM to NifTI and were thus excluded. One patient had errors converting the annotation to masks and was excluded.

During registration, a total of 271 exams failed quality control (**Figure 6.3** and **6.4**). Of these 121 cases failed because the pre-contrast image was acquired with patient supine on the exam table whereas the post-contrast phase images were acquired with the patient prone on the table. These resulted in images that were very difficult to register to one another due to organ movement and orientation changes. Another 150 cases failed for other reasons, such as imperfect registration, cropped FOV of one or more scans, failure of registration algorithm to register in the S/I-direction etc.

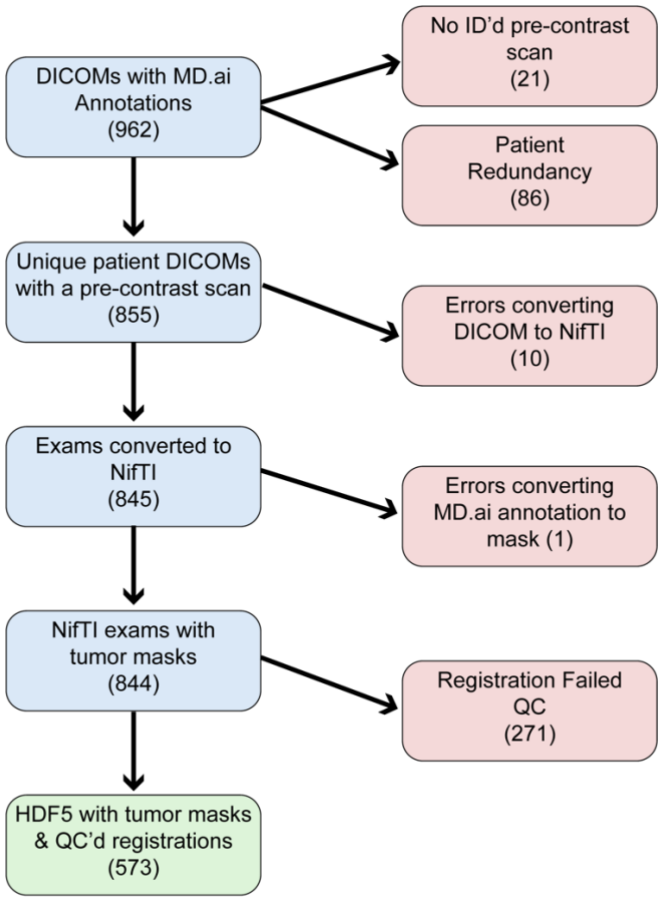

Figure 6.2: Flowchart of Dataset describing each step of data curation and excluded cases (red boxes). The dataset started with 962 patient DICOMs with annotations and ended with 573 registered HDF5 datasets including a tumor mask.

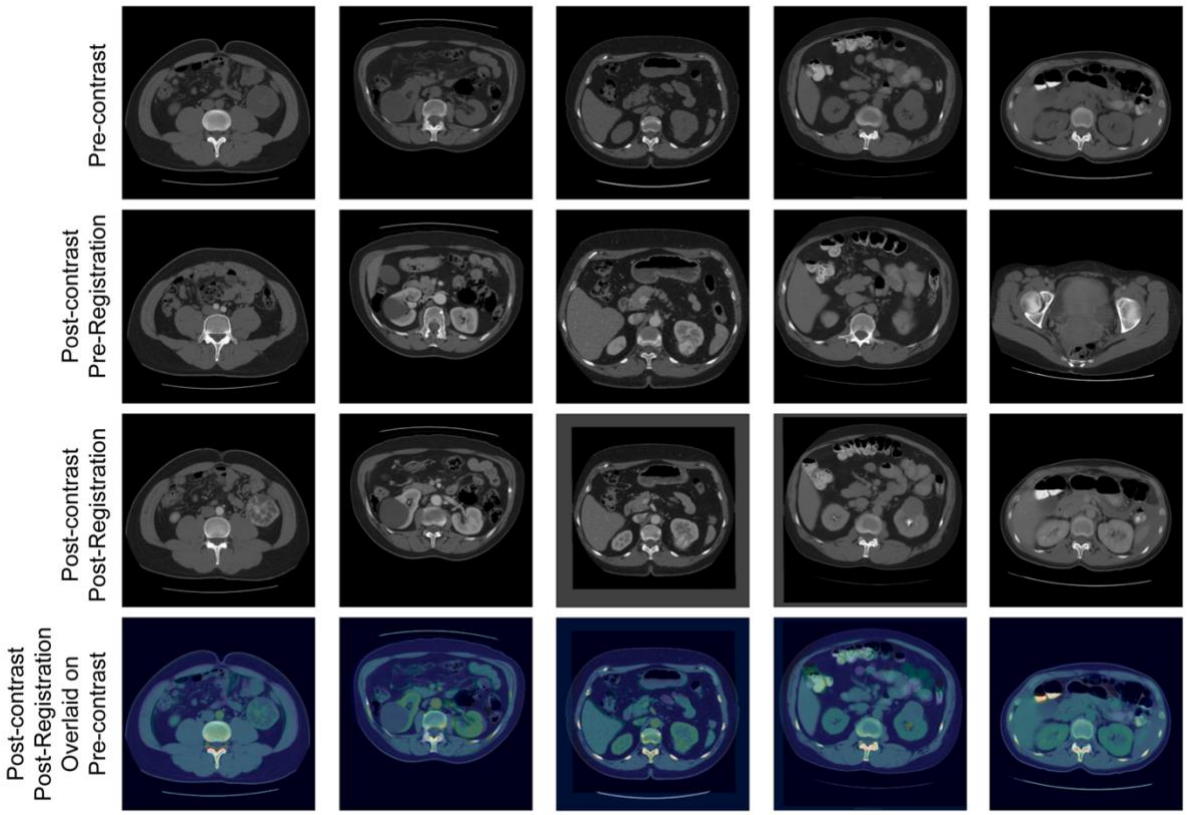

Figure 6.3: Five registration examples that passed quality control (QC). Examples of pre-contrast scans (top row) with corresponding post-contrast phase scans before and after registration. Bottom row displays the post contrast scan overlaid on top of the pre-contrast scan after registration.

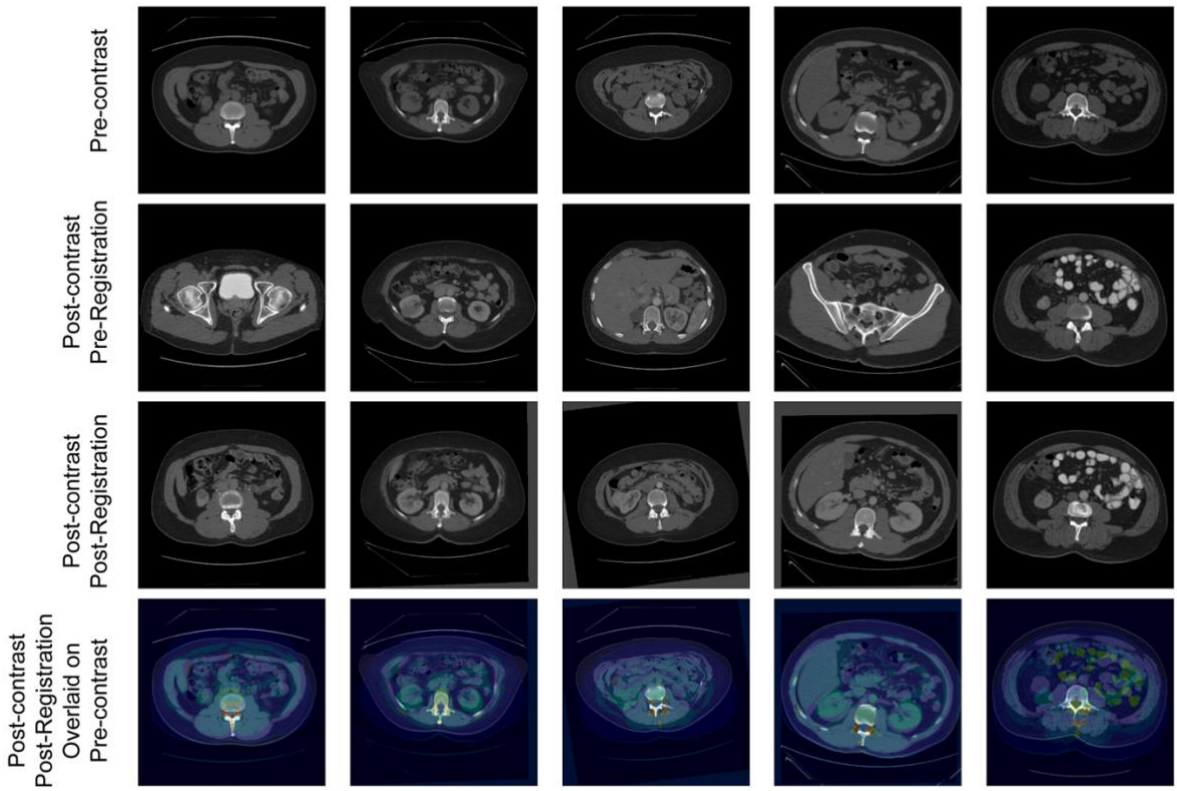

Figure 6.4: Five examples of registrations that failed. Top row shows pre-contrast scans, corresponding post-contrast phase scans before and after registration. Bottom row displays the post contrast scan overlaid on top of the pre-contrast scan after registration. First three columns are cases that failed when the pre-contrast image was taken with the patient prone and post-contrast images with the patient supine.

6.4.2 Final Dataset Demographics

For the final dataset, the pathologies (**Figure 6.5**) and the included phases (**Figure 6.6**) were analyzed to determine the dataset diversity. Most of the dataset consists of RCC cases, with the most common subtype being clear cell (**Figure 6.5**). Of the graded exams, more tumors were low grade versus high grade. Also, most cases were the middle grades (grade 2 or 3) in between low vs high grade and very few exams were the highest grade, grade 4.

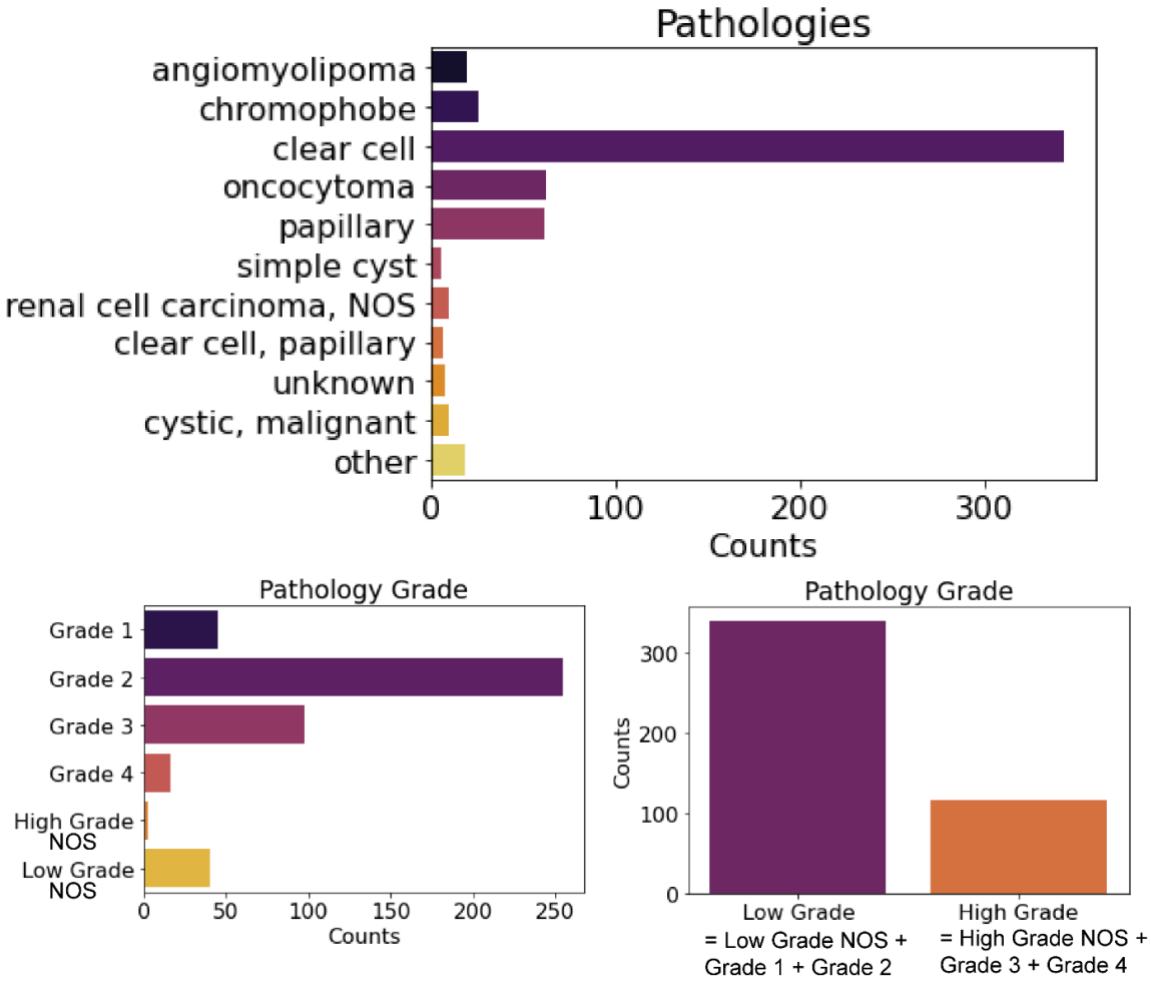

Figure 6.5: The pathologies & pathology grades for the final registered dataset. Note for pathology grades not all pathologies are graded so the bottom plots represent a subset of the full dataset. Some of the pathologies (like chRCC) were not given a grade number but labelled more generally as low or high grade NOS. The majority of the dataset was made up of clear cell RCC and many of the graded cases were low grade with very few cases being of the highest grade, grade 4. NOS= not otherwise specified

Most of the exams included at least one post-contrast phase scan other than the pre-contrast scan (**Figure 6.6**). Of these, the most common case two post-contrast phase scans. There were almost equivalent numbers of scans from each phases, although portal-venous had a slight majority. Less than 100 exams included all three post-contrast phases.

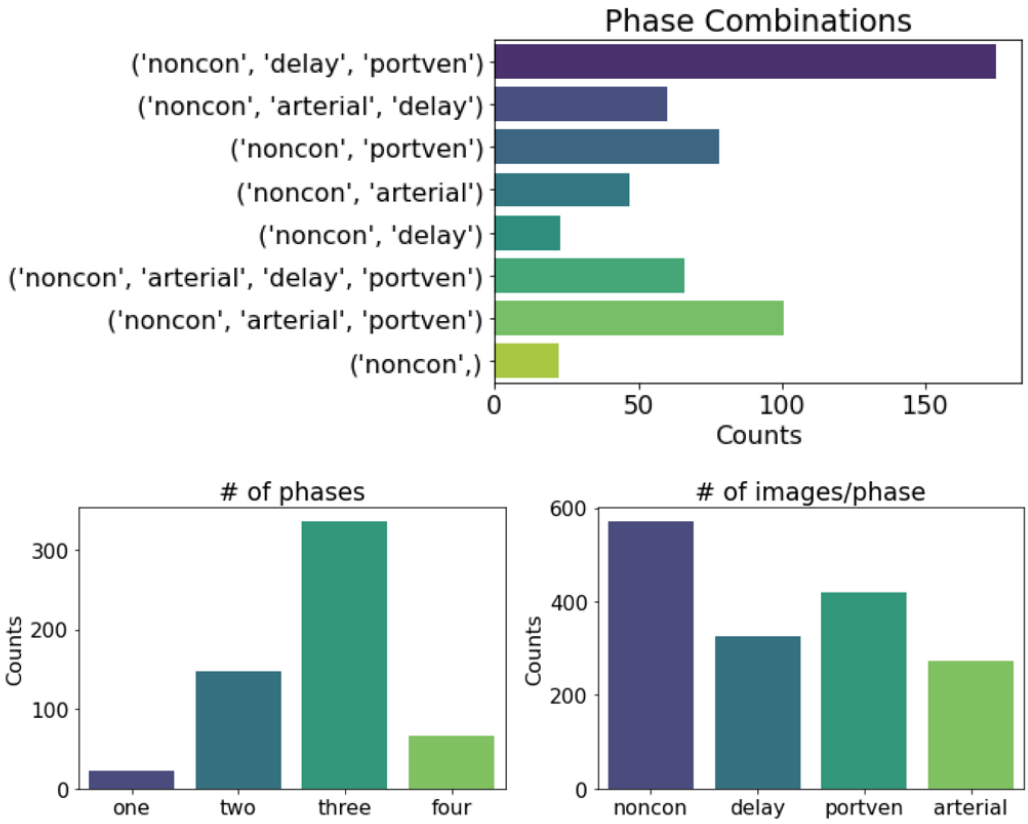

Figure 6.6: The number of scans and phases included for the exams in the the final registered dataset. Most exams included the pre-contrast scan and one or two post-contrast phase scans. The most common post-contrast phase was portal venous, although the number of images was similar for all three post-contrast phases. Noncon = pre-contrast, portven = portal venous

6.5 Discussion

In this work, we introduce and describe the curation of a 3D CT Renal Mass dataset with post-contrast phase scans. We intend to make this dataset available at https://imagingdatasets.ucsf.edu/ and/or on The Cancer Imaging Archive to use for further exploration of renal mass pathology and pathology grade using data driven methods. At the end of data curation, the final dataset contains 573 exams in HDF5 files where each exam has a pre-contrast volume, most cases have one or more post-contrast phase scan volume, a lesion mask and pathology metadata (**Figure 6.2**).

The dataset includes a variety of renal mass pathologies, but most are RCCs (**Figure 6.5**). Of the graded RCCs, the dataset is imbalanced and includes more than twice the number of low-grade cases as compared to high-grade cases. Similarly, ccRCC exams severely outnumber oncocytoma, pRCC and chRCC cases. If the dataset is used for low vs high grade, RCC subtype or benign vs malignant classification tasks, the class imbalance must be considered. Although imbalanced, the distribution of pathologies and pathology grades is representative of renal mass incidence at UCSF.

Another feature of the dataset is the inclusion of pre-contrast volumes along with post-contrast phase scan volumes: arterial, portal venous or delay phases (**Figure 6.6**). Most exams do not include all phases but the pre-contrast exam plus one or two more phases. In the final registered dataset, 22 exams only included the pre-contrast scan even though the initial DICOM inclusion criteria specified at least one post-contrast scan. For these exams, the post-contrast phases could not be registered and therefore were not included.

Along with CT volumes, masks of the renal tumors are also included. Although most of these are bounding boxes, the masks help localize the tumor quickly for analysis. Within this dataset, the CT volumes are provided as-is and no cropping, resampling or normalization has been done. Resampling and normalization would be necessary for input into a deep learning network to ensure consistent pixel spacing across data sampling and avoid exploding gradients during training. Cropping the volumes near the tumor may also be needed for improved model performance[11,13]. These steps are not included to allow for flexibility in preprocessing.

6.5.1 Registration

Registration was a significant bottleneck in the data curation and about 30% of exams were excluded due to failed registration. Particularly, the cases where the pre-contrast image was acquired with the patient supine on the table, and the contrast enhanced phase images were acquired with the patient prone, proved to be a challenge.

In this work, a select number of registration tools were attempted, including both affine and deformable registrations. None of the tools were able to improve results for the prone-supine registration cases. However, there are tools that were not attempted which could yield improved result. Some of these registration tools may require further fine-tuning for abdominal CT application.

6.5.2 Expansion of Dataset

The inclusion of more exams would only improve the utility of the dataset, and therefore the expansion of the dataset must be considered. For one, more of the excluded datasets may be included in the future, such as the 86 exams removed for patient redundancy or the 30% of exams that failed registration. Additionally, the data curation only included renal mass exams from up to 2018 and any since then could be supplemented. For the addition of new data, the functions and scripts used for the described curation steps will be made available on GitHub.

During the described curation process, each scan was converted from DICOM to NifTI to HDF5. The choice to use HDF5 as the final format was decided after starting conversions to NifTI. This pipeline could be optimized by directly converting DICOM to HDF5 in the future.

6.6 Conclusion

Here, a 3D multi-phase renal tumor CT dataset from UCSF with 573 exams is described to supplement available data for pathology characterization and grading tasks. During the curation process, the post-contrast images are registered to pre-contrast image and radiologist annotations are converted to tumor masks and phase labels. The image volumes, masks, and relevant metadata are all packaged together for ease of use in classification tasks. This renal tumor CT dataset can be used in deep learning and texture analysis work in the future to improve performance of models.

6.7 References

1. Wang ZJ, Westphalen AC, Zagoria RJ. CT and MRI of small renal masses. *Br J Radiol*. 2018;91(1087):20180131. doi:10.1259/bjr.20180131

2. van Oostenbrugge TJ, Fütterer JJ, Mulders PFA. Diagnostic Imaging for Solid Renal Tumors: A Pictorial Review. *Kidney Cancer*. 2(2):79-93. doi:10.3233/KCA-180028

3. Krishna S, Murray CA, McInnes MD, Chatelain R, Siddaiah M, Al-Dandan O, et al. CT imaging of solid renal masses: pitfalls and solutions. *Clin Radiol*. 2017;72(9):708-721. doi:10.1016/j.crad.2017.05.003

4. Kang SK, Huang WC, Pandharipande PV, Chandarana H. Solid renal masses: what the numbers tell us. *AJR Am J Roentgenol*. 2014;202(6):1196-1206. doi:10.2214/AJR.14.12502

5. Kaur R, Juneja M, Mandal AK. An overview of non-invasive imaging modalities for diagnosis of solid and cystic renal lesions. *Med Biol Eng Comput*. 2020;58(1):1-24. doi:10.1007/s11517-019-02049-z

6. Sasaguri K, Takahashi N. CT and MR imaging for solid renal mass characterization. *Eur J Radiol*. 2018;99:40-54. doi:10.1016/j.ejrad.2017.12.008

7. Gordetsky J, Eich ML, Garapati M, Del Carmen Rodriguez Pena M, Rais-Bahrami S. Active Surveillance of Small Renal Masses. *Urology*. 2019;123:157-166. doi:10.1016/j.urology.2018.09.017

8. Blumenfeld AJ, Guru K, Fuchs GJ, Kim HL. Percutaneous biopsy of renal cell carcinoma underestimates nuclear grade. *Urology*. 2010;76(3):610-613. doi:10.1016/j.urology.2009.09.095

9. Leveridge MJ, Finelli A, Kachura JR, Evans A, Chung H, Shiff DA, et al. Outcomes of Small Renal Mass Needle Core Biopsy, Nondiagnostic Percutaneous Biopsy, and the Role of Repeat Biopsy. *Eur Urol*. 2011;60(3):578-584. doi:10.1016/j.eururo.2011.06.021

10. Coy H, Hsieh K, Wu W, Nagarajan MB, Young JR, Douek ML, et al. Deep learning and radiomics: the utility of Google TensorFlow™ Inception in classifying clear cell renal cell carcinoma and oncocytoma on multiphasic CT. *Abdom Radiol N Y*. 2019;44(6):2009-2020. doi:10.1007/s00261-019-01929-0

11. Lin F, Ma C, Xu J, Lei Y, Li Q, Lan Y, et al. A CT-based deep learning model for predicting the nuclear grade of clear cell renal cell carcinoma. *Eur J Radiol*. 2020;129:109079. doi:10.1016/j.ejrad.2020.109079

12. Xu L, Yang C, Zhang F, Cheng X, Wei Y, Fan S, et al. Deep Learning Using CT Images to Grade Clear Cell Renal Cell Carcinoma: Development and Validation of a Prediction Model. *Cancers*. 2022;14(11):2574. doi:10.3390/cancers14112574

13. Uhm KH, Jung SW, Choi MH, Shin HK, Yoo JI, Oh SW, et al. Deep learning for end-to-end kidney cancer diagnosis on multi-phase abdominal computed tomography. *Npj Precis Oncol*. 2021;5(1):1-6. doi:10.1038/s41698-021-00195-y

14. Liu J, Yildirim O, Akin O, Tian Y. AI-Driven Robust Kidney and Renal Mass Segmentation and Classification on 3D CT Images. *Bioengineering*. 2023;10(1):116. doi:10.3390/bioengineering10010116

15. Oberai A, Varghese B, Cen S, Angelini T, Hwang D, Gill I, et al. Deep learning based classification of solid lipid-poor contrast enhancing renal masses using contrast enhanced CT. *Br J Radiol*. 2020;93:20200002. doi:10.1259/bjr.20200002

16. Tanaka T, Huang Y, Marukawa Y, Tsuboi Y, Masaoka Y, Kojima K, et al. Differentiation of Small (≤ 4 cm) Renal Masses on Multiphase Contrast-Enhanced CT by Deep Learning. *Am J Roentgenol*. 2020;214(3):605-612. doi:10.2214/AJR.19.22074

17. Zabihollahy F, Schieda N, Krishna S, Ukwatta E. Automated classification of solid renal masses on contrast-enhanced computed tomography images using convolutional neural network with decision fusion. *Eur Radiol*. 2020;30(9):5183-5190. doi:10.1007/s00330-020-06787-9

18. Yu W, Liang G, Zeng L, Yang Y, Wu Y. Accuracy of CT texture analysis for differentiating low-grade and high-grade renal cell carcinoma: systematic review and meta-analysis. *BMJ Open*. 2021;11(12):e051470. doi:10.1136/bmjopen-2021-051470

19. Ding J, Xing Z, Jiang Z, Chen J, Pan L, Qiu J, et al. CT-based radiomic model predicts high grade of clear cell renal cell carcinoma. *Eur J Radiol*. 2018;103:51-56. doi:10.1016/j.ejrad.2018.04.013

20. Bektas CT, Kocak B, Yardimci AH, Turkcanoglu MH, Yucetas U, Koca SB, et al. Clear Cell Renal Cell Carcinoma: Machine Learning-Based Quantitative Computed Tomography

Texture Analysis for Prediction of Fuhrman Nuclear Grade. *Eur Radiol*. 2019;29(3):1153-1163. doi:10.1007/s00330-018-5698-2

21. Feng Z, Rong P, Cao P, Zhou Q, Zhu W, Yan Z, et al. Machine learning-based quantitative texture analysis of CT images of small renal masses: Differentiation of angiomyolipoma without visible fat from renal cell carcinoma. *Eur Radiol*. 2018;28(4):1625-1633. doi:10.1007/s00330-017-5118-z

22. Akin O, Elnajjar P, Heller M, Jarosz R, Erickson BJ, Kirk S, et al. The Cancer Genome Atlas Kidney Renal Clear Cell Carcinoma Collection (TCGA-KIRC) (Version 3). 2016. doi:10.7937/K9/TCIA.2016.V6PBVTDR

23. Linehan M, Gautam R, Kirk S, Lee Y, Roche C, Bonaccio E, et al. The Cancer Genome Atlas Cervical Kidney Renal Papillary Cell Carcinoma Collection (TCGA-KIRP) (Version 4). 2016. doi:10.7937/K9/TCIA.2016.ACWOGBEF

24. Linehan M, Gautam R, Sadow CA, Levine S. The Cancer Genome Atlas Kidney Chromophobe Collection (TCGA-KICH) (Version 3). 2016. doi:10.7937/K9/TCIA.2016.YU3RBCZN

25. Clark K, Vendt B, Smith K, Freymann J, Kirby J, Koppel P, et al. The Cancer Imaging Archive (TCIA): maintaining and operating a public information repository. *J Digit Imaging*. 2013;26(6):1045-1057. doi:10.1007/s10278-013-9622-7

26. Heller N, Sathianathen N, Kalapara A, Walczak E, Moore K, Kaluzniak H, et al. The KiTS19 Challenge Data: 300 Kidney Tumor Cases with Clinical Context, CT Semantic Segmentations, and Surgical Outcomes. March 2020. doi:10.48550/arXiv.1904.00445

CHAPTER 7: SUMMARY & FUTURE WORK

7.1 Summary

In this dissertation, acquisition and quantification advancements for Hyperpolarized [1-^{13}C]Pyruvate (HP C13) MRI were described. The implementation and optimization of a preclinical 2D spectral-spatial EPI for HP C13 MRI was detailed (Chapter 3). Simulations and in vivo results suggested the spectral-spatial EPI sequence in preclinical experiments decreased blurring from phase encodes compared to a CSI sequence. The optimal flip angles for a spectral-spatial EPI sequence were explored through simulation. The fit k_{PL} maps were found to be consistent between the EPI and CSI acquisitions.

For HP C13 MRI quantification efforts, two projects were focused on improving rate constant fitting. The first effort introduced and described a novel pharmacokinetic model for metabolite-specific bSSFP acquisitions (Chapter 4). This model was validated with paired lactate-bSSFP and bicarbonate-bSSFP in vivo datasets and shown to result in similar k_{PL} and k_{PB} values when using a previous pharmacokinetic model. The other project used a U-Net to estimate k_{PL} maps directly from dynamic HP C13 data (Chapter 5). For simulated data, the U-Net estimated maps performed better than voxel-wise fitting methods. For in vivo data, the U-Net predicted maps appear over-smoothed before finetuning. After finetuning, the U-Net predicted maps appear more realistic and resemble the voxel-wise pharmacokinetic model fit maps.

Finally, a 3D multiphase renal tumor CT dataset is detailed (Chapter 6). This dataset can be used in renal tumor classification tasks, such as tumor grade classification or malignant vs benign classification.

7.2 Future Work

Renal cell carcinoma (RCC) is a strong candidate for HP C13 MRI due to the metabolic reprograming present in RCC. Although preliminary studies are promising[1,2], there is a need for larger scale studies studying k_{PL} and possibly other rate constants, k_{PB} and k_{PA} in RCC to fully evaluate their clinical value.

Ideally, more consistency and a consensus on the best method of deriving k_{PL} is also required. The strength of k_{PL} is that it should be comparable across studies, acquisition parameters and institutions. In evaluating possible methods of deriving k_{PL}, fitting to a pharmacokinetic model has been the most popular approach. One consideration with fitting to a model is determining which model to use. Although more complicated models may be more accurate, they usually include more parameters. Especially if these parameters are not known, they may need to be fit along with the rate constants. The fitting becomes challenging, inaccurate and sometimes not possible when there are many unknown parameters. For example, the accuracy of the k_{PL} fits decreased when lactate T_2 was fit instead of fixed in Chapter 4. The most useful pharmacokinetic model will have to balance complexity and simplicity as well as be accurate and applicable across varied acquisition choices.

Deep learning may also be an option for deriving k_{PL} and was shown for the first time here (Chapter 5). This still needs to be further explored, developed and potentially even integrated with pharmacokinetic fitting methods. Particularly, unsupervised or physics-based deep learning may be interesting and worthwhile to pursue. Although promising, there is still a lot of development left for adoption of using neural networks to estimate k_{PL} maps.

For the proposed renal tumor CT dataset (Chapter 6), the most important next step is exploring the effect of adding this dataset as additional examples within neural networks that have already had success in renal tumor classification. More data should help generalize or further evaluate successful frameworks. In the larger picture, there may be further challenges for deep learning or radiomics with texture analysis for renal characterization to be adopted clinically. New contrasts, like HP C13 MRI, may be the key to improving performance to get it closer to adoption.

7.3 References

1. Tang S, Meng MV, Slater JB, Gordon JW, Vigneron DB, Stohr BA, et al. Metabolic imaging with hyperpolarized 13C pyruvate magnetic resonance imaging in patients with renal tumors—Initial experience. *Cancer*. 2021;127(15):2693-2704. doi:https://doi.org/10.1002/cncr.33554

2. Ursprung S, Woitek R, McLean MA, Priest AN, Crispin-Ortuzar M, Brodie CR, et al. Hyperpolarized 13C-Pyruvate Metabolism as a Surrogate for Tumor Grade and Poor Outcome in Renal Cell Carcinoma—A Proof of Principle Study. *Cancers*. 2022;14(2):335. doi:10.3390/cancers14020335

Publishing Agreement

It is the policy of the University to encourage open access and broad distribution of all theses, dissertations, and manuscripts. The Graduate Division will facilitate the distribution of UCSF theses, dissertations, and manuscripts to the UCSF Library for open access and distribution. UCSF will make such theses, dissertations, and manuscripts accessible to the public and will take reasonable steps to preserve these works in perpetuity.

I hereby grant the non-exclusive, perpetual right to The Regents of the University of California to reproduce, publicly display, distribute, preserve, and publish copies of my thesis, dissertation, or manuscript in any form or media, now existing or later derived, including access online for teaching, research, and public service purposes.

DocuSigned by:
Sule Sahin
F743FA5350FF465...
Author Signature

8/23/2024
Date